Attractive interactions in similarly charged polyelectrolytes

By

Anvy Moly Tom

PHYS10201205011

The Institute of Mathematical Sciences, Chennai

A thesis submitted to the

Board of Studies in Physical Sciences

In partial fulfillment of requirements
For the Degree of

DOCTOR OF PHILOSOPHY

of

HOMI BHABHA NATIONAL INSTITUTE

December, 2018

Homi Bhabha National Institute

Recommendations of the Viva Voce Committee

As members of the Viva Voce Committee, we certify that we have read the dissertation prepared by Anvy Moly Tom entitled “Attractive interactions in similarly charged polyelectrolytes” and recommend that it maybe accepted as fulfilling the dissertation requirement for the Degree of Doctor of Philosophy.

____ **Date:**
Chair -Gautam I Menon

____ **Date:**
Guide/Convener -Satyavani Vemparala

____ **Date:**
Co-Guide -Rajesh Ravindran

____ **Date:**
Examiner -

____ **Date:**
Member 1 -R Ganesh

____ **Date:**
Member 2 -Pinaki Chaudhuri

Final approval and acceptance of this dissertation is contingent upon the candidate’s submission of the final copies of the dissertation to HBNI.

I hereby certify that I have read this dissertation prepared under my direction and recommend that it may be accepted as fulfilling the dissertation requirement.

Date: **Guide:** Satyavani Vemparala

Place: **Co-Guide:** Rajesh Ravindran

STATEMENT BY AUTHOR

This dissertation has been submitted in partial fulfillment of requirements for an advanced degree at Homi Bhabha National Institute (HBNI) and is deposited in the Library to be made available to borrowers under rules of the HBNI.

Brief quotations from this dissertation are allowable without special permission, provided that accurate acknowledgement of source is made. Requests for permission for extended quotation from or reproduction of this manuscript in whole or in part may be granted by the Competent Authority of HBNI when in his or her judgement the proposed use of the material is in the interests of scholarship. In all other instances, however, permission must be obtained from the author.

Anvy Moly Tom

DECLARATION

I, hereby declare that the investigation presented in the thesis has been carried out by me. The work is original and has not been submitted earlier as a whole or in part for a degree / diploma at this or any other Institution / University.

Anvy Moly Tom

List of Publications arising from the thesis

Published

1. Anvy Moly Tom, R. Rajesh, and Satyavani Vemparala. "Aggregation dynamics of rigid polyelectrolytes." The Journal of Chemical Physics 144(3):034904, 2016.
2. Anvy Moly Tom, Satyavani Vemparala, R. Rajesh, and Nikolai V. Brilliantov. "Mechanism of chain collapse of strongly charged polyelectrolytes." Physical Review Letters 117(14):147801, 2016.
3. Anvy Moly Tom, Satyavani Vemparala, R. Rajesh, and Nikolai V. Brilliantov. "Regimes of electrostatic collapse of a highly charged polyelectrolyte in a poor solvent." Soft Matter 13(9):1862, 2017.
4. Anvy Moly Tom, R. Rajesh, and Satyavani Vemparala. "Aggregation of flexible polyelectrolytes: Phase diagram and dynamics." The Journal of chemical physics 147(14):144903, 2017.

ACKNOWLEDGEMENTS

This thesis would be absolutely impossible without the helping hand of many individuals. I would like to thank them here. I would like to express my sincere gratitude to my research guides Prof. Satyavani Vemparala and Prof. R. Rajesh for their valuable guidance, scholarly advice and encouragement, without which I would not have completed this work. They showed me proper direction as well as offered help when I was facing difficulty in carrying out my work. They provided me with interesting and relevant problems to work on, but also helped me improve my way of thinking about problems. I am really grateful to my mentors for their for the arduous effort they put to guide me. I feel blessed to have carried out this endeavour under my facilitators who inspired me, gave me a lot of freedom and inspired me, profoundly like a family member during my entire Ph.D period. I would like to thank Prof. N. Brilliantov for a wonderful collaboration.

I owe my sincere thanks to the faculty members of IMSc for their guidance given during discussions, which we had at the time of our course work. I am greatly indebted to my Doctoral committee members who directed me with their advices and suggestions.

I am grateful to my seniors Upayan and Anoop who directed me and provided me with materials which were important. I would like to thank Renjan for his extended support during course work and initial stages of PhD. I also benefited a lot from discussions with Prasad ettan, Sasi etten, Assa chechi, Arya, Meghna, Arjun, Karthika and Jilmy on various occasions.

My sincere gratitude towards IMSc where I have spent more than six years of Ph.D. The academy offered a heartwarming atmosphere throughout the course - work comprised of, lectures and discussion sessions with faculty members and friends. I would like to thank IMSc for the High-Performance computing facilities, especially Annapurna, Nandadevi and Satpura, and for library access. Apart from them, people in computer centre, Vasan and Mangal also supported me to a great extent in pursuing my research. Also I am indebted to my batchmates who helped me during the entire Ph.D period. The staff members of office, library, security as well as support staff of our institution for their support and encouragement during my life at IMSc.

I must mention Vincent sir who played the role of a path maker in my life. A reservoir of knowledge is the only adjective apt for him. His valuable and inspiring words while I was pursuing M.Sc became a turning point in my life to choose research. I would like to Abraham Sir, Ison sir, Isacc Sir and Shebin Sir for their extended support throughout Ph.D. I should thank Indian Academy of Science for arranging a refresher course at my college which made me choose research at IMSc.

I am thankful to my family for their immense support and encouragement extended to me during all stages of my Ph.D work. My papa is the only reason behind where I am today. In my village, people around us always discouraged us from pursuing higher studies and persuaded us to get a job. But, Papa! you supported my decision to continue studies as per my wish. Along with papa, mammy, you also supported me to achieve my goal. I am grateful to Binvy, Tom and Cinvin for the constant encouragement throughout my life. My spouse Rathul played a vital role throughout. He understands perfectly the life of a research scholar and made things easier for me. His constant encouragement and inspiration elevated the level of my work. I would like to thank Amma, Ettan and Johita for the support provided.

I deeply thank Divya, Jilmy, Meghna, Arya, Sruthy, Anupam, Arjun, Revathi, Sumesh ettan, Prasad ettan, Anju, Sasi ettan, Radhu, Suneetha and Sangeetha for your great friendship, support, company, and readership throughout these years. I would like to thank Arya, Ammu and Rahul for their comments on the thesis.

I would like to remember my beloved friend Pavan who left us in the middle of our venture.

Contents

Synopsis

Polyelectrolytes (PEs) are polymers with ionizable groups which release counterions when dissolved in solutions, rendering the backbone of the polymer chain charged. Examples of PEs include biological polymers such as DNA, RNA, actin, virus, etc. [1–3] , as well as synthetic polymers such as sulphonated polystyrene, polyacrylic acid, etc. [4–8]. PEs have a wide range of applications, such as gene therapy, drug coating, water purification, color removal, paper making, etc. The dynamic and structural properties of PEs, critical for their applications, are crucially dependent on the conformational phases of PEs. These phases are primarily determined by the competition between the repulsive electrostatic interactions among like-charged monomers of the PE chains and the entropy of the unbound counterions. Depending on the relative dominance, the unbound counterions may condense onto the polymer backbone, renormalizing the charge density, and facilitate effective short-ranged attractive interactions between monomers [9]. In the dilute limit of a single PE chain in isolation, the effective interactions can result in extended, bead-necklace, and collapsed conformations depending on the charge density of the PE chain and the temperature of the system [10–18]. At finite densities of PE chains, the effective attractive interactions among the PE chains may lead to aggregation.

This thesis is divided into two parts. The first part addresses the mechanism that drives the collapse transition of a single PE from an extended to a collapsed phase. The second part studies the statics and dynamics of aggregation in a collection of PEs, both flexible and rigid. Both these problems are studied primarily using extensive molecular dynamics (MD) simulations of coarse-grained models.

Mechanism of the collapse of a single flexible PE

Several experiments and simulations have shown that at large enough charge density, ℓ_B, a like-charged PE chain undergoes a transition from an extended to collapsed conformation regardless of the solvent quality [11–15]. This counterintuitive transition is driven by the condensation of counterions onto the chain, reducing the effective charge density. The nature of the effective attractive interactions driving the transition is not well-understood and there are competing theories explaining their origin. For the collapsed state, these theories predict that the gyration radius, R_g, of a PE has the scaling form $R_g \sim N_m^{1/3} \ell_B^{-\gamma}$, where N_m is the PE chain length, and the exponent γ can potentially depend on system parameters. In the literature, there are three theoretical approaches [15–18], based on different physical models, to account for the electrostatics-driven counterintuitive collapse of similarly charged PEs. All the theories predict a single collapsed regime, but differ in their prediction of the exponent γ characterizing the dependence of R_g on ℓ_B. In the first approach [16], the system of charged, collapsed PE and the corresponding counterions is modeled as an amorphous ionic solid. In this theory, the system achieves minimum free energy when the PE is in a collapsed state and the R_g is independent of the charge density of the PE, thus leading to $\gamma = 0$. In the second theory, pairs of condensed counterions and PE monomers are treated as fluctuating dipoles, and the attractive dipole-dipole interaction energy is identified as the driving force behind the collapse of the PE in both good as well as poor solvents [17, 18]. The dipole theory proposes a scaling of R_g with ℓ_B as $R_g \sim \ell_B^{-2/3}$, leading to a value of $\gamma = 2/3$ for both good and poor solvents. The third theory, referred to as counterion fluctuation theory, proposes that attractive interactions driving the collapse transition is a result of the density fluctuations of the condensed counterions leading to a negative pressure [15]. This theory predicts $\gamma = 1/2$ for good solvent

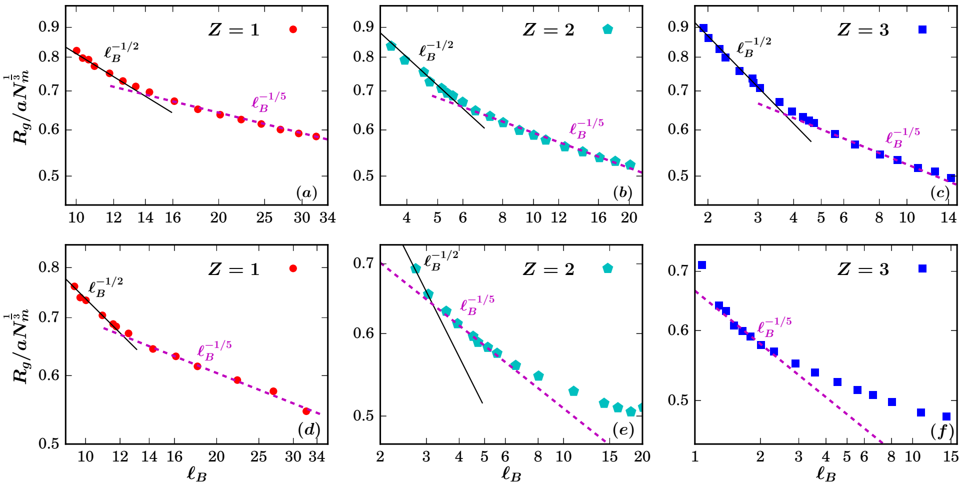

Figure 1: The variation of the radius of gyration (R_g) of the collapsed phase with charge density (ℓ_B) for a PE chain of length N_m and bond length a in (a)-(c) good solvent conditions and (d)-(f) poor solvent conditions.

conditions.

We present the results of extensive MD simulations exploring the collapsed conformation of a single flexible PE chain in both good and poor solvents. Our main results are summarized below.

- MD simulation results of a good solvent [Fig. 1(a)-(c)] reveal two collapsed regimes, that we refer to as weak and strong electrostatic regimes. In the first regime, the exponent $\gamma = 1/2$ (characterizing the dependence of R_g on ℓ_B) while in the second one $\gamma = 1/5$. This scaling is robust and independent of the valency of the counterions, volume interaction models between chain monomers and on the solvent models. The scaling in the weak electrostatic regime ($\gamma = 1/2$) is not consistent with the predictions of either the fluctuating dipole theory ($\gamma = 2/3$) [17, 18], or of the amorphous ionic solid ($\gamma = 0$) [16], but agrees with the counterion fluctuation theory [15] proposed earlier. However, the scaling in the strong electrostatic regime ($\gamma = 1/5$) is not consistent with any of the existing theories.

- We find the existence of several sub-regimes in the dependence of the gyration radius of the chain R_g on ℓ_B for poor solvents as shown in Fig. 1 (d)-(f). In contrast to a good solvent, the exponent γ for a poor solvent crucially depends on the size and valency of the counterions.

- We develop a generalized theory for a collapsed regime of a PE in good and poor solvents based on counterion fluctuation theory [15], by explicitly considering the monomer-monomer, monomer-counterion and counterion-counterion interactions. In the original counterion fluctuation theory [15], the volume contribution of PE free energy was truncated at the second virial coefficient. We have included more terms in the virial expansion depending on the packing fraction of the system, resulting in multiple regimes with different exponents. This generalized counterion fluctuation theory describes the MD results for both good and poor solvents well.
- We also show that the presence of condensed counterions modifies the effective attraction among the chain monomers and modulates the sign of the second virial coefficient under poor solvent conditions.

Aggregation dynamics of rigid PEs

At finite densities of PE chains, the effective attractive interactions among the PE chains can lead to aggregation, in addition to individual collapsed phases. Understanding such counterion-mediated aggregation of charged polymers is very relevant as the aggregation of biopolymers such as DNA and actin has been implicated to play an important role in biological functions such as cell scaffolding, DNA packaging, and cytoskeletal organization [2, 19]. In addition to biological polymers, recent studies have shown that the aggregation of synthetic polymers is crucial in their ability to function as biomimetic and functional materials [20–22].

We study the dynamics of aggregation of rigid PEs using MD simulations. Figure 2 shows the snapshot of a system of $N(0) = 100$ rigid PEs with charge density $\ell_B = 3.57$ and valency $Z = 3$ at different times. As the time evolves, the PEs aggregate and the number

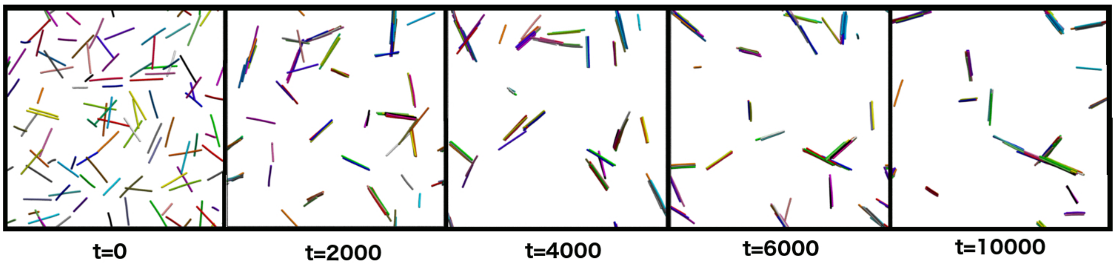

Figure 2: Snapshots of a collection of rigid PEs system at different times for $\ell_B = 3.57$ and $Z = 3$. The counterions are not shown for better clarity.

of aggregates decreases. The main results obtained are summarized below.

- The fraction of aggregate $n(t) = N(t)/N(0)$ decreases with scaled time t/t^* as a power law $t^{-\theta}$. From our simulations, we find $\theta = 0.62 \pm 0.07$, as shown in Fig. 3.

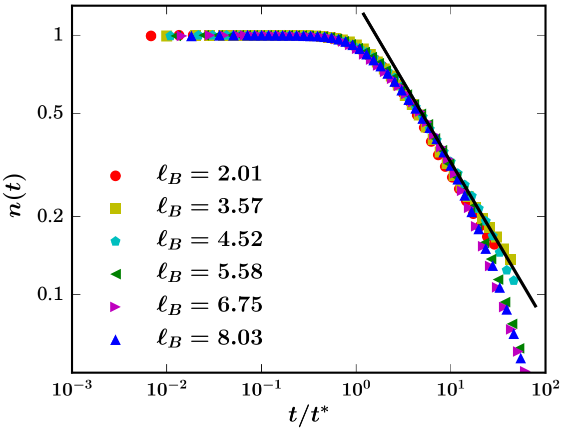

Figure 3: The variation of the fraction of aggregates $n(t)$ with scaled time t/t^* for different values of ℓ_B for systems with trivalent counterions, where t^* is the time at which $n(t) = 0.9$. The straight line corresponds to power law $(t/t^*)^{-0.62}$.

- We find that the exponent θ is independent or utmost weakly dependent on ℓ_B and other system parameters such as valency (Z), density (ρ), length of PE chains (N_m).

- The exponent θ characterizing the power law decay of the number of aggregates is quite universal. It is thus plausible that aggregation is driven by diffusion and irreversible aggregation (we do not see any fragmentation event) due to short-ranged attractive forces. With this assumption, we recast the aggregation dynamics of PE in terms of the Smoluchowski equation for irreversible aggregation [23],

$$\frac{dN(m)}{dt} = \frac{1}{2}\sum_{m_1=1}^{m-1} K(m_1, m-m_1)N(m_1)N(m-m_1) - \sum_{m_1=1}^{\infty} K(m,m_1)N(m)N(m_1), \quad (1)$$

where $N(m)$ is the number of aggregates of size m at time t, and collision kernel $K(m_1,m_2)$ is the rate at which two masses m_1 and m_2 collide. The first term in Eqn. (4.6) describes the aggregation of particles to form an aggregate of size m, while the second term describes the loss of an aggregate of size m due to collision with other particles. From the observed cylindrical shape of PE aggregation, we deduce the collision kernel. For this collision kernel, we find $\theta = 2/3$, which is in agreement with our MD simulation results. Our results suggest that once counterions condense, effective interactions between PE chains short-ranged and the aggregation of PEs are diffusion-limited.

Role of flexibility in the aggregation of multiple PEs

The introduction of flexibility in the charged polymer backbone is expected to fundamentally alter the aggregation dynamics, as additional time scales can emerge due to the possibility of the system getting trapped by kinetic barriers. We aim to understand the behavior of aggregation in the case of completely flexible PEs (FPEs). The main results are summarized below.

- In the case of FPEs, aggregation as well as fragmentation events are present.
- Unlike rigid charged polymers, the phase diagram of the flexible charged polymers with valency $Z = 3$ as shown in Fig. 4, consist of three different phases depending on the charge density: one with no aggregation, another with finite bundles and a fully phase separated phase.
- An individual FPE chain within an aggregate becomes more extended with increas-

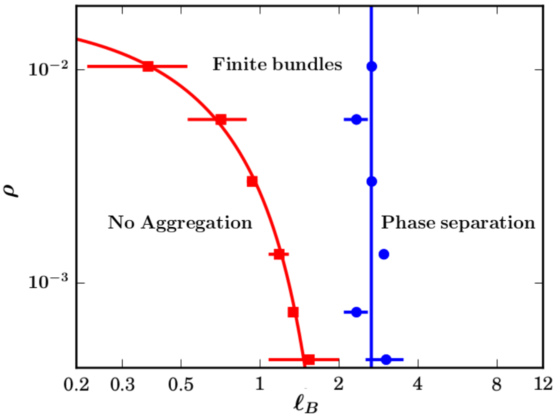

Figure 4: Phase diagram for a collection of flexible PEs in the ρ-ℓ_B plane. There are three phases: one with no aggregation, another one with finite-sized bundles and a completely phase separated phase.

ing aggregate size, and we show that its non-bonded nearest neighbors are increasingly from other FPE chains, implying that the FPE chains within an aggregate are strongly entangled.

- The dynamics of aggregation in the phase-separated phase were quantified through the temporal variation of the fraction of the aggregate $n(t)$: $n(t) \sim t^{-\theta}$ as in the case of rigid PEs. We find that, θ decreases with increasing charge density and varies from from $0.6-0.35$ for the range of charge densities considered. This is in contrast to the charge independent value of $\theta \approx 0.62$ obtained for rigid PE chains through MD simulations. The reason for the dependence of the exponent on charge may be due to the additional time scale involved in the system due to the rearrangements inside an aggregate such as opening up and closing up of an existing aggregate consisting of entangled FPE chains, during the addition of a new one. Such a rearrangement is absent in the case of rigid PE aggregation.

- In the case of FPE aggregate, we observe multiple regimes characterized by different scaling exponents in the relation between the radius of gyration and the effective Bjerrum length of the PE chain ($R_g \sim \ell_B^{-\gamma}$) as predicted by generalized counterion fluctuation theory for a single PE chain collapse. This provides further evidence for the counterion fluctuation theory being the correct description for the effective attractive interactions in charged PE systems.

Chapter 1

Polyelectrolytes: Introduction

Polyelectrolytes (PEs) are long, electrically charged molecules in polar solutions. The oppositely charged counterions are present in the solution such that the system is overall neutral. This chapter deals with a brief introduction to polymers and PEs, which includes different measurement parameters of polymers, basic models etc. It also contains the outline of the thesis.

1.1 What are polyelectrolytes?

Polyelectrolytes (PEs) are polymers with ionizable groups, which release counterions when dissolved in solutions, rendering the backbone of the polymer chain charged. These are similar to simple salts such as $NaCl$, which gives Na^+ and Cl^- in solution. Hence, PEs are also known as polysalts. PEs have characteristics of both polymers and electrolytes. A polymer molecule is defined as a long chain with repeating units of atoms that are bonded through covalent bonds. The group of atoms that repeat are called monomers, and a polymer is group of monomers connected via covalent bonds. If the monomers are identical then such polymers are called homopolymers whereas if more than one kind of monomers exist in a single chain, then such polymers are called heteropolymers. The total number of monomer units present in a polymer is referred to as the degree of polymerization.

In a PE, the degree of ionization is denoted by f and it's value varies from 0 to 1. If all the monomers are charged, then $f = 1$, and such PEs are called strongly charged PEs whereas if $f<1$ only some of the monomers are charged and they are called weakly charged PEs. The schematic diagram of a strongly charged and a weakly charged PE are given in Fig. 1.1. When the ionizable groups dissociate, polymer molecules become charged either positively or negatively, depending upon the specific functional groups present. Polymers whose ionizable functional groups have a net positive charge are called cationic PEs and those with a net negative charge are called as anionic PEs. The polymers having both positive and negative charges such that they have zero total charge are called nonionic PEs. Examples of PEs vary from naturally occurring PEs to synthetic PEs. [1–8].

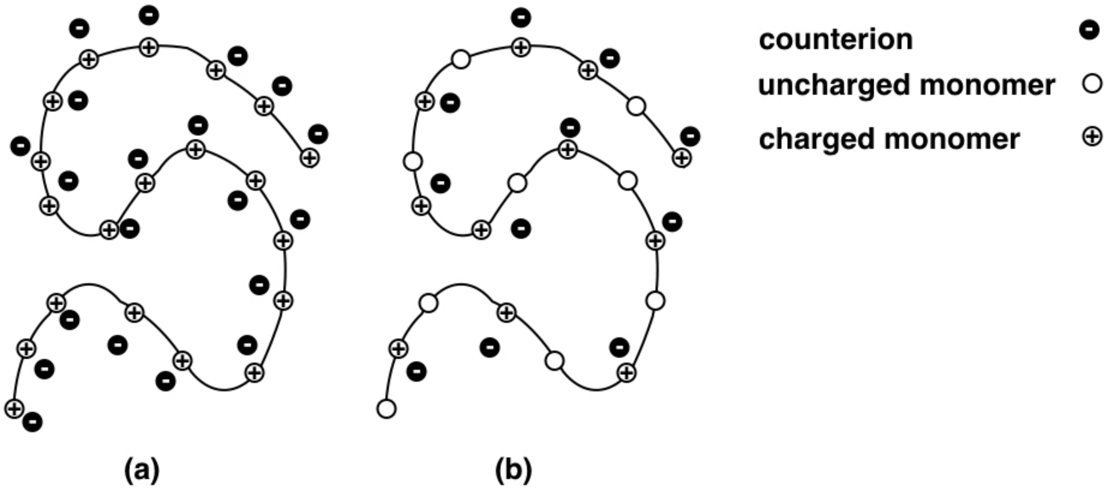

Figure 1.1: A schematic diagram of a PE with (a) $f = 1$ and (b) $f < 1$.

1.1.1 Biological PEs

Examples of biological PEs include DNA, RNA, actin, virus, polypeptides, polysaccharides etc [1–3]. The double stranded DNA (dsDNA) is a highly charged PE of $-2e$ charge per base pair and each elementary charge comes from phosphate group present in the backbone [24]. The electrostatic interactions in biological PEs play a crucial role in their structural and dynamical properties. For example, PEs often self-organize by the electrostatic interactions to form superstructures. DNA compaction into chromatin fiber in the nuclei of eukaryotic cells is a typical example of such super structures [24]. The genomic DNA forms superstructures with the help of positively charged histone proteins in the nuclei of eukaryotic organisms [25, 26]. Aggregation of biological PEs are important to some disease states. For example, histones promote the aggregation and fibrillation of α-synuclein protien, which plays an important role in the pathogenesis of Parkinson's disease [27]. Furthermore, molecular cluster formation can also cause debilitating neurodegenerative diseases like Alzheimer syndrome, where a few identical small fragments of large proteins show the tendency to form fibrils. For example, $A\beta_{16-22}$ peptides self-assemble into aggregated structures with a high β-strand content [28].

1.1.2 Synthetic PEs

Examples of synthetic polymers include sulphonated polystyrene, polyacrylic acid, etc [4–8]. The charges on PEs can be dynamic, causing polymer chains to adopt different equilibrium conformations even with relatively small changes to the surrounding environment such as pH, temperature, presence of solvent etc. This property of PEs is used in chemical separation and bio-medical applications such as drug delivery [6, 29–31], gene therapy [5, 32–34] etc. PEs are widely used as flocculants, which are used in solid-liquid separation [4]. If a charged macro-ion is added to a system of colloidal suspensions, it destabilizes the suspensions and form a large aggregate and which separates from liquids by sedimentationand this process is called flocculation. Synthetic PEs are widely used as flocculants in many industries such as in water purification [7, 35–37], color removal [8, 38–40], paper making [4, 41] etc. The cross-linked PEs form three-dimensional structures that swell in water rather than dissolving in it. They can retain extremely large amounts of liquid relative to their own mass (500 times its weight) through hydrogen bonding with water molecules. This feature of PEs is used in making super absorbent products like baby diapers and other disposable personal hygiene products, such as adult protective underwear and sanitary napkins [42–45].

1.1.3 Importance of PE studies

The description of PEs is quite challenging primarily because of the long range electrostatic interaction. Many non linearly coupled variables control the properties of PE and the whole system is strongly correlated. The dynamical and structural properties of the PEs, critical for their applications, are crucially dependent on the conformational phases that the PEs may assume depending on a variety of conditions and parameters of the system. These phases are primarily determined by the competition between the repulsive electrostatic interactions among the like-charged monomers of the PE chains and the entropy of the free counterions. Depending on the relative dominance between the energy and the entropy, free counterions may condense onto the polymer backbone [9,46,47], renormalizing the charge density, and facilitate effective short-ranged attractive interactions between monomers and cause counterintuitive behavior to PE systems. Several theoretical, computer simulations, and the experimental studies have been done on PE system and some of them will be described briefly in later sections, though the understanding of the behavior of PEs are still incomplete.

1.2 Neutral polymer vs Polyelectrolyte

Polymers exhibit different interesting behaviors depending on external conditions such as temperature, solvent quality etc. and the conformations of polymers are determined by the resultant dominant interactions in the system. Consider a polymer in a solvent, where the typical interactions are between monomer-monomer, monomer-solvent, and

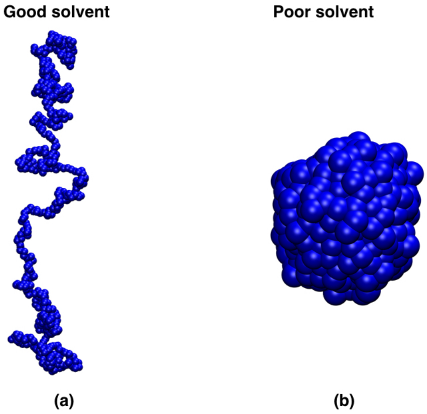

Figure 1.2: Typical snapshot of a neutral polymer in (a) good solvent (b) poor solvent. In good solvent, polymer acquires an extended conformation where as in poor solvent, it acquires a collapsed conformation.

solvent-solvent. If monomer-monomer interaction dominates over monomer-solvent interaction, then the chain is likely to be in a collapsed state and the polymer is said to be in poor solvent conditions. On the other hand if the monomer-solvent interaction is greater than the monomer-monomer interaction, then the chain is likely to be in an extended state and the polymer is said to be in good solvent conditions. Such solvents are known as good solvents. Solvent quality can be changed by changing the temperature, as we increase temperature nature of solvent changes from poor to good solvent quality [48]. Neutral polymer undergoes a transition from extended to collapsed conformation as we change temperature or solvent quality from good to poor solvent. A typical conformation of a neutral polymer in a good solvent and a poor solvent is shown in Fig. 1.2 (a) and Fig. 1.2 (b) respectively. The detailed theoretical description of extended to collapsed transformation is explained in Sec. 1.2.3.

Charged polymers, PEs are intrinsically different from neutral polymers since they carry multiple charges along its backbone, which generates long-range electrostatic interaction. Furthermore, the PE backbone is always accompanied by oppositely charged counterions which neutralizes it. These features constitute the unique and complicated properties of PEs, such as chain conformation, rheology, dynamics, and phase behaviors, different from those of neutral polymers.

One of the important length scales in system of PEs is Bjerrum length (ℓ_B) and it is the length scale at which the electrostatic interaction energy of two monovalent ions is comparable to the thermal energy k_BT, where T is the absolute temperature. Bjerrum length is given by

$$\ell_B = \frac{e^2}{4\pi\epsilon_0 k_B T}, \tag{1.1}$$

where ϵ_0 is the dielectric constant and e is the charge of monomer. The quantity ℓ_B is a measure of the distance at which the Coulomb energy and the thermal fluctuations are comparable. If the distance between ions is shorter than ℓ_B, the electrostatic interactions dominate. In other-words, for large Bjerrum length ℓ_B electrostatic interactions dominate whereas for small Bjerrum length thermal effects dominate. In water at room temperatures, Bjerrum length $\ell_B \sim 0.7nm$ [24]. For small Bjerrum lengths, counterions are likely to move throughout the entire volume and the counterion entropy will be maximum. Fig. 1.3 shows the snapshot of a single flexible PE at different Bjerrum lengths. At very small ℓ_B [Fig. 1.3 (a)], the chain behaves like a neutral polymer and the counterions are randomly distributed in the box to maximize their entropy. For critical ℓ_B, counterion starts condensing on the chain and a phenomenon called Manning condensation occurs [Fig. 1.3 (b)]. For very high Bjerrum length the polymer chain collapses due to the attractive interactions arising from the condensed counterions [Fig. 1.3 (c)].

1.2.1 Counterion condensation

The electrostatic interaction of PE system increases as the charge density ℓ_B increases and the counterions starts to bound to the PE chain above some critical charge density. This phenomenon is known as counterion condensation, or Manning condensation. This process was first proposed by Onsager and later analysed by Manning [46, 49, 50] and Oosawa [51]. The counterion condensation can be understand as follows. Consider a system of cylindrical rod of uniformly charged with radius R and counterions of oppositely charged as shown in Fig. 1.4. The electrostatic potential at a distance $r > R$ arising from

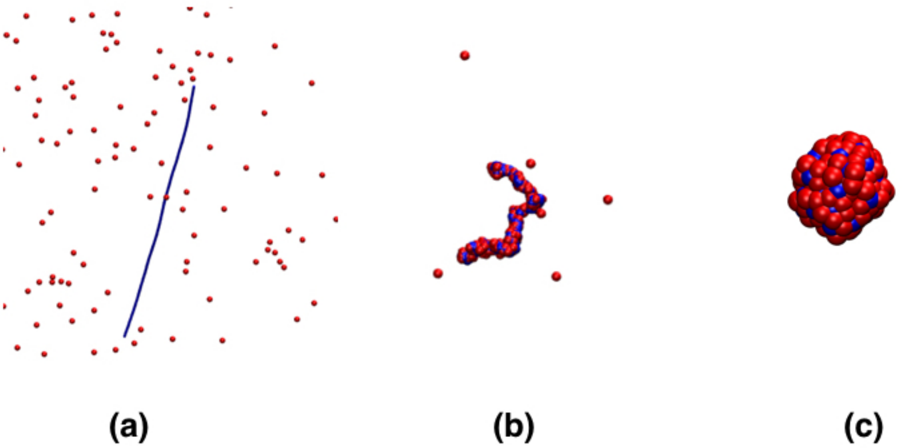

Figure 1.3: Behavior of a PE chain in good solvent at different Bjerrum length (ℓ_B). (a) At very small ℓ_B, the chain is in an extended state and the counterions are randomly distributed in the box to maximize its entropy. (b) Intermediate ℓ_B, corresponding to Manning condensation, counterion starts condensing on the chain, and the chain is in extended state irrespective of solvent quality. (c) High ℓ_B, PE chain collapses irrespective of solvent quality.

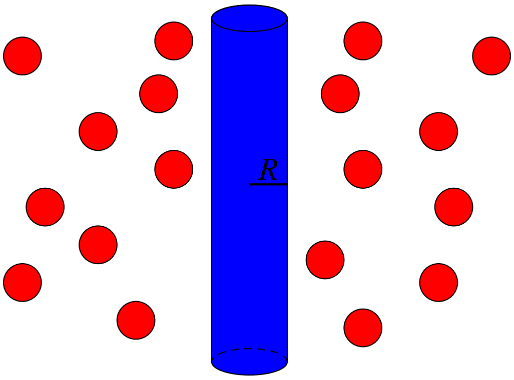

Figure 1.4: A schematic picture of a single infinite charged rod (blue) immersed in an aqueous solution containing counterions (red).

the charged rod with a linear charge density of $1/\ell$ is

$$\phi(r) = \frac{2\ell_B}{\ell} \ln\left(\frac{r}{R}\right), \tag{1.2}$$

and the counterion density can be estimated by using Boltzmann distribution as

$$n(r) \sim e^{-\phi(r)}. \tag{1.3}$$

The number of counterions inside a cylindrical shell of radius R_0 around charged rod can be calculated as

$$Q(R_0) = 2\pi \int_R^{R_0} rdr\, n(r) = \frac{2\pi}{R^{-2\ell_B^*}} \int_R^{R_0} drr^{(1-2\ell_B^*)} \sim r^{2(1-\ell_B^*)}|_R^{R_0}, \tag{1.4}$$

where $\ell_B^* = \frac{\ell_B}{\ell}$ is the dimensionless Bjerrum length and is called Manning parameter. When $\ell_B^* < 1$, $Q(R_0)$ grows with R_0 and the counterion are distributed in the entire volume, maximizing their entropy. For $\ell_B^* > 1$, $Q(R_0)$ is independent of R_0 in the asymptotic limit $R_0 \to \infty$ and therefore, counterions are bound. This phenomenon is called counterion condensation. Dependency of manning parameter on the valency is $\ell_B^* \leq Z^{-1}$, where Z is the valency [52]. In later part of this thesis, we use this manning parameter, ℓ_B^* everywhere and for notational simplicity we drop * and use ℓ_B.

1.2.2 Different measures of polymer conformations

In this section, we describe different measures that can characterize polymer conformations. A typical polymer conformation is shown in Fig. 1.5. The centre of mass of polymer chain is R_{CM} and R_i is the position of i^{th} monomer with respect to the centre of mass of chain (R_{CM}). The conformations of polymer chain can be described by following parameters.

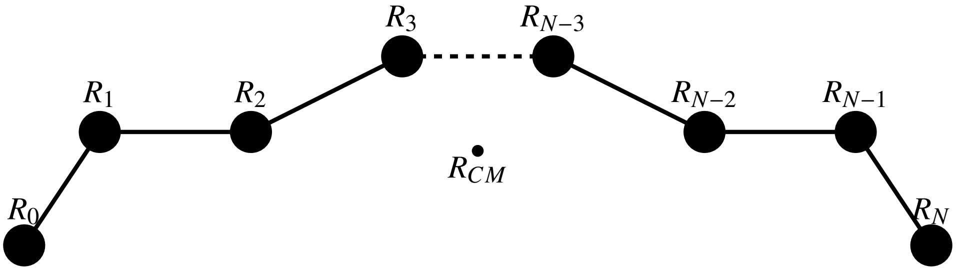

Figure 1.5: A typical conformation of a polymer chain. R_i is the position of i^{th} monomer with respect to the centre of mass of chain (R_{CM}).

- Mean square end-to-end distance, $\langle R_{ee}^2 \rangle$

$$\left\langle R_{ee}^2 \right\rangle = \left\langle (R_N - R_0)^2 \right\rangle, \tag{1.5}$$

where $\langle \rangle$ represents the ensemble or time average.

- Radius of gyration, R_g :

$$R_g^2 = \frac{1}{N} \left\langle \sum_{i=0}^{N-1} R_i^2 \right\rangle. \tag{1.6}$$

In static scattering experiments (using neutron, x-ray, light), a typically measured quantity is the radius of gyration R_g.

- Hydrodynamic radius, R_h:

$$R_h = \left(\frac{1}{N} \sum_{i=0}^{N-1} \sum_{j>i} \left\langle \frac{1}{|R_i - R_j|} \right\rangle \right)^{-1}. \tag{1.7}$$

This quantity is measured in dynamic scattering experiments.

- Shape factor R_g/R_h:

The ratio of radius of gyration (R_g) to hydrodynamic radius (R_h) is known as shape factor. It is the measure of anisotropy of the shape of the molecule and also provides structural information. The shape factor for a spherical shell with all particles are uniformly distributed on its surface is 1 where as uniformly distributed particle in a sphere has shape factor 0.77. The shape factor increases with anisotropy and takes a value about 4 for a rod-like conformation [53].

- Persistence length, l_p:

The persistence length of a polymer is a measure of the flexibility of backbone and is the length beyond which the orientations of two bonds along the chain are uncorrelated. The orientation correlation between i^{th} and j^{th} bonds decays with the distance along the chain backbone $a|j-i|$ as

$$\langle u_i . u_j \rangle = a^2 \exp\left[-\frac{a|j-i|}{l_p} \right], \tag{1.8}$$

where a is the bond length, $u_i = R_i - R_{i-1}$ and $u_j = R_j - R_{j-1}$ are the bond vectors and l_p is defined as the persistence length. For distances $a|j-i|$ smaller than l_p, the bond orientations are correlated and hence the conformation is rod-like and for distances $a|j-i|$ larger than l_p, the bond orientations are uncorrelated and hence the conformation is coil-like. The flexible chains have smaller persistence length while the rigid chains have larger persistence length. The stiff polymer in nature, ds-DNA has a persistence length of $l_p \sim 500$Å whereas the flexible synthetic polymer, polystyrene has persistence length of $l_p \sim 10-14$Å [54].

- Gyration tensor:

  The gyration tensor can be defined as

$$S_{\alpha\beta} = \frac{1}{N} \sum_{i=1}^{N} R_{i\alpha} R_{i\beta}, \ \alpha, \beta = 1, 2, 3, \tag{1.9}$$

  where $R_{i\alpha}$ is the α^{th} component of position vector R_i of i^{th} particle measured from the center of mass. Gyration tensor and its eigen values are widely used in polymer physics to describe the geometrical properties such as radius of gyration, shape anisotropy, asphericity etc. Let the eigenvalues be denoted by λ_1, λ_2, and λ_3, where $\lambda_1 \geq \lambda_2 \geq \lambda_3$. The different shape descriptors in terms of the eigen values can be expressed as

  - Radius of gyration:

$$R_g^2 = \lambda_1 + \lambda_2 + \lambda_3. \tag{1.10}$$

  - Shape anisotropy:

$$\kappa^2 = \frac{3}{2} \frac{\lambda_1^4 + \lambda_2^4 + \lambda_3^4}{(\lambda_1^2 + \lambda_2^2 + \lambda_3^2)^2} - \frac{1}{2}. \tag{1.11}$$

Shape anisotropy varies between 0 for spherically symmetric particles and 1 for all the particles lies on a line.

- Asphericity:

$$b = \lambda_3^2 - \frac{1}{2}(\lambda_1^2 + \lambda_2^2). \tag{1.12}$$

It measures, how the shape deviates from basic spherical geometry. Asphericity, b is always non-negative and $b = 0$ for spherically distributed particles.

- Acylindricity:

$$c = \lambda_1^2 - \lambda_2^2. \tag{1.13}$$

It determines how the shape varies from cylindrical shape. Acylindricity, $c = 0$ for particle distributed with cylindrical symmetry.

1.2.3 Theoretical description of a neutral polymer and charged polymer (PE)

Neutral polymer

Theoretical description of polymer using a Flory-type free energy functional is described in this section. For a neutral polymer, the contribution in free energy mainly comes from the entropic part and excluded volume interactions. In general, the free energy of a polymer chain can be written as

$$F = F_{\text{entropy}} + F_{\text{int}}, \tag{1.14}$$

where F_{entropy} is the free energy due to entropic contribution of chain and F_{int} is the free energy due to volume interaction. According to Flory, the equilibrium conformation of polymer chain is determined by the balance between volume interactions and entropic interactions [55]. In the following section, we briefly explain these terms.

The free energy due entropic elasticity of chain

To explain the entropic free energy, let us consider an ideal polymer chain in which there

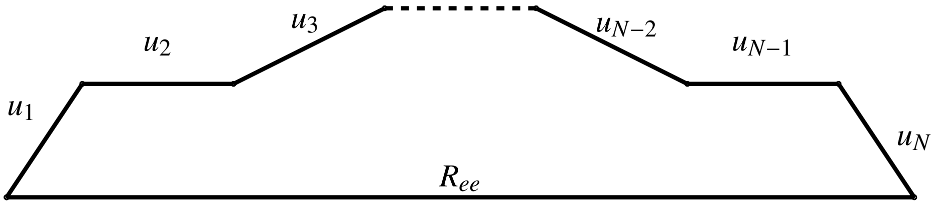

Figure 1.6: An ideal freely joined chain with N rigid segments (bonds) with bond vector u_i and the end to end distance is R_{ee}.

is no interaction between solvent or monomers of same or other polymer. An example of ideal chain is freely joined chain composed of N rigid segments as shown in Fig. 1.6, each of length l, able to direct in any direction. The motion of each segment is independent and there is no interaction between segments. The end-to-end vector R_{ee} of freely joined chain is:

$$R_{ee} = \sum_{i=1}^{N} u_i, \tag{1.15}$$

where $u_i = R_i - R_{i-1}$ is the bond vector. The mean square end-to-end distance of a freely joined chain is

$$\left\langle {R_{ee}}^2 \right\rangle = \left\langle \left(\sum_{i=1}^{N} u_i \right)^2 \right\rangle = \sum_{i=1}^{N} \langle u_i^2 \rangle + 2 \sum \sum_{1 \le i < j \le N} \langle u_i u_j \rangle. \tag{1.16}$$

Since the segments in freely joined chain are not correlated, $\langle u_i u_j \rangle = l^2 \langle \cos\theta_{ij} \rangle = 0$ and $\langle u_i^2 \rangle = l^2$. Hence the mean square end-to-end distance is

$$\left\langle {R_{ee}}^2 \right\rangle = N l^2. \tag{1.17}$$

This definition of mean square end-to-end distance is equivalent to the definition given in Eqn. (1.5).

So, for a random chain, the mean length of the chain is $R_{ee} = N^{1/2} l$, which is small compared to fully extended state $R_{ee} = Nl$. The equilibrium state of a macromolecule is an extended state with end-to-end distance of the order of $R_{ee} = N^{1/2} l$, where the entropy of chain is maximum (large number of configurations possible, whereas for $R_{ee} = Nl$, only one conformation is possible with the completely stretched case).

Since the mean size of coil is $N^{1/2}l$ and volume is $N^{3/2}l^3$, the mean concentration of monomers can be calculated as

$$n \sim N/N^{3/2}l^3 \sim N^{-1/2}l^{-3}. \tag{1.18}$$

This quantity tends to zero as the chain length increases.

From the Central Limit Theorem, the probability distribution function of a freely joint chain with N segment having end to end deistance R_{ee} is given by,

$$P_N(R_{ee}) = \left(\frac{2\pi Nl^2}{3}\right)^{-\frac{3}{2}} \exp\left[-\frac{3R_{ee}^2}{2Nl^2}\right], \tag{1.19}$$

and hence the statistical distribution of end-to-end vector of ideal chain is Gaussian and the ideal chain is also known as Gaussian chain.

The partition function of a Gaussian chain of end-to-end vector R_{ee} is

$$Z_N(R_{ee}) = N^{'} P_N(R_{ee}), \tag{1.20}$$

where $N^{'}$ is the normalizing factor which is independent of R_{ee}. The free energy of ideal chain is

$$F(R_{ee}) = -T \ln Z_N(R_{ee}) = \text{const} + \frac{3TR_{ee}^2}{2Nl^2}. \tag{1.21}$$

From Eqn. (1.21), it is seen that as the R_{ee} increases free energy also increases. The nature always tries to minimise free energy. The end-to-end distance, R_{ee} increases, implies that stretching of polymer chain, induces an elastic force in the opposite direction to minimise free energy. This is entropic in nature. One can replace R_{ee} with R_g, the radius of gyration since both the quantities are proportional.

We derived the free energy of an ideal chain which is the entropic contribution in free energy corresponding to an extended chain. As we know from the Sec. 1.2, neutral polymer has two conformations namely, extended and collapsed state. In order to derive the free energy corresponding to the entropic contribution collapsed state, let us consider an ideal macromolecule located inside a spherical cavity with diameter D much larger than the persistence length of the polymer and smaller than the length of the stretched polymer chain. Such a polymer conformation is identical to collapsed state. The entropy of such a system decreases as a result of confinement and the free energy takes the form [54]

$$F_{\text{entropy}} = Tf\left(\frac{N^{1/2}l}{D}\right), \tag{1.22}$$

where the function f is unknown, but can be evaluated by using properties of free energy. The free energy is extensive and should be proportional to N, the function $f(x) \sim x^2$, hence free energy for a collapse state is

$$F_{\text{entropy}} \sim T\frac{Nl^2}{D^2}. \tag{1.23}$$

The different polymer conformations can be recognised by measuring radius of gyration, end-to-end distance and hydrodynamic radius. All these three quantities show same scaling with respect N, and one can replace R_{ee} with R_g in the expressions for free energies, which also adds constant factors.

The free energy due to volume interaction

Role of volume interaction can be parametrized by the expansion coefficient, α, the ratio of mean square radius of gyration of the polymer chain (R_g) to that of gaussian chain (R_{g0}) is given as

$$\alpha^2 = \frac{R_g^2}{R_{g0}^2}. \tag{1.24}$$

The expansion coefficient $\alpha \gg 1$ corresponds to extended state and $\alpha \ll 1$ corresponds to collapsed state. Since the monomer concentration in the extended state is low as in Eqn. (1.18), the thermodynamic function can be expanded into power series of the number of particles in the unit volume ie., virial expansion. The free energy F_{int} can be expanded in terms of virial expansion as

$$\frac{F_{\text{int}}(\alpha)}{T} \sim R_g^2 B\left(\frac{N}{R_g^3}\right)^2 + R_g^3 C\left(\frac{N}{R_g^3}\right)^3 + \text{............}, \tag{1.25}$$

where B and C are second and third virial coefficients respectively, and are defined by the interaction potential. Equation (1.25) can be written in terms of expansion coefficient α as follows:

$$\frac{F_{\text{int}}(\alpha)}{T} \sim \left(\frac{BN^{1/2}}{l^3}\right)\alpha^{-3} + \left(\frac{C}{l^6}\right)\alpha^{-6} + \text{............} \tag{1.26}$$

The second-virial coefficient is a measure of the strength of two-body interactions $u(r)$, and is given by

$$B(T) = \frac{1}{2}\int\left\{1 - \exp\left[-\frac{u(r)}{T}\right]\right\} d^3r. \tag{1.27}$$

In good solvent condition, the effective interaction between the monomers are repulsive and hence $B(T)$ is positive whereas in the poor solvent, attractive interaction between the monomer leads to negative $B(T)$.

The entropic free energy defined in Eqns. (1.21) and (1.23) can be written in terms of expansion coefficient α as follows:

$$\frac{F_{\text{entropy}}(\alpha)}{T} = \begin{cases} aR_g^2/Nl^2 \sim \alpha^2, & \alpha \gg 1, \\ Nl^2/R_g^2 \sim \alpha^{-2}, & \alpha \ll 1. \end{cases} \tag{1.28}$$

Combining the two limiting cases by interpolation, we get

$$\frac{F_{\text{entropy}}(\alpha)}{T} \sim \alpha^2 + \frac{1}{\alpha^2}, \tag{1.29}$$

where $\alpha \gg 1$ corresponds to swollen (extended) state and $\alpha \ll 1$ correspond to collapsed state. The total free energy of a neutral polymer in terms of swelling parameter can be written as

$$F \sim \alpha^2 + \alpha^{-2} + \left(\frac{BN^{1/2}}{l^3}\right)\alpha^{-3} + \left(\frac{C}{l^6}\right)\alpha^{-6} + ..., \tag{1.30}$$

The equilibrium value of α, the swelling parameter can be calculated by minimizing the total free energy with respect to α. From α one can find the relation between R_g and N. For an extended chain, the scaling relation is $R_g \propto N^{3/5}$ whereas for a collapsed chain, the scaling relation is $R_g \propto N^{1/3}$.

Polyelectrolytes

The Flory like theory for a PE was first introduced by Kuhn et al [56]. The free energy expression contains all terms as in the case of neutral polymers and the one corresponding to electrostatic interactions. This electrostatic interactions are relevant only at large Bjerrum length(ℓ_B), at small Bjerrum length (ℓ_B), the PE chain behaves essentially as neutral polymer.

The electrostatic interaction part of free energy can be evaluated by neglecting the connectivity of the polymer chain and assuming that the monomers are uniformly distributed within the chain volume V_{ch} [57]. Due to the electrostatic interactions, the chain elongates and forms an ellipsoid shape with its longitudinal diameter equal to the end-to-end distance of an ideal chain. The electrostatic contribution of such an uniformly charged ellipsoid with net charge efN can be written as

$$\frac{F_{\text{el}}}{k_B T} \sim \frac{\ell_B (fN)^2}{R_{ee}} \ln\left(\frac{R_{ee}}{lN^{1/2}}\right). \tag{1.31}$$

The PE free energy will be described in more detail in Chapter 3.

1.2.4 Simulation models of polymers

This section provides an overview of some of the popular computational models used today in the field of simulation of polymers. The length scale of polymer ranges from several Å to nano meter and the time scale required for simulation varies from femtoseconds to hours depends on the required material properties. A single model can not achieve all these requirements, hence we use different models which represents different length and time scales as illustrated in Fig. 1.7. The models have basic units as electrons (quantum chemistry), atom (force field), monomers or group of monomers (mesoscopic models), entire polymer chain (soft fluids), or volume elements (finite elements). As we can see from the Fig. 1.7, the time and length scales at which one can simulate a particular model, increases as we reduce the number of degrees of freedom. These models can be quantum or classical with respect to their number of degrees of freedom. Choosing the correct model depends on the objective of the problem. For example: chemical reaction studies need the information regarding electronic wave function and one has to use quantum chemical methods with a few atoms and simulate for a small duration. On the other hand, many physical properties such as diffusion constant do not need electronic properties or atomistic properties. Instead, one has to simulate bigger systems for longer times. In such cases mesoscopic models are good enough. Models which involve atomic or subatomic levels are computationally very costly. The brief description of some models are described in the following sections.

Models with Electronic Degrees of Freedom - quantum mechanical models

The most fundamental level of modeling of polymeric system include the electronic degrees of freedom, which are responsible for the properties like polymerization stereochemistry, electronic conductivity, non-linear optical properties, photochemistry etc. These models treat the electronic wave function quantum mechanically within the frozen-nuclei approximation through Born-Oppenheimer approximation. The Born-Oppenheimer

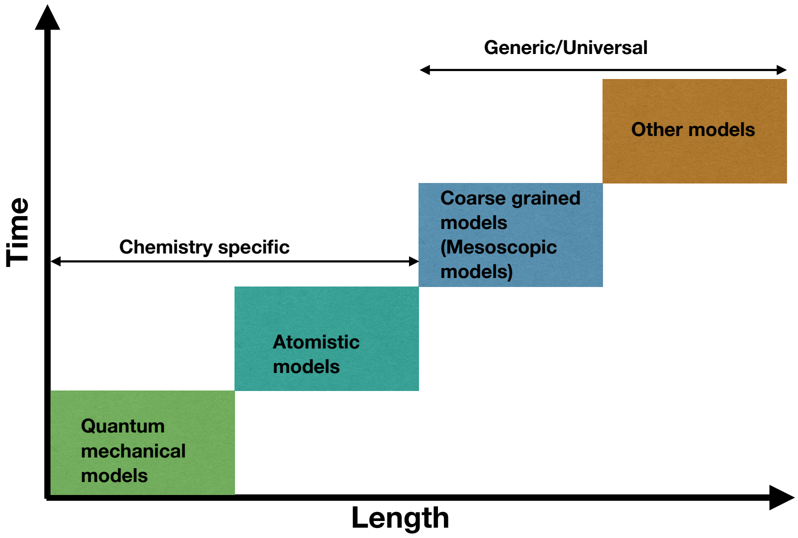

Figure 1.7: The schematic representation of length and time scales associated with different models.

approximation separates the electronic and nuclear motion [58] and hence one can write a separate equation of motion for the electronic degrees of freedom with the nuclear positions entering only as parameters and not as dynamic degrees of freedom. At the next level of approximation, only nuclear degrees of freedom and their mutual interactions are treated according to classical mechanics.

Chemically Realistic Models of Polymers - Atomistic models

Chemically realistic models consider the nuclear positions and potentials to develop a model which is classical in nature. These models do not consider electronic degrees of freedom explicitly. The time step used in the simulations depends on the highest frequency present in the systems *ie.*, time step should be less than the inverse of the bond vibration frequency present in the system. The potentials in the system include both bonded and non bonded interactions which are described in detail in Sec. 2.3. In atomistic models the chemical structure of all constituents are reproduced. In such models, each interacting site represents a constituent atom, bonded to others in accordance with chemical composition. The parameters in the interactions are obtained either from experiments or from quantum mechanical calculations. Atomistic simulation are limited by time taken for each of simulation and number of particle as well.

Coarse-Grained Models

Polymers have many common mesoscopic characteristics which are independent of the atomistic structure of the chemical repeating units. For instance, the self-similar structure of polymers in solutions or melts at large length scales is only characterized by the chain's end-to-end distance. Hence one can neglect the chemical details of the system and use a coarse-grained description. In coarse-grained simulations, a group of atoms or molecules is treated as a single force centre hence decrease the number of force sites and thus reduce computational requirements for molecular simulation. While these models are successful in describing structural properties, dynamic evolution is faster than the corresponding atomistic simulations or experiments. Implementation of coarse-grained models involves two major steps. The first is mapping of all-atom system onto a coarse-grained representation. The second is optimizing the effective interactions between coarse-grained sites. Similar to empirical potentials scheme, coarse-grained interactions are optimized to reproduce certain structural and thermodynamic properties of reference all-atom system. This second stage is more challenging and there are several systematic coarse-graining techniques developed to address it, such as iterative Boltzmann inversion, force-matching, inverse Monte Carlo etc [59].

The coarse-grained models can be classified as off-lattice models and lattice models. The examples of off-lattice models include pearl necklace model of either of the tangent hard-sphere type, where the bond lengths between neighboring pearls along the chain can vary freely within tight limits, or of the bead-spring type, where neighboring beads are connected by anharmonic springs (refer Sec. 1.2.3). Another example of an off-lattice model consists of ellipsoidal repeating units. Lattice models of polymer solutions are simple and computationally efficient realization, and therefore they have interest both for single chain simulations as well as for simulations of polymer solutions and melts [60–63]. In simple lattice models, a small group of atomistic repeating units is represented by a site on a simple cubic lattice or any other lattice. These monomers undergoes self avoiding random walk on lattices. Required conditions may apply externally for the movement of monomers. The main disadvantage of lattice models is that only the configurational part of the partition function can be investigated. The earliest lattice model, bond fluctuating model defined on a cubic lattice with a monomer occupies in eight lattice sites in three dimension (four sites in two dimension) and the bond distances and angles are allowed to vary between different discrete possibilities [64]. The movement restricted such as not to overlap the different polymer chains.

In the higher degree of coarse-graining, one consider entire polymer chain as a single unit such models are called soft fluid and the one consider volume element as the basic unit is called finite elements method.

Computational model for PE and solvent

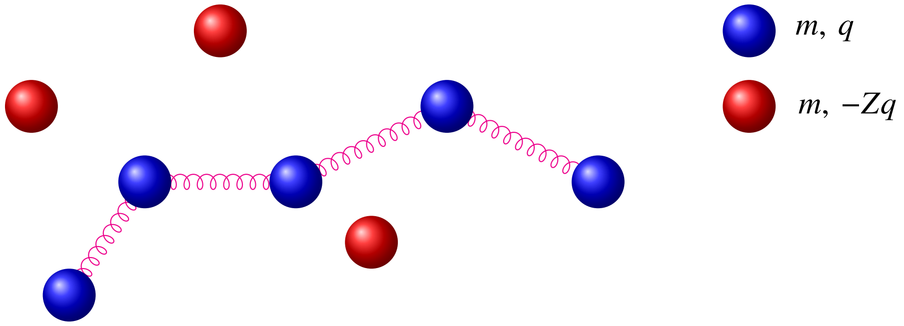

Figure 1.8: Bead-spring model of a PE chain and counterions. The monomer is represented by blue spheres and the counterion by red spheres. m and q are mass and charge respectively. Z is the valency of counterions.

In this thesis, PEs are modeled by a coarse-grained model called bead-spring model. The monomers (group of atoms), the smallest repeating units, are represented as spheres and are connected by springs as shown in Fig. 1.8. Each monomer has a charge q, unit mass and radius. The counterions are also spheres of unit mass and various radii depending on the problem. The charge and number of the counterions are such as to neutralize the system.

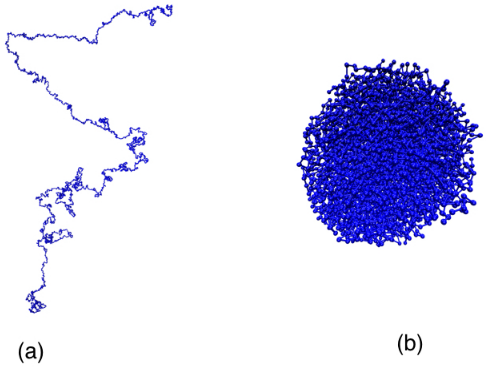

Figure 1.9: Polymer of length N=5000 (a) in good solvent (b) poor solvent.

In general, solvents can be classified as good and poor solvents. In good solvents, the solute particle has affinity with the solvent particle. A polymer in a good solvent is likely to be in a coil/extended/swollen state [Fig. 1.9 (a)], whereas in a poor solvent, solute and solvent particles ’dislike’ each other. A polymer is likely to be in a globule/collapsed configuration in a poor solvent [Fig. 1.9 (b)]. By changing the temperature one can move from one solvent quality to the other. The solvent can be simulated in explicit as well as implicit models. In explicit solvent simulations of protein, water is represented by all-atom force field models or by coarse-grained models. Currently several water models are being used in bio-molecular simulations such as SPC,SPC/E,TIP3P,TIP5P. Each of these models are optimized to one or more physical properties of water, such as radial distribution function, diffusivity, density anomaly etc. But none of these models can simultaneously reproduce all properties. The presence of water molecules in the system increases the number of degrees of freedom by more than 1000. Coarse-grained (CG) models are less structured representations of a molecule obtained by mapping two or more atoms onto a single interaction site. i.e. the entire water/solvent molecule is mapped to one coarse-grained bead located at the centre of mass of the water/solvent molecule.

Significant speed-ups are obtained due to lesser number of degrees of freedom, simpler, softer potentials and larger time steps. Simulations will be simplified with coarse grained models of water.

In implicit solvent method, the interaction between the solute particles determine the quality of the solvent. The interaction between the monomers are taken to be attractive for poor solvents and are taken to be repulsive for good solvents. There is no solvent particle in the system. We use implicit solvent method in all our simulations.

1.3 Contribution of this thesis

This thesis is divided into two parts. The first part addresses the mechanism that drives the collapse transition of a single PE from an extended to a collapsed phase. The second part studies the statics and dynamics of aggregation in a collection of PEs, both flexible and rigid. Both these problems are studied primarily using extensive molecular dynamics (MD) simulations of coarse-grained models. A brief introduction to these problems is given below.

1.3.1 Extended-collapse transition in PEs

Several experiments and simulations have shown that the PE chain undergoes a transition from extended to collapsed conformation above critical charge density [10–15,57,65–67]. This transition is independent of the solvent type, though the configuration of charged polymer at very low charge density and the critical charge density corresponding to this transition depends purely on the nature of the solvent. Other than the solvent the counterion properties such as valency, size, shape etc are also crucial in determining critical charge density for transition. Collapsed state of PE can be found in the biological world, for example, RNA or DNA are densely packed in cells and viruses [68–70]. Ex-

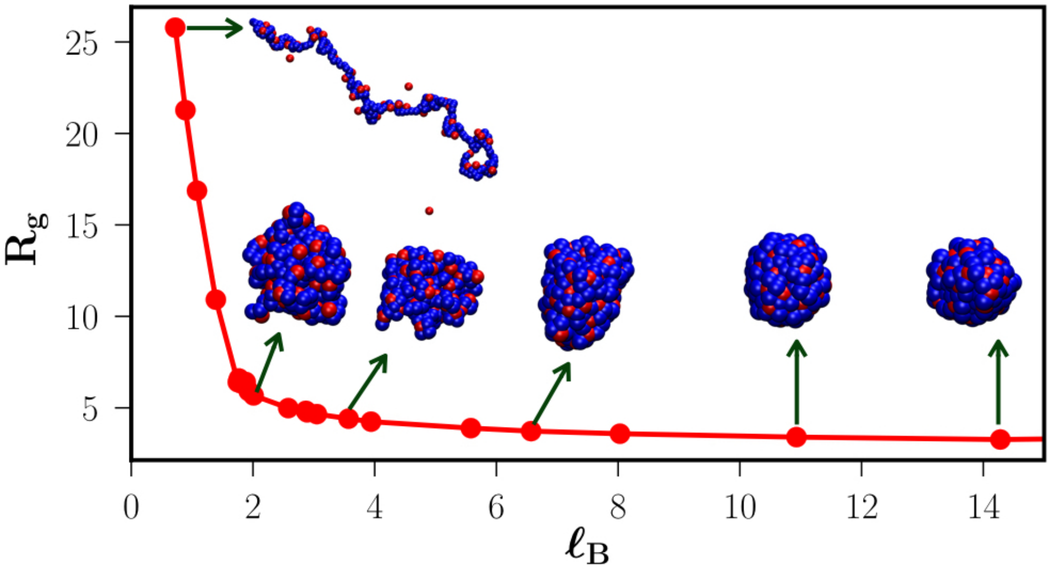

Figure 1.10: The extended to collapsed transition of PE: Radius of gyration as a function of charge density for a PE with trivalent counterions in a good solvent condition. Snapshots corresponds to different charge density is shown. Note that the snapshots are not scaled same for clarity. Polymer chain is represented in blue color and counterions are in red color.

tended to collapse transition was first observed in experiments, where it was found that DNA molecules collapse in to highly compact configurations upon the addition of multivalent counterion [71]. The order of this phase transition is shown to be first order in nature [14, 15, 72, 73].

The variation of radius of gyration with the charge density for a PE with trivalent counterion in a good solvent from our simulations is shown in Fig. 1.10. The first snapshot corresponds to the PE with fraction of counterion condensed on it and in extended state with high radius of gyration (R_g). As ℓ_B increases, R_g decreases corresponding to the extended to collapsed transition. Another important aspect regarding extended-collapse-transition is that the pathway of transition. In neutral polymers several theories says different mechanism of transition with different intermediate state such as peal necklace phase [74–77]. Whether such transition pathway exists in the case of PE chain is an unanswered question.

1.3.2 Aggregation of multiple PEs

In the dilute system of PE chains, each chain is surrounded by the cloud of oppositely charged counterions. The resident charges in the PE chain and counterion cloud cause repulsion between them, whereas, when the charge clouds overlap, then the respective PE chains attract. This happens above a critical charge density, which is different from the critical charge density corresponds to extended to collapse transition. These counterion mediated attraction is observed in nature as well, for example, biologically relevant charged polymers such as DNA, actin and microtubules, may aggregate into bundles in the presence of counterions [2, 78–82]. The double stranded DNAs in solution repel each other due it's like charge and the addition of counterion decreases their repulsion as the concentration of counterions increases and turns attractive above critical concentration [83, 84]. F-actin has large persistence length and can be treated as a rigid PE and is anionic in nature. In the presence of divalent counterions, F-actin filaments will drive the ordering of close-packed bundles of twisted filaments [85]. The PEs aggregates irrespective of chain flexibility, flexible biological polymers such as proteins show aggregation and the protein-protein disordered aggregates cause many neurodegenerative diseases [86, 87]. Depending on the concentration of multivalent ions, different phases observed in the case of PEs system such as isolated rods, aggregated networks of rods and aggregated bundles of rods [88–100]. Aggregation of multiple PEs has been studied extensively [2, 89–118]. The different simulation studies shows that the finite sized bundles is the equilibrium state for intermediate value of charge density and phase separated state for the large charge density [92, 93]. Now the question of interest is regarding the equilibrium state of multiple PE aggregation, whether it is phase separated state or finite size bundles and also how do the dynamics of aggregation changes with different system properties such as valency, charge density, monomer density, chain length, flexibility etc..

1.3.3 Organisation of thesis

The rest of the thesis is organized as follows. The molecular dynamics (MD) simulation technique is described in chapter 2. Brief description of algorithm, various bonded and non bonded interaction, model for PEs and different technique for thermostatting are described in this chapter.

In chapter 3, mechanism of collapse of PE irrespective of solvent quality is described. The nature of the effective attractive interactions driving the extended to collapse transition is not well-understood and there are competing theories explaining their origin. For the collapsed state, these theories predict that the gyration radius, R_g, of a PE has the scaling form $R_g \sim N_m^{1/3} \ell_B^{-\gamma}$, where N_m is the PE chain length, and the exponent γ can potentially depend on system parameters. In the literature, there are three theoretical approaches [15–18], based on different physical models, to account for the electrostatics-driven counterintuitive collapse of similarly charged PEs. All the theories predict a single collapsed regime, but differ in their prediction of the exponent γ characterizing the dependence of R_g on ℓ_B. We present the results of extensive MD simulations exploring the collapsed conformation of a single flexible PE chain in both good and poor solvents and trying to identify the possible theory to explain the mechanism of collapse.

The behaviour of system of multiple PEs are described in chapter 4 and 5. Chapter 4 explains the aggregation dynamics of rigid PEs, where, the simulation results suggest that, though the system of PEs and counterions interact via long-range Coulomb interactions, the effective attractive interactions between the aggregating polymers are short-ranged. The aggregation dynamics, monitored through the decay of number of aggregates with time, is shown to behave like a power law $t^{-\theta}$, where θ is shown to be independent of the charge density of the polymers, the valency of the counterions, the length and the number density of the rigid polymers. Using these simulation results, the aggregation of rigid PEs is modeled using Smoluchowski coagulation equation for irreversible aggregation of particles of different masses. From this modeling, we obtain $\theta = 2/3$, in close agreement with MD simulation data (θ=0.62) strengthening the argument of effective short-range interactions in rigid PE systems. We also find that the morphology of the aggregates and the mode of merging of aggregates is not unique and depends critically on the charge density of the polymers. For lower charge density, the aggregates are cylindrical in shape, and they change to a more elongated collinear shape at higher charge density.

In chapter 5, phase diagram and dynamics of aggregation of flexible PE is described. The introduction of flexibility alters the aggregation dynamics, as additional time scales emerge due to the possibility of the system getting trapped by kinetic barriers. Unlike rigid PEs, the phase diagram of the flexible charged polymers is rich and depends on the charge density of the polymer. Three different phases are observed: one with no aggregation, another with finite bundles and a fully phase-separated phase. The additional time scales are reflected in the power law exponent with the value of exponent depending on the charge density, unlike the rigid charged polymers. These results underscore the crucial role of flexibility in the emergence of a rich phase behavior.

In chapter 6, the results of this thesis are described.

Chapter 2

Simulation methods

In this chapter, a brief introduction to both molecular dynamics (MD) simulations is given.

2.1 Molecular dynamics simulation

Molecular dynamics (MD) simulations determine the time evolution of a set of interacting particle by integrating their equations of motion. Since the microscopic configuration is known at all times, the macroscopic properties may be read out at any time.

Classical MD simulations of atomic systems is based on the Born-Oppenheimer approximation (BOA) [58]. Consider a system of electrons of charge e with mass m and atomic nuclei (N) of mass M, the hamiltonian of such a system can be written as

$$H = K_N(\mathbf{R}) + K_e(\mathbf{r}) + P_{Ne}(\mathbf{R},\mathbf{r}) + P_{NN}(\mathbf{R}) + P_{ee}(\mathbf{r}), \tag{2.1}$$

where $K_N(\mathbf{R})$ and $K_e(\mathbf{r})$ are the kinetic energy terms of the nuclei and the electrons respectively. $P_{Ne}(\mathbf{R},\mathbf{r})$, $P_{NN}(\mathbf{R})$, $P_{ee}(\mathbf{r})$ are the potential energy terms of nucleus - electron interaction, nuclei-nuclei interaction and electron-electron interaction respectively. The system is described by the Schrödinger equation, $\hat{H}\Psi = i\hbar\frac{\partial\Psi}{\partial t}$, where $\hat{H}$ is the hamiltonian operator and the wave-function Ψ is a function of the co-ordinates of both the nuclei and the electrons. Solving the Schrödinger equation for a many particle system is both time and memory consuming, and many approximations are used to simplify the problem. One of the most important approximations is the BOA, which is based on the large difference between the masses of the nuclei and electrons. Due to the comparatively large mass, the nuclei move slowly compared to electrons, and they may be treated as stationary. Since the electrons move fast in the field of nuclei, this leads to a difference in the time scale of the motion of electrons and the nuclei, and according to BOA, one can treat the motion of electron and nuclei independently. So the wave function can be written as the product of individual wave function as follows:

$$\Psi(\mathbf{R},\mathbf{r}) = \chi(\mathbf{R}).\psi(\mathbf{r}), \tag{2.2}$$

where $\chi(\mathbf{R})$ is the wave function of the nuclei and $\psi(\mathbf{r})$ is that of the electrons. Under BOA, the motion of nuclei can be treated classically, with nuclei moving in an averaged background potential due to electrons. The dynamics are governed by Newton's equations of motion

$$m_i\ddot{\mathbf{r}}_i = -\frac{\partial U(\mathbf{r_i})}{\partial \mathbf{r}_i}, \tag{2.3}$$

where m_i is the mass of the i^{th} nucleus at position $\mathbf{r}_i$ and $U(\mathbf{r_i})$ is the potential experienced by the i^{th} nucleus, due to the presence of all other nuclei. The classical MD simulation solves Newton's equations of motion numerically.

2.2 Measurements and the ergodic hypotheses

The average value of observables in the system can be measured in two ways, ensemble average and time average. The time averages of the measured quantity A is given by

$$\langle A \rangle_t = \lim_{\tau \to \infty} \frac{1}{\tau} \int_0^{\tau} A[q(t), p(t)] dt. \tag{2.4}$$

On the other hand the ensemble average is given by

$$\langle A \rangle_e = \frac{\int A[q(t), p(t)] \rho[q(t), p(t)] \, dqdp}{\int \rho[q(t), p(t)] \, dqdp}, \tag{2.5}$$

where $\rho[q(t), p(t)]$ is phase space density at the volume element $dqdp$. According to the ergodic hypotheses, in equilibrium, the time average of a quantity which is obtained by repeated measurement in the same system, and the ensemble average obtained from measuring each system of an ensemble just once, is the same, *i.e.*

$$\langle A \rangle_t = \langle A \rangle_e. \tag{2.6}$$

The ergodic hypothesis is used in MD as well as Monte Carlo (MC) simulations for taking averages of quantities in different ensembles.

2.3 Interactions in the system

The problem of finding a realistic potential that would mimic the true energy surfaces is nontrivial. In MD, empirical potentials with a specific functional form and parameters represent the physics and chemistry of the systems of interest. The parameters are chosen such as to get a good fit to realistic potentials. Quantum mechanical calculations, iterative algorithms and data from experiments are used for this purpose. A typical force field takes the form

$$U(r_1, r_2..., r_N) = \sum_{\text{bonds}} \frac{1}{2}K_b(r_{ij} - b)^2 + \sum_{\text{angles}} \frac{1}{2}K_\theta(\theta_{ijk} - \theta_0)^2 + \sum_{\text{torsions}} k_\phi[1 + \cos\phi_{ijkl}] \quad (2.7)$$
$$+ \sum_{\text{atom pairs}} 4\varepsilon_{ij}\left[\left(\frac{\sigma_{ij}}{r_{ij}}\right)^{12} - \left(\frac{\sigma_{ij}}{r_{ij}}\right)^{6}\right] + \sum_{\text{atom pairs}} \frac{q_i q_j}{4\pi\epsilon_0\epsilon_r r_{ij}}.$$

In the first three terms the summation indices run over all the bonds, angles and torsion angles defined by the chemical nature of the system through covalent bonds, whereas in the last two terms the summation indices run over all pairs of atoms which are not bonded chemically.

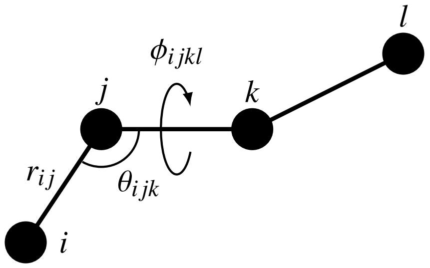

Figure 2.1: Schematic description of the parameters in bonded interactions using a simple chain.

1. **Bonded interactions:** The first term in Eqn. (2.7), a harmonic bond potential, represents the bond interaction energy between i^{th} and j^{th} covalently bonded particle separated by a distance r_{ij}. b is the equilibrium bond length, and K_b is the force constant associated with the bond. The second term in Eqn. (2.7) represents the interaction energy corresponding to the bond angle defined between two adjacent bonds making an instantaneous angle θ_{ijk} and equilibrium angle θ_0. K_θ is the force constant associated with the angle. The third term represents potential involving the angle between planes containing particles i, j, k and j, k, l and is known as torsion interaction or dihedral interaction. This interaction constraints the rotation around a bond. The schematic representation of different bonded interactions is shown in Fig. 2.1.

2. **Non-bonded interactions:** The non-bonded interactions in Eqn. (2.7) consist of van der Waals (fourth term) and electrostatic (last term) interactions. Non-bonded interactions applies to pairs of sites separated at-least by four covalent bonds, since bonded interactions are separated by at-most three covalent bonds. Specific environmental effects can be accounted by properly adjusted partial charges q_i (and an effective value of the constant ϵ_0) as well as the LJ parameters ε_{ij} and σ_{ij}. The non-bonded interactions are assumed to be pairwise additive.

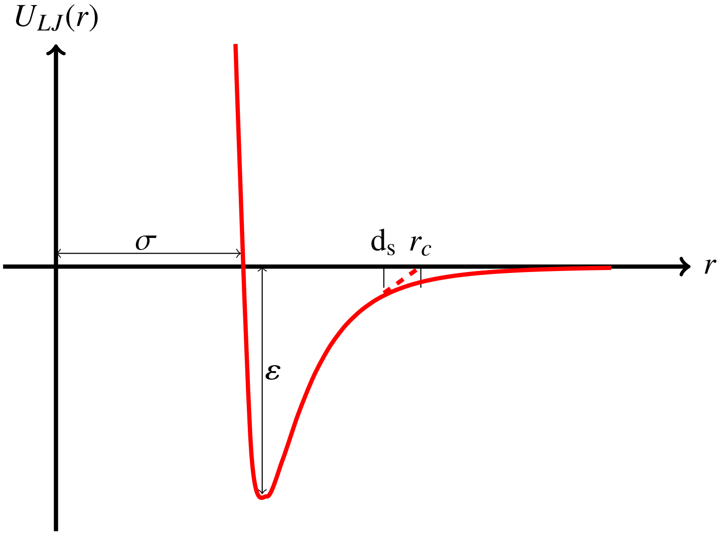

Figure 2.2: The form of LJ potential and the different parameters.

In excluded volume interaction, r_{ij} is the distance between particles i and j, ε_{ij} is the minimum of the potential and σ_{ij} is the inter-particle distance at which the potential is zero. The LJ interaction is zero at infinite separation of particle and as the separation is reduced, the interaction turns attractive and attains a minimum, ϵ_{ij}. As the separation is further reduced, below σ_{ij}, the interaction turns strongly repulsive, which prevents overlap between the pairs. A schematic representation of LJ potential is shown in Fig. 2.2. LJ parameters are usually defined for identical particles and for non-identical particle one can calculate the parameters using the

Lorentz-Berthelot mixing rule [119] as follows:

$$\varepsilon_{ij} = \sqrt{\varepsilon_{ii}\varepsilon_{jj}} \qquad \sigma_{ij} = \frac{1}{2}[\sigma_{ii} + \sigma_{jj}]. \tag{2.8}$$

LJ interaction is considered to be short range for all practical purposes and the interaction is chosen to be zero beyond a cut-off distance r_c for better computational efficiency. This can be done by using a switching function to truncate the potential smoothly at the cut-off distance. The switching starts at a distance called switch distance $\mathrm{d_s}$ (see Fig. 2.2) which is always less than the cut-off distance. The switching function helps the LJ potential to truncate to zero smoothly and hence avoids the discontinuity associated with force and conserves energy.

The second non-bonded interaction is the electrostatic (Coulomb) interaction, where q_i and q_j are the charges of i^{th} and j^{th} particle separated by a distance r_{ij}, ϵ_0 is the permittivity of free space and ϵ_r is the relative permittivity of media. The Coulomb interactions are long-range in nature and hence computing this interaction is the most computationally intensive in MD simulation. Different techniques are used for this purpose and are explained in Sec. 2.6.

2.4 Algorithms for integrating the equations of motion

The potential energy is a function of the positions of all atoms and it is hard to solve the equations of motion analytically. In 1967, L. Verlet introduced a simple algorithm to solve these equations numerically [120] and this algorithm is known as Verlet algorithm. The solution of Newton's equations using the Verlet algorithm is based on a Taylor series expansion. We explain the Verlet algorithm using a single particle problem. Let $r(t)$ be the position of the particle at time t. Using Taylor series expansion up to the second-order term, one can write the expression for the position at later $(t + \delta t)$ and previous $(t - \delta t)$

times as

$$r(t+\delta t) = r(t) + \dot{r}(t)\delta t + \frac{1}{2!}\ddot{r}(t)\delta t^2 + \frac{1}{3!}\dddot{r}(t)\delta t^3 + O(\delta t^4), \tag{2.9}$$

$$r(t-\delta t) = r(t) - \dot{r}(t)\delta t + \frac{1}{2!}\ddot{r}(t)\delta t^2 - \frac{1}{3!}\dddot{r}(t)\delta t^3 + O(\delta t^4), \tag{2.10}$$

where $\dot{r}(t) = v(t)$ is the velocity and $\ddot{r}(t) = \frac{f(t)}{m}$ is the acceleration. Adding Eqns. (2.9) and (2.10) removes the velocity term and gives an expression for the position at time $t+\delta t$ as

$$r(t+\delta t) = 2r(t) - r(t-\delta t) + \frac{f(t)}{m}\delta t^2 + O(\delta t^4). \tag{2.11}$$

Equation (2.11) is straightforward and easy to implement in simulations. Note that the Verlet algorithm relies on two previous time steps, t and $t-\delta t$, to find the solution forward in time $t+\delta t$, and it is a fourth-order method.

This algorithm does not directly calculate velocity. This may be a problem if properties of the system that depend on velocity, such as kinetic energy, are desired. The velocity can be calculated using equation

$$v(t) = \frac{1}{2(\delta t)}[r(t+\delta t) - r(t-\delta t)]. \tag{2.12}$$

The velocity at time t can be calculated only after calculating $r(t+\delta t)$. So the calculation of velocity is one step behind and this is the main drawback of this algorithm. Later Swope et al [121] modified the Verlet algorithm such as to get both position and velocity together, which is known as velocity Verlet algorithm. Velocity Verlet algorithm can be derived as follows. The Newton's equation of motion is a second order equation and can be written as two first order equations as

$$\dot{r}(t) = v(t), \tag{2.13}$$

$$\dot{v}(t) = \frac{f(t)}{m}. \tag{2.14}$$

Using Taylor series expansion,

$$r(t+\delta t) = r(t) + \dot{r}(t)\delta t + \frac{1}{2!}\ddot{r}(t)\delta t^2 + O(\delta t^3),$$

$$r(t+\delta t) = r(t) + v(t)\delta t + \frac{1}{2!}\frac{f(t)}{m}\delta t^2 + O(\delta t^3). \tag{2.15}$$

Similarly, Taylor expansion for velocity can be written as

$$v(t+\delta t) = v(t) + \dot{v}(t)\delta t + \frac{1}{2!}\ddot{v}(t)\delta t^2 + O(\delta t^3). \tag{2.16}$$

We can use $\frac{f}{m}$ to eliminate $\dot{v}$, but we need to develop an expression for $\ddot{v}$ in terms of known quantities. This can be done by expanding $\dot{v}(t+\delta t)$

$$\dot{v}(t+\delta t) = \dot{v}(t) + \ddot{v}(t)\delta t + O(\delta t^2).$$

On rearranging we get

$$\frac{1}{2}\ddot{v}(t)\delta t^2 = \frac{1}{2}[\dot{v}(t+\delta t) - \dot{v}(t)]\delta t + O(\delta t^3). \tag{2.17}$$

Now the expression for $v(t+\delta t)$ becomes

$$v(t+\delta t) = v(t) + \dot{v}(t)\delta t + \frac{1}{2}[\dot{v}(t+\delta t) - \dot{v}(t)]\delta t + O(\delta t^3),$$

$$v(t+\delta t) = v(t) + \frac{1}{2}[f(t+\delta t) + f(t)]\delta t + O(\delta t^3). \tag{2.18}$$

In the velocity Verlet algorithm, positions and velocities are calculated simultaneously with the expressions (2.15), (2.18).The algorithm is implemented in the following steps:

1. positions at $(t+\delta t)$ are calculated according to Eqn. (2.15).

2. velocity at $(t+\frac{\delta t}{2})$ is calculated using

$$v\left(t+\frac{\delta t}{2}\right)=v(t)+\frac{f(t)}{2m}\delta t. \tag{2.19}$$

3. force at $(t+\delta t)$ is computed based on $r(t+\delta t)$.

4. velocity at $(t+\delta t)$ is calculated using

$$v(t+\delta t)=v\left(t+\frac{\delta t}{2}\right)+\frac{f(t+\delta t)}{2m}\delta t. \tag{2.20}$$

2.5 Boundary conditions

In a finite system with boundaries, the particles at the boundary experience a different environment than those in the bulk, which changes the accuracy of measurements. In order to avoid this surface effect, we simulate the system with periodic boundary conditions, by placing a virtual box in all three cartesian directions, completely filling space and this virtual box is an exact replica of the original box. In simulations, a particle moves in the original box, its periodic images in each of the neighboring boxes also move in a concerted manner by the same amount and in the same fashion. As the simulation evolves, atoms can move through the boundary of the simulation cells. When this happens, an image atom from one of the neighboring cell enters to replace the lost particle. This process in two dimensions is illustrated in Fig. 2.3, where the original box is shown in blue and all other boxes are images. When a particle in the central box, numbered 1, moves across the boundary, all its images also moves across boundary. The image numbered 2, from the lower box enters from the lower box to the original box and replaces particle 1. Thus the particle does not feel any boundary and the total number of particles in each box is always conserved. In order to calculate the interactions involving particle 1, we must consider the interactions between every other particle in the simulation box. In principle, we should include the interactions between all the images in the nearby boxes as well which leads

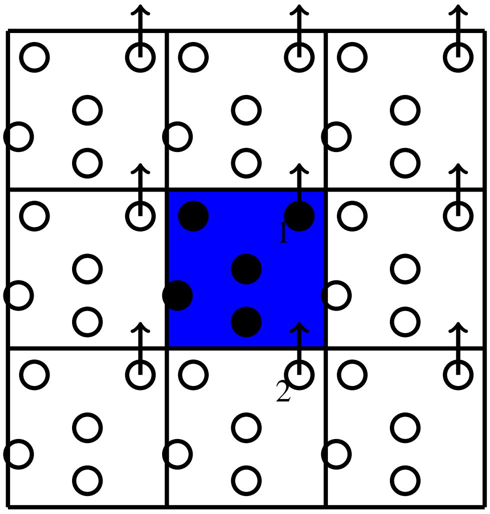

Figure 2.3: Illustration of periodic boundary condition in two dimension. The original box is shown in blue and all other boxes are images. Particle number 1 in the blue box is moving to the upper box whereas the image particle labelled 2 is coming to the blue box from the lower box, thus the particle does not feel any boundary.

to an infinite number of terms in the interaction. This is practically impossible and one should make constraints on the summation. To consider the interactions involving particle 1, we can fix the particle position as center of a box of same size and geometry as the original simulation box and consider interactions of particle 1 between all other particle within that box. There will be N-1 terms in the interaction. This is called minimum image convention. For short range potentials, the contributions come only from the nearest neighbors hence we can introduce a spherical cut-off r_c for calculating the potential.

2.6 Calculation of long-range interactions

Interactions which decay slower than r^{-d} are treated as long-range interactions, where d is the dimension of the system [122]. In three dimensions, electrostatic interactions are long-range interactions. The calculation of long-range interactions, in the presence of periodic boundary conditions is difficult since it involves interactions among infinite number of particles. In order to overcome this issue, there are different algorithms such as Ewald summation and particle particle / particle mesh (PPPM) algorithm. All the simulations mentioned in this thesis use PPPM. The main concept behind these two methods is that the long-range behaviour in real space becomes shortrange in the corresponding Fourier space.

2.6.1 Ewald summation

The basic concept of Ewald summation is splitting the potential into long-range and short-range parts by adding and subtracting a Gaussian distribution of charge [123]. The short-range interaction in real space is evaluated in real space itself and the long-range interaction in real space is evaluated in Fourier space.

The total Coulomb interaction energy due to N particles, each particle at position r_i having charge q_i is

$$V_{el} = \sum_{(i,j)} \frac{q_i q_j}{|\mathbf{r}_{ij}|}, \tag{2.21}$$

where $r_{ij} = r_j - r_i$ and the sum is over all pairs ($N(N-1)/2$ pairs in total). When periodic boundary conditions are applied, the total electrostatic interaction energy can be computed for all periodic images also. The expression can be modified as

$$V_{el} = \sum_{n} \sum_{(i,j)} \frac{q_i q_j}{|\mathbf{r}_{ij} + nL|}, \tag{2.22}$$

where $nL = \sum_{i=1}^{3} n_i \mathbf{c}_i$, $\mathbf{c}_i$ is lattice vector and n_i is an integer. In terms of the potential

$$V_{el} = \frac{1}{2} \sum_{i=1}^{N} q_i \phi_{[i]}(r_i), \tag{2.23}$$

where $\phi_{[i]}$ is the potential field generated by all ions plus their images, excluding ion i. One cannot use this expression in simulations, since the sum converges poorly. One can overcome this issue by screening the charge with a cloud of opposite charge. The charge density corresponding to a system of N point charges q_i at position r_i can be represented as

$$\rho(r) = \sum_{i=1}^{N} q_i \delta(r - r_i). \tag{2.24}$$

Introducing screening,

$$\begin{aligned}
\rho(r) &= \rho(r) + \rho_{gauss} - \rho_{gauss}, & (2.25)\\
&= [\rho(r) - \rho_{gauss}] + \rho_{gauss}, & (2.26)\\
&= \rho_S + \rho_L, & (2.27)
\end{aligned}$$

where ρ_{gauss} is the screening charge which can be described by a Gaussian distribution. In this case, the fraction of unscreened charge q_i goes to zero at a large distance. The screening charge density can take a Gaussian distribution as

$$\rho_{gauss}(r_i) = q_i(\alpha/\pi)^{3/2} \exp(-\alpha r^2), \tag{2.28}$$

where α determines the width of the Gaussian distribution, $\rho_S = \rho(r) - \rho_{gauss}$ is the screened charge distribution for which the electric potential is short range and the potential corresponding to $\rho_L = \rho_{gauss}$ is long-range. The pictorial representation of charge splitting is

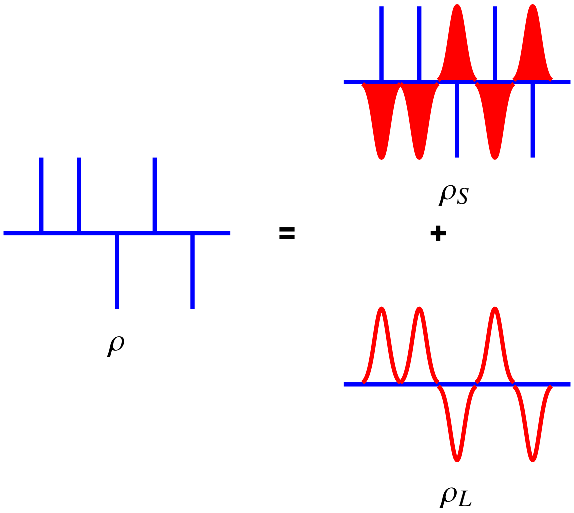

Figure 2.4: Ewald summation: The point charges can be considered as sum of point charges, screening charges and cancelling charge distribution.

shown in Fig. 2.4. The potential field generated by this charge distribution is the solution of the Poisson equation

$$\nabla^2 \phi_i(r) = -\frac{\rho_i(r)}{\epsilon}. \tag{2.29}$$

The potential can also be split into short-range and long-range parts [124]. The short-range part can be computed in real space and is given by

$$\phi^S_{[i]}(r) = \frac{q_i}{r} erfc(\sqrt{\alpha r}), \tag{2.30}$$

where $erfc(x) = 1 - erf(x)$ is the complementary error function and the error function is $erf(r) \sim \frac{2}{\sqrt{\pi}} \int_0^r e^{-t^2} dt.$

The long-range part can be calculated by solving Eqn. (2.29) in Fourier space and the solution is

$$\phi^L_{[i]}(r) = \frac{1}{2V} \sum_{k \neq 0} \frac{4\pi}{k^2} |\rho(k)|^2 \exp(-k^2/4\alpha) - (\alpha/\pi)^{(1/2)} \sum_{i=1}^{N} q_i^2. \tag{2.31}$$

The detailed derivation can be found in reference [124]. The computational complexity needed of the calculation of the Ewald sum is of the order of $O(N^{3/2})$.

2.6.2 Particle-Particle/ Particle-Mesh Algorithm(PPPM)

In PPPM, charges are assigned to the grid points and then the potential is evaluated by using a technique called Fast Fourier Transform (FFT). This method is faster than the Ewald method, with a computational complexity of the order of $O(N \log N)$. The different steps in the algorithm are

1. Charge assignment : assigning charges present in the system to grid points. This is done with the help of a charge assignment function.

2. Evaluation of potential : potential evaluated by solving the Poisson equation using FFT technique.

3. Calculation of electrostatic field : electrostatic field at each grid point is calculated from the negative gradient of the potential.

4. Calculation of force : the force on each particle due to the electric field at each grid point is calculated.

2.7 Choice of ensemble

MD simulations are usually performed in microcanonical or constant NVE, canonical or constant NVT, isothermal-isobaric or constant NPT and grandcanonical ensemble or constant μVT, where N is the number of particles, V is the volume, E is the internal energy, T is the temperature, P is the pressure and μ is the chemical potential. The suitable ensemble is chosen depending on the nature of the thermodynamic quantities to be evaluated and also on the experimental conditions for ease of calculation of quantities of interest. All the ensembles are equivalent in the thermodynamic limit of a system with short-range interactions. In contrast, for a system with long-range interactions, different ensembles are inequivalent [125–127]. The main reason for this inequivalence is the non-additivity of total energy and the non-concavity of the microcanonical entropy.

The different ensembles may not be equivalent for a PE system, since the electrostatic interactions are non-additive long-range interactions. However, most of the theoretical and computational studies on PEs have been done in the canonical ensemble. In MD simulations, simply integrating Newton's equations of motion generates a microcanonical ensemble as a consequence of the conservation of total energy. Several methods have been introduced to keep the temperature constant (canonical ensemble) while using the microcanonical ensemble. A brief introduction to such methods is given below:

1. **Andersen thermostat:** The constant temperature method was proposed by Andersen [128] and is achieved by coupling the system to a heat bath. This is imple-

mented by adding stochastic collisions in the system. In this scheme, randomly selected particles are allowed to collide occasionally and change their velocity, this changed velocity is selected from a Maxwell-Boltzmann distribution corresponding to the desired temperature. All other particles are unaffected by this collision and the main drawback of this method is the randomly updating of velocities of the particles which are involved in the collision. The dynamics of this method is not physical and hence one cannot use this method for the evaluation of dynamical properties.

2. **Berendsen Thermostat:** Another method of keeping the temperature constant was introduced by Berendsen [129]. In this method the velocities of particles are rescaled so as to obtain the desired temperature. The temperature of the system is corrected such that the deviation exponentially decays with a constant time τ,

   $$\frac{dT}{dt} = \frac{T - T_0}{\tau}. \tag{2.32}$$

   Though this method fails to produce fluctuations in energy and hence does not give the canonical ensemble, the method is widely used in equilibration process due to the efficiency with which it relaxes a system to the target temperature.

3. **Langevin Thermostat:** Langevin thermostat uses stochastic disturbances to control the temperature. The particle is assumed to be moving through a sea of small particles. The smaller particles create a damping force on the large particle, $-\gamma_i p_i$, where γ_i is the friction coefficient and p_i is the momentum of i^{th} particle. Also the smaller particle moves with a kinetic energy and gives random kicks to the larger particle. In other words, the idea is to apply a frictional force and random force to the momenta

   $$\dot{p}_i = F_i - \gamma_i p_i + R_i(t), \tag{2.33}$$

   where F_i is the force acting on atom i due to interaction potential, γ_i is the damping factor (friction coefficient) and $R_i(t)$ is the zero-averaged random force having the property

$$< R_i(0)R_i(t) >= 2m_i\gamma_i k_B T\delta(t), \tag{2.34}$$

where T is the desired temperature and $\delta(t)$ the time-step used in MD to integrate the equations of motion.

4. **Nosé-Hoover Thermostat:** Nosé-Hoover thermostat is a commonly used method to achieve constant temperature and this deterministic method was first introduced by Noṡe and further modified by Hoover [130, 131]. This method uses an extended Lagrangian, which has additional artificial position and momentum co-ordinates. These co-ordinates give the effect of a heat bath. There are no random forces or velocities used in this method. The dynamical equations for this method are

$$\dot{r}_i = \frac{p_i}{m}, \tag{2.35}$$

$$\dot{p}_i = f_i - \zeta p_i, \tag{2.36}$$

$$\dot{\zeta} = \frac{\sum_{i\alpha} p_{i\alpha}^2/m - gk_BT}{Q} = \mathcal{V}_T\left(\frac{\mathcal{T}}{T} - 1\right), \tag{2.37}$$

where ζ is the friction coefficient, Q is the thermal inertia parameter, $\mathcal{V}_T$ is the relaxation rate for thermal fluctuations, $g \sim 3N$ is the number of degrees of freedom and $\mathcal{T}$ is the instantaneous ‘mechanical’ temperature. If the system is too hot, i.e. $\mathcal{T} > T$, then the friction coefficient (ζ) increases. When ζ becomes positive the system begins to cool down. If the system is too cold, the reverse happens, and the friction coefficient may become negative, thus heat the system up again. This way, the Nosé Hoover thermostat maintains a constant temperature. The main advantage of this method is that the dynamics of all degrees of freedom are deterministic and time-reversible, and no random variables are used. The equations of motion obeyed by these additional degrees of freedom guarantee that the original degrees of freedom (r^N, p^N) sample a canonical ensemble.

Chapter 3

Mechanism of collapse of single flexible polyelectrolyte

We test the predictions of the different theories describing the collapse transition of a flexible PE using large scale MD simulations. To explain the observed behavior in the collapsed regime, we modify the counterion fluctuation theory by explicitly considering the interactions between monomer-monomer, monomer-counterion and counterion-counterion. A detailed comparison between the theoretical predictions and the results of the simulations are presented. This chapter is based on work presented in Refs. [132] and [133].

3.1 Coil-globule transition of a neutral polymer

The transition of a flexible polymer chain from an extended to a collapsed state is known as coil-globule transition. The neutral polymer undergoes a coil-globule transition upon a change of temperature, pH of the solution, or addition of other polymer molecules [134, 135]. In general, the polymer is in an extended state under good solvent conditions, whereas it is in a collapsed state in a poor solvent. The coil-globule transition has direct implications for many biological systems, such as proteins [136–138].

In computer simulations, the extended or collapsed state of a polymer can be achieved in different ways, for example, by changing the temperature or by adjusting the interaction parameters in the system. Snapshots of a neutral polymer simulated under different values of the interaction parameter, ε_{LJ} are shown in Fig. 3.1, where ε_{LJ} is the parameter of the LJ interaction between the monomers as defined in Sec. 2.3 and $r_c = 2.5$. As ε_{LJ} increases, the quality of the solvent changes from good to poor and the polymer undergoes a transition from an extended to a collapsed state.

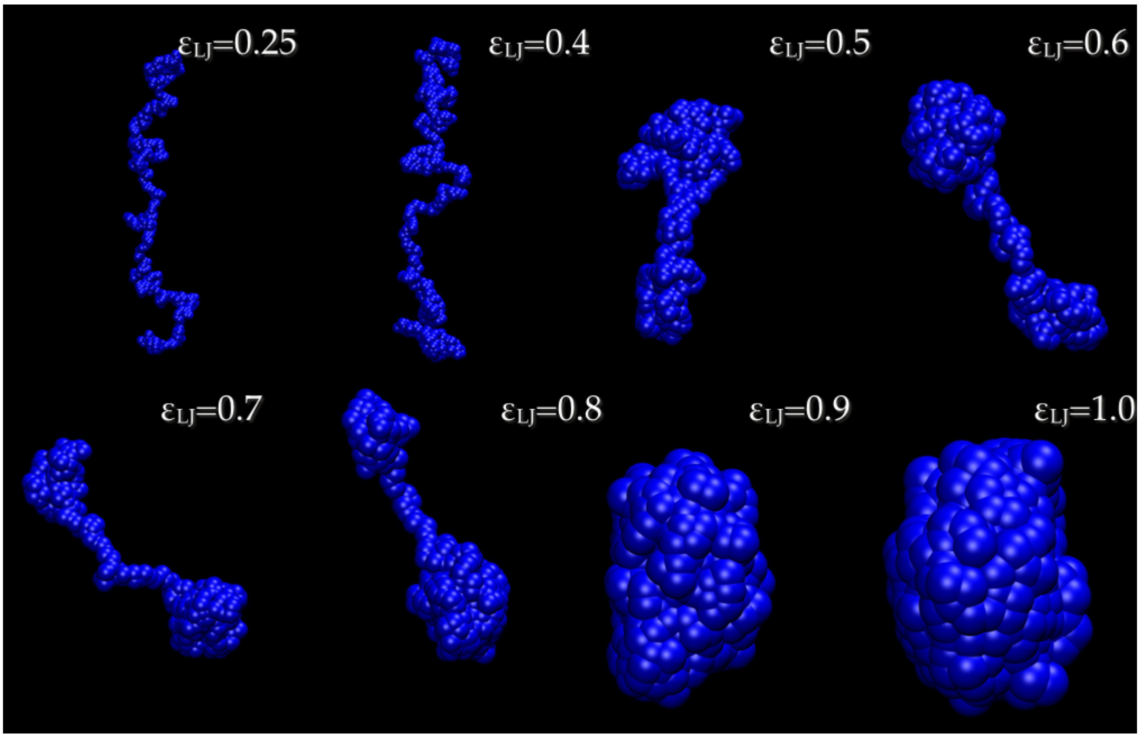

Figure 3.1: Snapshots of a neutral polymer simulated under different values of the parameter, ε_{LJ} associated with the LJ interaction between the monomers. We set $r_c = 2.5$. The values $\varepsilon_{LJ} = 0.9$ and 1.0 are correspond to a poor solvent whereas $\varepsilon_{LJ} = 0.25$ and 0.4 correspond to a good solvent.

3.2 Coil-globule transition of a flexible PE

The behavior of PEs, is more complicated than neutral polymers due to additional electrostatic interactions in the system. The PE undergoes a transition from an extended to a collapsed state irrespective of the solvent quality [10–15, 57, 65–67]. Unlike neutral polymers, the conformations of a PE depend not only on the solvent quality, but crucially depend also on the interplay between the electrostatic energy of the system and the translational entropy of the counterions [15, 57]. The transition occurs at a critical charge density, which depends on the solvent quality. Figure 3.2 shows the snapshot of the single PE system at different charge densities in good and poor solvents where, the top panel of figures corresponds to the PE in a good solvent and the bottom panel corresponds to that in a poor solvent. The strength of the electrostatic interactions depends on the charge density along the PE, which is quantified by the dimensionless Bjerrum length ℓ_B (see Sec. 1.2). For a small charge density, counterions are dispersed away from the PE, and the chain is in an extended conformation when in a good or theta-solvent as in Fig. 3.2 (a) and is collapsed into a compact globule in a bad solvent as in Fig. 3.2 (d) [14, 54]. With increasing charge density, the PE attains an extended conformation, regardless of solvent quality due to the electrostatic repulsion. As we increase the charge density further, counterions begin to condense onto the PE [see Fig. 3.2 (b) and Fig. 3.2 (e)], renormalizing its charge density [46, 54, 139]. This results in an effective attraction between similarly-charged monomers of the PE and it collapses into a globule conformation, independent of the solvent quality as in Fig. 3.2 (c) and Fig. 3.2 (f) [10–15, 57, 65, 66].

The compaction of a PE chain into a globular conformation is of great biological importance. For instance, biological PE molecules like RNA or DNA are densely packed in cells and viruses [68–70] which are orders of magnitude smaller than the contour length of the PE molecule, requiring it to be highly compacted [16, 19].

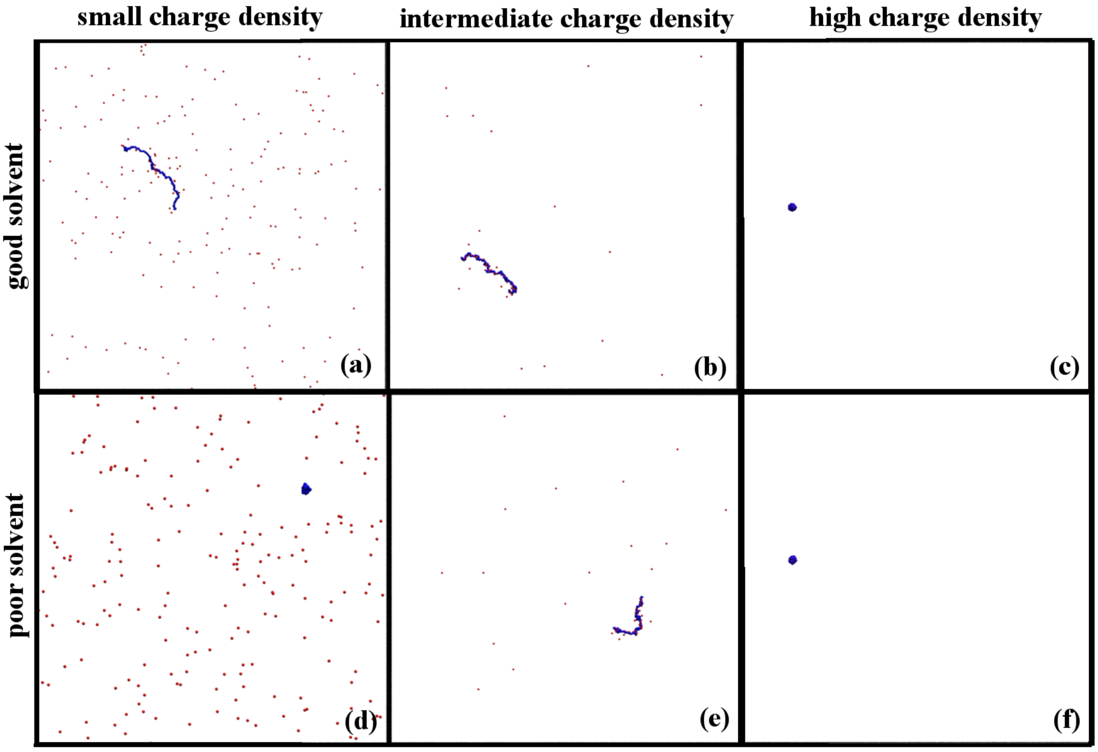

Figure 3.2: Snapshot of a PE simulated under different values of charge density and solvent quality. Snapshot in the upper panel corresponds to good solvent conditions and that in the lower panel corresponds to poor solvent conditions.

3.3 Competing theories on the collapse of a PE

The nature of the effective attractive interactions driving the transition is not well understood and there are competing theories explaining their origin. For the collapsed state, these theories predict that the radius of gyration, R_g, of a PE has the scaling form $R_g \sim N_m^{1/3} \ell_B^{-\gamma}$, where N is the number of monomers of the PE chain, and the exponent γ can potentially depend on system parameters. In the literature, there are three theoretical approaches [15–18, 140–142], based on different physical models, to account for the electrostatics-driven collapse of PEs. All the theories predict a single collapsed regime, but differ in their prediction of the exponent γ characterizing the dependence of R_g on ℓ_B. The different theories are described below.

Dipole theory

In the dipole theory, it is assumed that condensed counterions and the PE monomers form fluctuating dipoles [17, 18, 141, 142]. The dipoles freely rotate, yielding, on average, an attractive interaction between the segments of the chain; this leads to the collapse of a PE even in a good solvent. For a highly charged flexible PE in a salt-free solution, this theory predicts that the radius of gyration of the collapsed conformation scales as $R_g \sim N_m^{1/3}\left|\ell_B^2 - cB\right|^{-1/3}$, where B is the second virial coefficient, N_m is the number of monomers in the PE chain and c is a dimensional constant that depends on the details of the system. This dependence is predicted for both good [17, 18, 142] and bad [17, 142] solvents. For theta-solvent with $B = 0$ [54], a simpler scaling, $R_g \sim \ell_B^{-2/3} {N_m}^{1/3}$ is obtained [17].

Counterion fluctuation theory

In the counterion fluctuation theory [15], the free energy of the collapsed chain is calculated by assuming that the condensed counterions and the monomers are completely uncorrelated. The contribution towards the total free energy has four parts. One is the free energy of the ideal chain, and the rest are the contributions due to the counterion entropy, electrostatic interactions and the volume interactions. The negative part of the free energy comes from the fluctuations in the condensed counterions and leads to a negative pressure in the system that causes the collapse of the PE. The counterion fluctuation theory, when restricted to the second virial coefficient in the volume interactions, predicts that in a good solvent $R_g \sim \ell_B^{-1/2} {N_m}^{1/3}$.

Ionic Solid theory

This theory is based on modeling the collapsed conformation as an amorphous ionic solid [16]. For large charge density of the PE and in the presence of multivalent counterions, the free energy of the solid is smaller than that of the extended PE, driving the chain collapse. In the collapsed conformation, the condensed counterions and the monomers form a dense network, i.e. the condensed counterions do not fluctuate but are localised by forming ionic bonds. This theory, however, does not predict any dependence of the radius of gyration R_g on ℓ_B.

All mechanisms discussed above imply a collapsed phase, $R_g \sim N_m^{1/3}$ for large values of charge density, but different dependence of R_g on ℓ_B. Due to a great significance for applications, especially for nano-medicine and biotechnology, it is vital to have an appropriate theory of the interactions that drive the collapse of a PE.

3.4 MD simulation details

We model a flexible PE chain as described in Sec. 1.2.3, with N_m monomers of charge e connected by harmonic springs of energy

$$U_{bond}(r) = \frac{1}{2}k(r-a)^2, \tag{3.1}$$

where k is the spring constant, a is the equilibrium bond length, and r is the instantaneous distance between the bonded monomers. The PE chain and $N_c = N_m/Z$ neutralizing counterions with a valency Z are placed in a box of linear size L. Pairs of all non-bonded particles (counterions and monomers) separated by a distance r_{ij} interact through the volume (or van der Waals) interactions. Here we model these interactions by the Lennard Jones (LJ) $6-12$ potential with a cut-off of r_c as

$$U_{LJ}(r_{ij}) = 4\varepsilon_{LJ}\left[\left(\sigma/r_{ij}\right)^{12} - \left(\sigma/r_{ij}\right)^{6}\right],\ r_{ij} \leq r_c. \tag{3.2}$$

LJ energy parameter ε_{LJ}	Cutoff distance r_c	Solvent quality
1	1	Good
0.25	2.5	Good
1	2.5	Poor
1.5	2.5	Poor

Table 3.1: The different LJ parameters between monomers used in the implicit solvent simulations and the corresponding solvent quality is listed in table.

The values of ε_{LJ} and r_c are varied to model solvents of different qualities. The electrostatic energy between the charges q_i and q_j separated by a distance r_{ij} is given by

$$U_c(r_{ij}) = \frac{q_i q_j}{\epsilon r_{ij}}, \tag{3.3}$$

where ϵ is the dielectric permittivity.

In the simulations, we use $a = 1.12\sigma$, $k = 500.0 k_B T/\sigma^2$, $L = 370\sigma$, N_m=204 and 402. All energies are measured in units of $k_B T$, and we maintain the temperature at 1 through a Nosé-Hoover thermostat. All distances are measured in terms of σ which we set to 1. The long-range Coulomb interactions are evaluated using particle-particle/particle-mesh (PPPM) technique.

The different LJ parameters between the monomers, used in the implicit solvent simulations and the corresponding solvent quality is listed in table 3.1. For all other volume interactions among counterions and between monomers and counterions, the LJ interactions are repulsive, $\varepsilon_{LJ} = 1.0$ and $r_c = 1.0$. These conditions are chosen in such a way that, when the charge on the monomers is zero (neutral polymer), a PE chain adopts a collapsed conformation or an extended conformation, mimicking poor or good solvent conditions respectively. We also performed additional simulations in which the counterion size (σ_c) is varied. Another set of simulations were performed in the presence of explicit solvent molecules with good solvent conditions. We used the attractive interactions between the monomers and solvent pairs ($r_c = 2.5$, $\varepsilon_{LJ} = 1.0$) and repulsive interactions for all other pairs.

The equations of motion are integrated in time using molecular dynamics simulation package LAMMPS [143] with a time step of 0.001. All the systems are equilibrated for 5×10^6 timesteps and the data presented in this work are averaged over 5×10^6 timesteps of production runs.

3.5 Results

3.5.1 MD simulation studies on the collapse of a PE in a good solvent

In this section, we discuss the results from MD simulations of a single PE in a good solvent with purely repulsive LJ interactions between all non-bonded pairs of monomers and counterions. The cut-off of the LJ interaction is set to be $r_c = 1.0$ and the LJ energy parameter is $\varepsilon_{LJ} = 1$. We simulate the system for various values of $\ell_B > \ell_B^c$ such that the equilibrium configuration of a PE is a collapsed state with $R_g \sim N_m^{1/3}$, where ℓ_B^c is the critical charge density corresponding to the extended to collapse transition.

Radius of gyration of the collapse

The variation of the radius of gyration R_g with ℓ_B in the collapsed regime is shown in Fig. 3.3. It is clear that the R_g decreases as a power law and separates two regimes. The two power laws intersect at $R_g/aN_m^{1/3} \approx 0.63$, 0.66 and 0.69 with the corresponding crossover values $\ell_B^*(Z) \approx 3.71$, 5.58 and 13.70 for valency $Z = 3$, 2 and 1 respectively. It can be seen that for $\ell_B < \ell_B^*(Z)$ the observed dependence, $R_g \propto \ell_B^{-1/2} N_m^{1/3}$, is consistent with the predictions of the counterion fluctuation theory [15]. However, for $\ell_B > \ell_B^*(Z)$, we find a crossover to a different scaling, $R_g \propto \ell_B^{-1/5} N_m^{1/3}$, which is not predicted by any of the existing theories. These two regimes of $\ell_B < \ell_B^*(Z)$ and $\ell_B > \ell_B^*(Z)$ will be referred to as weak and strong electrostatic regimes respectively. We verified that the exponents and

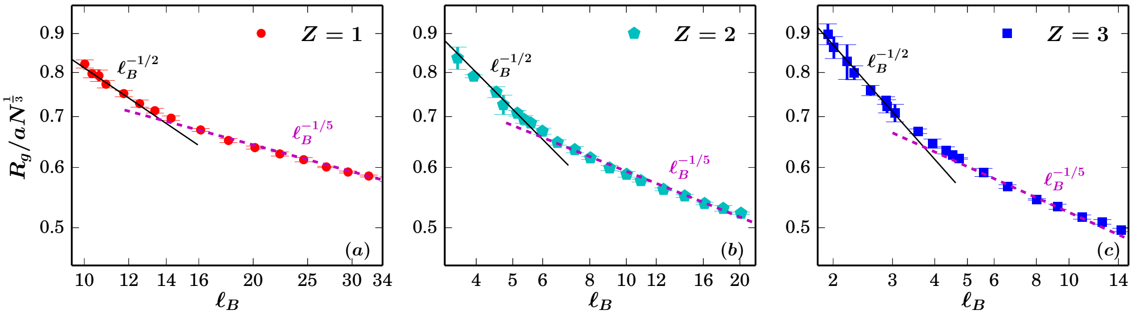

Figure 3.3: Variation of the radius of gyration R_g of a PE chain with the reduced Bjerrum length ℓ_B for different valencies of counterions. The chain length is $N_m = 204$ and interactions in the system are $\varepsilon_{LJ} = 1.0$ and $r_c = 1.0$ between all pairs of particle. The two power laws intersect at $R_g/aN_m^{1/3} \approx 0.63\,(Z = 3)$, $0.66\ (Z = 2)$ and $0.69\ (Z = 1)$ with the corresponding crossover values $\ell_B^*(Z) \approx 3.71\ \ (Z = 3)$, $5.58\ (Z = 2)$, and $13.70\ (Z = 1)$.

associated features seen in Fig. 3.3 are robust and independent of the details of the solvent model by simulating two other systems good solvent conditions. For the first system, we use LJ potential with attractive interaction ($r_c = 2.5$, $\varepsilon_{LJ} = 0.25$) between monomer pairs and purely repulsive interaction ($r_c = 1.0$, $\varepsilon_{LJ} = 1.0$) for all other pairs. From Fig. 3.1, it is evident that the above conditions on the LJ potential correspond to good solvent conditions since the neutral polymer with same parameters is in an extended state. The variation of the radius of gyration R_g with ℓ_B in the collapsed regime of the above system is shown in Fig. 3.4 (a-c). This agrees with the observed scaling in Fig. 3.3. For the second system, we perform the simulation of the PE chain in the presence of explicit solvent molecules. In this system, we use attractive interaction between monomer and solvent pairs ($r_c = 2.5$, $\varepsilon_{LJ} = 1.0$) and purely repulsive interaction ($r_c = 1.0$, $\varepsilon_{LJ} = 1.0$) for all other pairs. It can be seen from Fig. 3.4 (d) that the observed scaling regimes and power laws in Fig. 3.3 are independent of the system with the solvent particle present explicitly. In order to understand whether the results are independent of the chain length N, we perform simulations with $N_m = 204$ and 402. From Fig. 3.4 (e), it is clear that the results are independent of the length of the chain N_m as well.

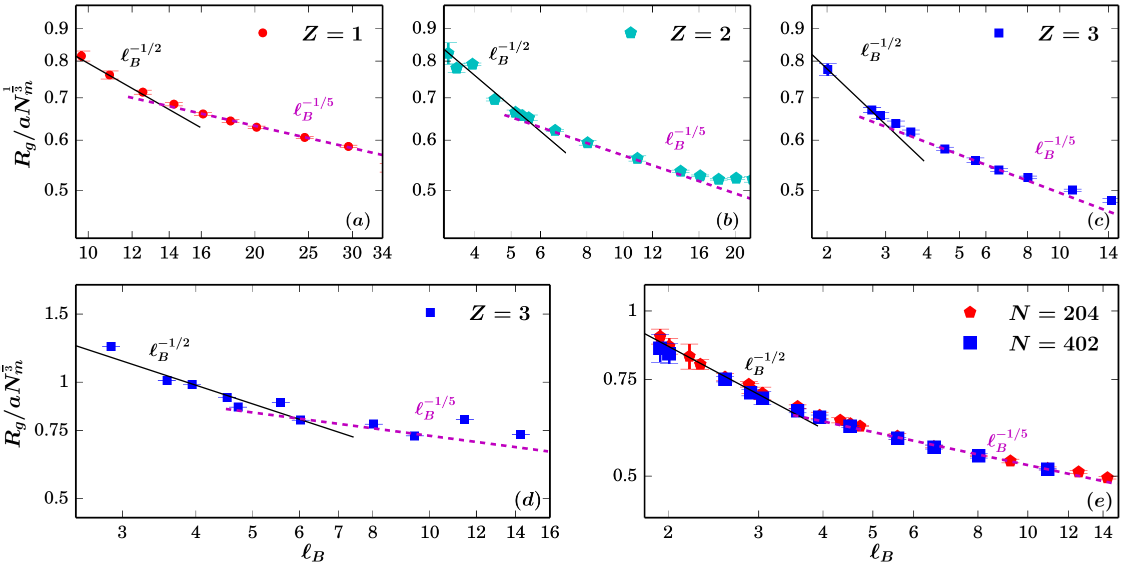

Figure 3.4: The variation of the radius of gyration R_g with respect to charge density ℓ_B for different models of good solvent systems, (a)-(c) implicit solvent with $\varepsilon_{LJ} = 0.25$ and $r_c = 2.5$ (d) explicit solvent and $Z = 3$ and (e) implicit solvent with $\varepsilon_{LJ} = 1.0$ and $r_c = 1.0$ with different N and $Z = 3$.

The two scaling regimes

As we already discussed, in our analysis there are two scaling regimes present in our system depending upon the charge density (see Fig. 3.3), we call them the weak and the strong regimes. In this section, we try to differentiate these regimes structurally with the intuition that, in the weak regime the counterions and the monomers are loosely bound, whereas in the strong regime, they are tightly bound. These can be studied by looking at the counterion distribution and the radial distribution function.

Counterion distribution inside the collapse

Typical snapshots of the system with monovalent counterions in the weak and strong electrostatic regimes are shown in Fig. 3.5 (a-b), which demonstrate that the PE is much more compact in the strong electrostatic regime. This can be further quantified by the radial number density profile ρ as function of r/r' is shown in Fig. 3.5 (c). Here r is the distance of the counterion from the center of mass of the chain, r' is the distance at which the density is 50% of the density at $r = 0$ and $\rho' = N/V'$, where $V' = \frac{4}{3}\pi r'^3$. It can be

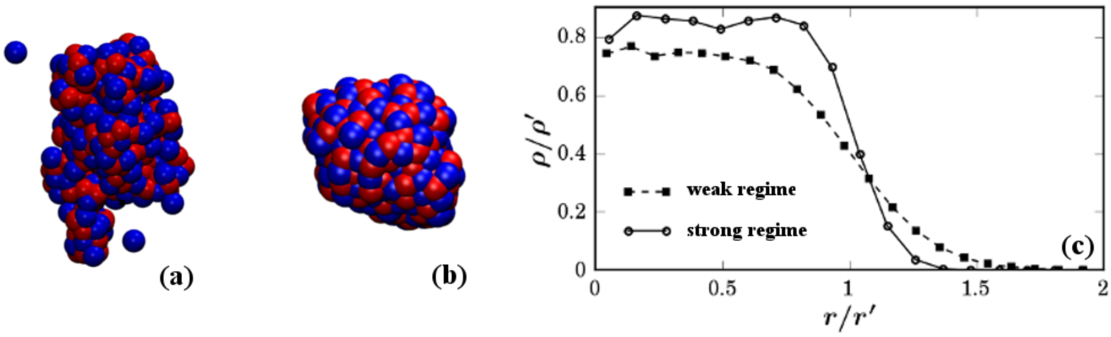

Figure 3.5: Snapshots of collapsed PE in (a) weak electrostatic regime, $Z = 1$, $\ell_B = 10.93$ (left) and (b) strong electrostatic regime, $Z = 1$, $\ell_B = 34.86$ (right). (c) The corresponding radial number density profile ρ of the counterions where r is the distance of the counterion from the center of mass of the chain. r' is the distance at which the density is 50% of the density at $r = 0$ and $\rho' = N/V'$, where $V' = \frac{4}{3}\pi r'^3$.

seen that the profile has a broader tail in the weak electrostatic regime, suggesting that the counterions are more loosely bound compared to that in the strong electrostatic regime.

Radial distribution function of the monomers and the counterions inside the collapse

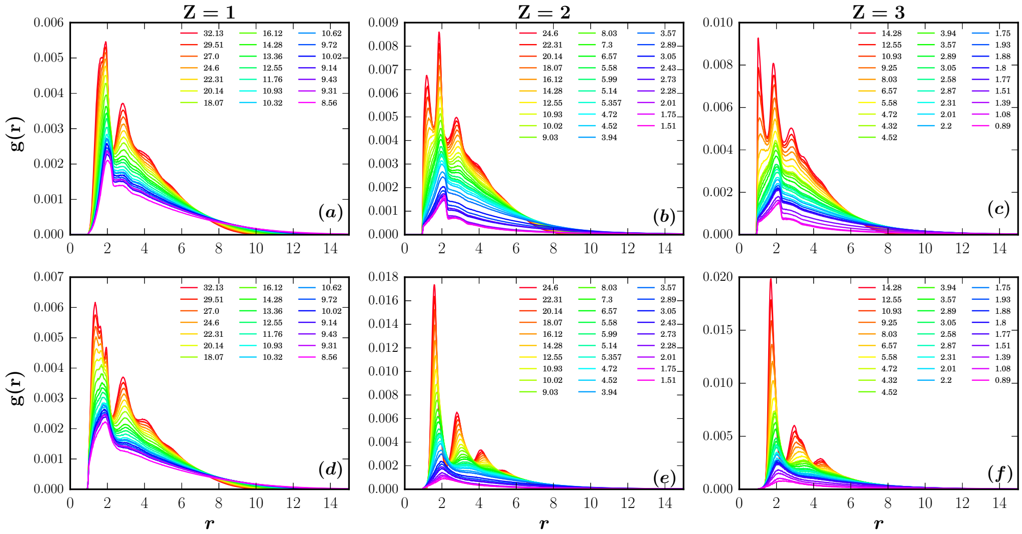

Figure 3.6: Radial distribution function ($g(r)$) between monomers (a-c) and counterions (d-f) at different values of charge density (ℓ_B) and valency (Z).

The radial distribution function, $g(r)$, gives information regarding the structural arrangement of the particle with respect to the reference particle. The height of the peaks of $g(r)$ gives the information regarding how tightly the particles are arranged in the system. For example, an increase in the peak height implies a more tightly packed structure [144].

Fig. 3.6 (a-c) shows an analysis of $g(r)$ between non-bonded monomers of the PE for different values of charge density ℓ_B and Fig. 3.6 (d-f) shows that between counterions. It can be seen from all the plots that the height of the first peak increases as the charge density increases. We can conclude that, both the monomers and the counterions in the weak electrostatic regime are loosely packed, compared to that in the strong electrostatic regime.

3.5.2 Generalized counterion fluctuation theory

The aim of this section is to develop a generalized theory for the electrostatic-driven collapse of a PE in a good as well as a poor solvent. We start with the counterion fluctuation theory for a good solvent and retain the electrostatic term in the original theory [15]. We modify the theory by changing the volume interactions and show that the generalized counterion fluctuation theory is applicable to both good and poor solvent conditions.

Free energy of a PE system

Our main objective is to get a relation between R_g and ℓ_B. Hence we write the free energy in terms of R_g and ℓ_B and minimize it with respect to R_g to obtain the dependence of R_g on ℓ_B. If we take into account the contributions from various entropic and energetic terms, then the expression for the free energy of the system can be written as

$$F(R_g) = F_{\mathrm{id.ch}}(R_g) + F_{\mathrm{en}}(R_g) + F_{\mathrm{el}}(R_g) + F_{\mathrm{vol}}(R_g), \tag{3.4}$$

where $F_{\mathrm{id.ch}}$, F_{en}, F_{el}, and F_{vol} account for the free energy of an ideal chain, entropy of the counterions, the electrostatic interactions between all the charged particles, and the volume interactions between all the particles respectively.

$F_{\mathrm{id.ch}}(R_g)$, the part of the free energy corresponding to the ideal chain is described by

Eqn. (3.5) [15, 54, 145] (For more details see Sec. 1.2.3).

$$\beta F_{\mathrm{id.ch}} \simeq \frac{9}{4}\left(\alpha^2 + \alpha^{-2}\right), \tag{3.5}$$

where $\alpha = R_g/R_{\mathrm{g.id}}$ is the expansion factor, with $R_{\mathrm{g.id}}$ being the radius of gyration of the ideal chain, $R^2_{\mathrm{g.id}} = N_m a^2/6$, where a is the inter-monomer distance.

The second part of the system free energy, $F_{\mathrm{en}}(R_g)$, accounting for the entropy of the counterions and the third part of the system free energy, $F_{\mathrm{el}}(R_g)$ accounting for the electrostatic interactions among all charges are given by the counterion fluctuation theory [15]. In the counterion fluctuation theory, a simplified approximation of two constant counterion densities, one for the condensed counterions inside the gyration volume, $r < R_g$ (r is the distance from the PE center of mass and R_g is the radius of gyration), and the other one for free counterions, $r > R_g$, have been used. That is, the following model for the reduced counterion density $\tilde{\rho}_c(r) = \rho_c(r)/(n/Z)$ has been exploited:

$$\tilde{\rho}_c(r) = \tilde{\rho}\theta(R_g - r) + (1 - \tilde{\rho})\theta(r - R_g)\eta^3, \tag{3.6}$$

where $\tilde{\rho}$ is a constant, $n = N_m/V_g$ ($V_g = 4\pi R_g^3/3$) is the concentration of monomers inside the globule, assumed to be constant, n/Z is the maximal concentration of counterions within the globule, $\theta(x)$ is the unit step-function and $\eta = R_g/R_0 \ll 1$, with R_0 being the radius of the "Wigner-Seitz" cell, which quantifies the volume per one PE chain [146]. The value of R_0 corresponds to the size of the simulation box L in our MD simulations.

Using the above counterion density one can compute the entropic part of the counterion free energy [15] can be written as

$$
\begin{aligned}
\frac{\beta F_{\mathrm{en}}}{N_m} &= \frac{4\pi}{N_m}\int_0^{R_0} dr r^2 \rho_c(r)\Big(\ln[\Lambda_c^3\rho_c(r)]-1\Big) && (3.7)\\
&= 3\int_0^{R_0/R_g} dx x^2 \tilde{\rho}_c(x)\left(\ln[\tilde{\rho}_c(x)]-1\right) && \\
&\simeq -\frac{3}{Z}(1-\tilde{\rho})\ln\left(\frac{R_0}{a}\right), && (3.8)
\end{aligned}
$$

where Λ_c is the thermal wavelength of counterions, $\tilde{\rho} = \rho_{\mathrm{c.in}}/\rho_g$ with $\rho_{\mathrm{c.in}}$ being the number density of counterions within the globule of gyration volume $V_{\mathrm{g}} = 4\pi R_g^3/3$ and $\rho_g = N_c/V_{\mathrm{g}} = N_m/(ZV_{\mathrm{g}})$ is the maximal counterion number density corresponding to complete condensation.

The third part of the system free energy, $F_{\mathrm{el}}(R_g)$, accounting for the electrostatic interactions among all charges is given by the counterion fluctuation theory [15] as

$$
\frac{\beta F_{\mathrm{el}}}{N_m} = \frac{3\sqrt{6}\ell_B N_m^{1/2}(1-\tilde{\rho})^2}{5\alpha}\left(1-\frac{3R_g}{2R_0}\right)-\frac{3}{2}\left(\frac{2}{\pi^2}\right)^{1/3}\frac{\ell_B\sqrt{6}Z^{2/3}\tilde{\rho}^{4/3}}{N_m^{1/6}\alpha}. \tag{3.9}
$$

The first term on the right hand side of Eqn. (3.9) gives the mean-field result for the electrostatic interactions in the system. The second term describes the contribution to the free energy from the correlated fluctuations of the charge density and is beyond the Poisson-Boltzmann approximation [15]. Both Eqns. (3.8) and (3.9) are valid for dilute salt-free PE solutions, $R_0 \gg R_g$ and long chains, $N_m \gg 1$ [15]. In this limit, the terms proportional to R_g/R_0 are negligibly small. Also, it has been assumed that the densities of free and condensed counterions are constants [15] in obtaining Eqns. (3.8) and (3.9). Within this approach one can analyze all conformational regimes of a PE chain, from an extended to a collapsed one, and predict that the electrostatic collapse takes place, for $N_m \to \infty$, as a first-order phase transition [15].

Finally, the free energy accounting for the volume interactions, $F_{\mathrm{vol}}(R_g)$, may be written as

$$F_{\mathrm{vol}}(R_g) = F_{\mathrm{vol\,m.m.}} + F_{\mathrm{vol\,c.m.}} + F_{\mathrm{vol\,c.c.}}, \tag{3.10}$$

where $F_{\mathrm{vol\,m.m.}}$ is the free energy for the volume interactions among monomers, $F_{\mathrm{vol\,c.m.}}$ is the free energy for the volume interactions among counterions and monomers, and $F_{\mathrm{vol\,c.c.}}$ is the free energy terms for the volume interactions among counterions.

The free energy for the volume interactions among monomers may be written in the form of a virial expansion as

$$\begin{aligned}\beta F_{\mathrm{vol\,m.m.}} &= \sum_{k=2}^{\infty} B_k \rho_m^k V_{\mathrm{g}} = \sum_{k=2}^{\infty} B_k \left(\frac{N_m}{V_{\mathrm{g}}}\right)^k V_{\mathrm{g}} \\ &= \sum_{k=2}^{\infty} \left(\frac{4\pi a^3}{3\sqrt{6}}\right)^{1-k} \frac{N_m^{(3-k)/2}}{\alpha^{3(k-1)}} B_k, \end{aligned} \tag{3.11}$$

where B_k is the k-th virial coefficient for monomer-monomer interactions and $\rho_m = N_m/V_{\mathrm{g}}$ is the average density of monomers inside the gyration volume. Similar to Eqn. (3.11), the free energy of the volume interactions of counterions is given as

$$\begin{aligned}\beta F_{\mathrm{vol\,c.c.}} &= \sum_{k=2}^{\infty} C_k \rho_{\mathrm{c.in}}^k V_{\mathrm{g}} = \sum_{k=2}^{\infty} C_k \left(\frac{N_c}{V_{\mathrm{g}}}\right)^k V_{\mathrm{g}} \\ &= \sum_{k=2}^{\infty} \left(\frac{4\pi a^3}{3\sqrt{6}}\right)^{1-k} \frac{C_k}{Z^k} \frac{N_m^{(3-k)/2}}{\alpha^{3(k-1)}}, \end{aligned} \tag{3.12}$$

where $\rho_{\mathrm{c.in}} \simeq N_c/V_{\mathrm{g}} = N_m/ZV_{\mathrm{g}}$ is the average counterion density inside the gyration volume. We approximate it by the corresponding density, when all counterions are condensed. C_k are the virial coefficients for the counterion-counterion interactions. In the above equation, we neglect the term that accounts for the volume interactions of the free counterion $F^{\mathrm{f.c.}}_{\mathrm{vol\,c.c.}}$, since it is negligibly small as compared to $F_{\mathrm{vol\,c.c.}}$:

$$\beta F^{\mathrm{f.c.}}_{\mathrm{vol\,c.c.}} = \sum_{k=2}^{\infty} C_k \left(\frac{N_c(1-\tilde{\rho})}{V_{\mathrm{g}}}\right)^k V_{\mathrm{g}} \left(\frac{R_g}{R_0}\right)^{3(k-1)} \ll \beta F_{\mathrm{vol\,c.c.}}. \tag{3.13}$$

Furthermore, the monomer-counterion volume interactions are described by the term

$$\begin{aligned}\beta F_{\text{vol c.m.}} &= \sum_{k=2}^{\infty}\sum_{l=0}^{k} C_l^k \rho_{\text{c.in}}^l \rho_m^{k-l} D_{l,k-l} V_{\text{g}} \\ &= \sum_{k=2}^{\infty}\left(\frac{4\pi a^3}{3\sqrt{6}}\right)^{1-k}\frac{N_m^{(3-k)/2}}{\alpha^{3(k-1)}}\sum_{l=0}^{k}\frac{C_l^k}{Z^l}D_{l,k-l},\end{aligned} \tag{3.14}$$

where $C_l^k = k!/l!(k-l)!$ are the combinatorial coefficients and $D_{l,k-l}$ is the k-th virial coefficient for monomer-counterion volume interactions which refers to l counterions and $k-l$ monomers.

Using Eqns. (3.11), (3.12) and (3.14) one can write the part of the free energy responsible for the volume interactions in the system in the following compact form:

$$\beta F_{\text{vol}} = \sum_{k=2}^{\infty}\frac{N_m^{(3-k)/2}}{\alpha^{3(k-1)}}\tilde{B}_k, \tag{3.15}$$

where the renormalized virial coefficients $\tilde{B}_k$, that account for all volume interactions, are defined as

$$\tilde{B}_k = \left(\frac{2\pi a^3}{9\sqrt{6}}\right)^{1-k}\left(B_k + \sum_{l=0}^{k}\frac{C_l^k}{Z^l}D_{l,k-l} + \frac{C_k}{Z^k}\right). \tag{3.16}$$

When the packing fraction of monomers is small, the free energy is well-approximated by the truncated virial expansion [54]. The counterion fluctuation theory, uses only the second virial term. In order to explain the additional observed regime in the MD simulation results (see Sec. 3.5.1), keeping all terms up to the third virial term is necessary. Then we obtain for $F_{\text{vol m.m.}}$

$$\begin{aligned}\beta F_{\text{vol m.m.}} &= \left(B_2\rho_m^2 + B_3\rho_m^3\right)V_{\text{g}} = \left(B_2\left(\frac{N_m}{V_{\text{g}}}\right)^2 + B_3\left(\frac{N_m}{V_{\text{g}}}\right)^3\right)V_{\text{g}} \\ &= \tilde{b}^{-1}\frac{B_2}{\alpha^3 N_m^{1/2}} + \tilde{b}^{-2}\frac{B_3}{\alpha^6},\end{aligned} \tag{3.17}$$

where B_2 and B_3 are the second and third virial coefficients for monomer-monomer interactions, $\rho_m = N_m/V_{\text{g}}$ is the average density of monomers inside the gyration volume and $\tilde{b} = \left(2\pi a^3/9\sqrt{6}\right)$. Both B_2 and B_3 are positive in the case of a good solvent. For a poor solvent, in general, we expect B_2 to be negative, making it necessary to keep the third virial term, the first positive term in the virial expansion. The free energy of the volume interactions involving counterions $F_{\mathrm{vol\,c.c.}}$ and $F_{\mathrm{vol\,c.m.}}$ will have a similar form as in Eqn. (3.17). Combining these expressions for $F_{\mathrm{vol\,m.m.}}$, $F_{\mathrm{vol\,c.m.}}$ and $F_{\mathrm{vol\,c.c.}}$ we obtain the free energy F_{vol} for the collapsed PE to be:

$$\beta F_{\mathrm{vol}} = \frac{\tilde{B}_2}{\alpha^3 N_m^{1/2}} + \frac{\tilde{B}_3}{\alpha^6}, \tag{3.18}$$

where $\tilde{B}_2$ and $\tilde{B}_3$ are the renormalized second and third virial coefficients respectively that account for all volume interactions. The general expression of these coefficients is given in Eqn. (3.16) and for the present case is given as

$$\tilde{B}_2 = \tilde{b}^{-1}\left(B_2 + \frac{2D_{1,1}}{Z} + \frac{C_2}{Z^2}\right), \tag{3.19}$$

$$\tilde{B}_3 = \tilde{b}^{-2}\left(B_3 + \frac{3D_{1,2}}{Z} + \frac{3D_{2,1}}{Z^2} + \frac{C_3}{Z^3}\right). \tag{3.20}$$

The value of the bare virial coefficients B_k, C_k and $D_{l,k-l}$ are determined by the relative strength of the LJ interactions and the thermal energy $k_B T$. Due to the dominance of repulsive forces in the monomer-counterion and counterion-counterion volume interactions considered here, all coefficients C_k and $D_{l,k-l}$ are positive, $C_k > 0$ and $D_{l,k-l} > 0$ for $k \geq 2$ and $1 \leq l \leq k$. We also assume that the renormalized third virial coefficient $\tilde{B}_3$ is positive as well.

The sign of the renormalized second virial coefficient $\tilde{B}_2$ is difficult to determine apriori. Though the "bare" value B_2 is negative for poor solvents, the renormalized coefficient $\tilde{B}_2$ also depends on the counterion valency and the virial coefficients C_k and $D_{l,k-l}$ [see Eqn. (3.19)]. If these positive coefficients are large and the valency Z is small, $\tilde{B}_2$ could potentially change sign and become positive. The values of the virial coefficients C_k and $D_{l,k-l}$ are determined by the size of the counterions: the larger the counterions, the larger are the virial coefficients. Hence, it is expected that large counterions will result in a positive renormalized coefficient, $\tilde{B}_2 > 0$. These predictions will be checked in our MD simulations discussed in Sec. 3.5.3. The virial expansion truncated at the third virial term [see Eqn. (3.18)] is valid for a poor solvent for low packing fractions. For a good solvent, it is necessary to include the third virial term to explain the observed scaling of R_g with ℓ_B in the strong electrostatic regime described in Sec. 3.5.1. At the same time, the packing fractions remain relatively low for a wide range of ℓ_B values and the inclusion of only the third virial term is sufficient. However, for a poor solvent, due to the attractive volume interactions, we anticipate that the packing fractions will be larger than that of a good solvent at the same ℓ_B. When the packing fraction is high, the truncated expansion Eqn. (3.17) loses its accuracy. In this case, either all the terms in the virial expansion must be retained or an effective equation of state (EOS) for dense fluids like Flory-Huggins or van der Waals EOS or EOS for Lennard-Jones mixtures (e.g. ref [147]) is to be used. In the EOS approach, one has to use model parameters, specific for a particular system, which may be obtained only by fitting available experimental or numerical data. However, we choose the first approach, developed for dense gases [148], where the virial coefficients are explicitly expressed in terms of the interaction potential. Including additional terms in the virial expansion, we obtain the general form as in Eqn. (3.15) has to be considered.

Combining the different contributions [Eqns. (3.5), (3.8), (3.9) and (3.15)] the free energy in Eqn. (3.4) attains the form

$$\begin{aligned}\frac{\beta F(\alpha)}{N_m} \simeq{}& \frac{9}{4N_m}\left(\alpha^2+\alpha^{-2}\right)-\frac{3}{Z}(1-\tilde{\rho})\ln\left(\frac{R_0}{a}\right)\\ &+\frac{3\sqrt{6}\ell_B N_m^{1/2}(1-\tilde{\rho})^2}{5\alpha}\left(1-\frac{3R_g}{2R_0}\right)-\frac{\tilde{Z}^2\ell_B}{N_m^{1/6}\alpha}+\sum_{k=2}^{\infty}\frac{N_m^{(1-k)/2}}{\alpha^{3(k-1)}}\tilde{B}_k,\end{aligned} \tag{3.21}$$

where $\tilde{Z}^2 = (3/2)(2/\pi^2)^{1/3}\sqrt{6}Z^{2/3}$. In the collapsed regime, it is well known that, regardless of the solvent quality, almost all counterions are located within the gyration volume of the PE chain. Hence, the average counterion density inside the gyration volume will be $\rho_{\text{c.in}} \simeq \rho_g = N_c/V_{\text{g}}$ resulting in $\tilde{\rho} \approx 1$ in Eqns. (3.8) and (3.9). This allows us to ignore the second and third terms on the right hand side of Eqn. (3.21) [1]. These two terms correspond to the entropy of counterions and to the mean-field contribution to the electrostatic energy. Moreover, since $R_g \sim N_m^{1/3}$ in a collapsed regime, the expansion factor $\alpha \sim N_m^{-1/6} \ll 1$. Thus, the term proportional to α^2 in $F_{\text{id.ch}}(\alpha)$ [refer Eqn. (3.5)] can also be neglected. It is straightforward to see that, in this limit, the term proportional to α^{-2} in $F_{\text{id.ch}}(\alpha)$ is small compared to the volume terms and may be dropped as well. With these approximations, Eqn. (3.21) for the free energy of a PE in a collapsed state, in terms of R_g, reduces to the following expression, regardless of the solvent quality:

$$\frac{\beta F(R_g)}{N_m} = -\frac{\tilde{Z}^2 a \ell_B}{\sqrt{6}}\left(\frac{N_m}{R_g^3}\right)^{1/3} + \sum_{k=2}^{\infty} \frac{\tilde{B}_k a^{3k-3}}{6^{(3k-3)/2}}\left(\frac{N_m}{R_g^3}\right)^{k-1}. \tag{3.22}$$

Dependence of R_g and energies of a PE chain on ℓ_B

Our aim is to understand the correct theory through the relation between R_g and ℓ_B. The dependence of R_g on ℓ_B ($R_g \sim \ell_B^{-\gamma}$) may be obtained by minimizing the free energy, Eqn. (3.22), with respect R_g as

$$2\tilde{Z}^2 \ell_B = \left(\frac{N_m a^3}{R_g^3}\right)^{2/3}\left[\tilde{B}_2 + \frac{2\tilde{B}_3}{6^{5/2}}\left(\frac{N_m a^3}{R_g^3}\right) + \frac{3\tilde{B}_4}{6^3}\left(\frac{N_m a^3}{R_g^3}\right)^2 + \ldots,\right] \tag{3.23}$$

The relative importance of different terms in Eqn. (3.23) depends on the packing fraction $N_m a^3/R_g^3$ and the virial coefficients $\tilde{B}_k$. We consider three cases below

1. When the packing fraction is small and the sign of $\tilde{B}_2$ is positive, the right hand side of Eqn. (3.23), which arises from virial expansion, can be truncated at $\tilde{B}_2$, yielding the following dependence of R_g on ℓ_B:

$$R_g = \frac{\sqrt{\tilde{B}_2}\, a N_m^{1/3}}{\sqrt{2}\tilde{Z}\ell_B^{1/2}}, \tag{3.24}$$

---

[1] One can also use a more rigorous approach as in the original counterion fluctuation theory [15] and minimize the total free energy with respect to $\tilde{\rho}$. This will give the value of $\tilde{\rho}$ very close to unity. Moreover, for $N_m \to \infty$ the collapse occurs as a first-order phase transition and $\tilde{\rho} = 1$ exactly in this limit.

which implies $R_g \propto \ell_B^{-1/2}$.

2. When the packing fraction is small and the sign of $\tilde{B}_2$ is negative, the most dominant positive term on the right hand side of Eqn. (3.23) is the term proportional to $\tilde{B}_3$. Truncating the series at $\tilde{B}_3$, we obtain

   $$R_g = \frac{\tilde{B}_3^{1/5} a N_m^{1/3}}{6^{3/10} \tilde{Z}^{2/5} \ell_B^{1/5}}, \tag{3.25}$$

   or $\gamma = 1/5$. Here we also assume that the electrostatic term strongly dominates over the term with the negative virial coefficient $\tilde{B}_2$.

3. When the packing fraction is large, the truncation of virial expansion fails as discussed in Sec. 3.5.2. In this case, all the terms on the right hand side of Eqn. (3.23) have to be retained. Qualitatively, we expect R_g to decrease with ℓ_B with a continuously varying "local " exponent γ. As it follows from the above analysis, the value of γ is determined by the dominating virial coefficient. If for some interval of ℓ_B the k-th virial coefficient is dominating, similar considerations lead to the conclusion, that $R_g \sim \ell_B^{1/(3k-4)}$ for this interval. Since $k > 3$, one finds that $\gamma < 1/5$. With increasing ℓ_B, the number k that refers to the dominating coefficient is expected to increase.

In the case of a good solvent, the packing fraction is small and truncating virial expansion at the third virial coefficient is enough to explain the observed behavior, whereas in the case of a poor solvent, more terms in the virial expansion are needed, depending on the strength of the solvent and the charge density.

We also derive the dependence of the internal energies, associated with the electrostatic and volume interactions, on the radius of gyration R_g. Using the thermodynamic relation for the internal energy $E = \partial \beta F / \partial \beta$, we obtain

$$
\begin{aligned}
\frac{\beta E_{\rm el}}{N_m \ell_B} &= -\frac{\tilde{Z}^2 a N_m^{1/3}}{\sqrt{6} R_g} \sim \frac{N_m^{1/3}}{R_g}, & (3.26)\\
\frac{\beta E_{LJ}}{N_m} &= \frac{\tilde{B}_2' N_m}{R_g^3} + \frac{\tilde{B}_3' N_m^2}{R_g^6} + \frac{\tilde{B}_4' N_m^3}{R_g^9} + \frac{\tilde{B}_5' N_m^4}{R_g^{12}} + \ldots, & (3.27)
\end{aligned}
$$

where $E_{\rm el}$ and E_{LJ} are the electrostatic and the volume components of the internal energy and the constants $\tilde{B}_k'$ may be expressed in terms of the derivatives of the renormalized virial coefficients $\tilde{B}_k$ with respect to the temperature.

Packing fraction of monomers

The packing fraction of monomers ϕ_m may be estimated as follows:

$$
\phi_m = \frac{\pi}{6} \frac{N_m}{V_{\rm act}} d^3, \tag{3.28}
$$

where d is the effective hard-core diameter, which for the soft-sphere potential $v(r)$ may be found from the expression [149]

$$
d = \int_0^\infty \left[1 - e^{-v(r)/k_B T} \right] dr. \tag{3.29}
$$

For the LJ potential with the cutoff at $r_c = 1.0$ and $\varepsilon_{LJ}/k_B T = 1$ we obtain

$$
d = 0.973\,\sigma. \tag{3.30}
$$

Taking into account the relation between the actual volume of the globule and the gyration volume, we obtain for the packing fraction

$$
\phi_m = 0.0535 \, \frac{N_m \sigma^3}{R_g^3}, \tag{3.31}
$$

which gives the packing fraction ϕ_m of about 0.08 for the weak electrostatic collapse and about 0.166 for the strong electrostatic collapse for $Z = 1$, with similar values for other valencies. If one takes into account the volume interaction with the counterions, the effective packing fraction may be twice large, as an upper limit. Still, it may be shown that in the range of studied parameters one has either the dominance in the volume interactions of the term of the second virial coefficient (for the weak collapse) or of the third virial coefficient (for the strong collapse); the term associated with the fourth virial coefficient is always smaller and may be approximated by zero. This guarantees that for the addressed range of parameters, two scaling regimes are observed $R_g \sim \ell_B^{-1/2}$ and $R_g \sim \ell_B^{-1/5}$ for PE in a good solvent.

3.5.3 Corroboration of theory using MD simulation studies

Poor solvent

It is more challenging, however, to study a collapsed state of a flexible PE in a poor solvent [150–156] since, unlike in a good solvent, there exist additional attractive interactions between monomers which compete with the repulsive part of electrostatic interactions. The valency of counterions determines the number of counterions condensed inside the collapsed globule and hence affects the monomer-monomer distance and thereby modifies the attractive volume interactions. Hence, the valency of the counterions which played no role in determining the exponent γ for a good solvent becomes significant for a poor solvent and possibly influences the exponent γ.

We simulate a flexible PE in poor solvents of varying the strengths, to obtain the dependence of R_g on ℓ_B as well as strength of the solvent. Fig. 3.7 shows the variation of R_g for a collapsed PE with ℓ_B for different counterion valency for two poor solvent conditions ($\varepsilon_{LJ} = 1.0,\ 1.5$ and $r_c = 2.5$ for monomer-monomer interaction). When $\varepsilon_{LJ} = 1.0$ [see Fig. 3.7 (a)-(c)] and $\varepsilon_{LJ} = 1.5$ [see Fig. 3.7 (d)-(f)], for monovalent and divalent counteri-

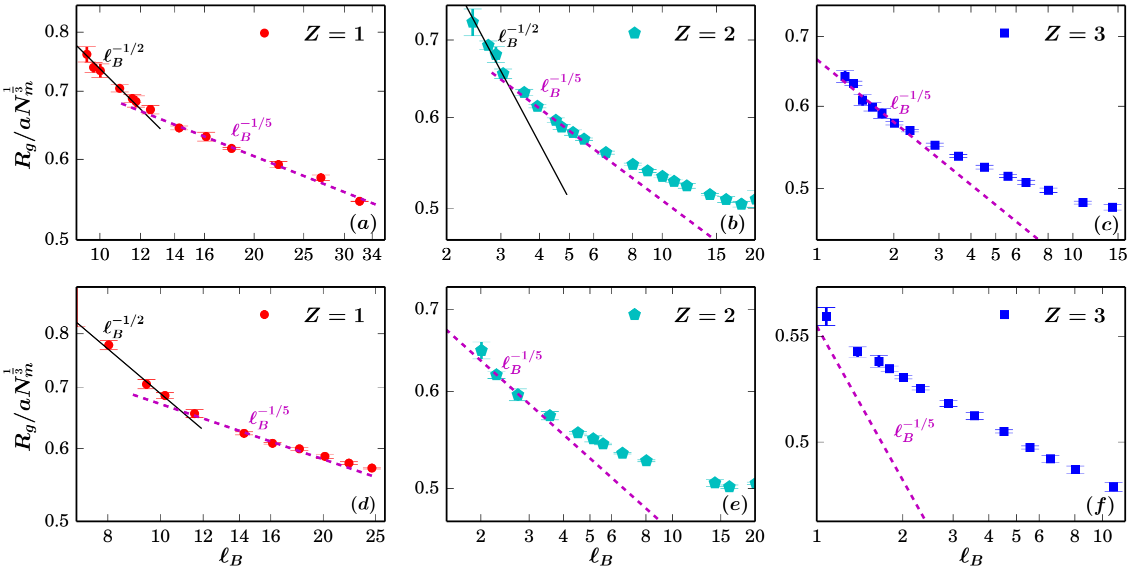

Figure 3.7: Variation of the radius of gyration R_g with ℓ_B for a PE chain with different counterion valency for poor solvent conditions with (a-c) $\varepsilon_{LJ} = 1.0$ and (d-f) $\varepsilon_{LJ} = 1.5$ and $r_c = 2.5$ for monomers. The solid straight lines correspond to the power laws with exponents $\gamma = 1/2$ and the dashed lines correspond to $\gamma = 1/5$ as predicted by the theory.

ons, two dominant sub-regimes characterized by $R_g \sim \ell_B^{-\gamma}$, with $\gamma = 1/2$ and $1/5$ exist. For trivalent counterions, we do not observe the regime with $\gamma = 1/2$ for $\varepsilon_{LJ} = 1.0$ [see Fig. 3.7 (c)], while for the case $\varepsilon_{LJ} = 1.5$ [see Fig. 3.7 (f)] , both regimes with $\gamma = 1/2$ and $1/5$ are absent. Also, in the case of divalent and trivalent counterions, for larger ℓ_B, an additional sub-regime appears where R_g decreases as a convex function of ℓ_B with a continuously decreasing slope (in the log-log plot). Qualitatively, this corresponds to an effective local power-law exponent γ, smaller than $1/5$ as discussed in Sec. 3.5.2. Following the discussion, the regimes with smaller values of γ that are observed in our simulations may potentially correspond to a larger packing fraction of the collapsed PE, where the truncation of virial expansion at the third term fails. The MD data presented in Fig. 3.7 are consistent with the theoretical predictions of Sec. 3.5.2.

Effect of the counterion size on the second virial coefficient

The appearance of $\gamma = 1/2$ in Fig. 3.7, which corresponds to a positive second virial coefficient is surprising, since in poor solvent conditions, the bare second virial coefficient B_2, when restricted to monomer-monomer interactions, is expected to be negative. Indeed when the charge of monomers is zero, the neutral PE always adopts a collapsed state in a poor solvent condition, corresponding to negative value of B_2 [54]. Then from Eqns. (3.23) and (3.25), it can be seen that the largest possible value for the exponent γ should be $1/5$, corresponding to the (positive) third virial term for a poor solvent. Hence, we envisage that the presence of the counterions inside a collapsed globule leads to the change of the sign of B_2 for the range of LJ parameters and valency of counterions considered here. This agrees with the theoretical analysis in Sec. 3.5.2 , where we argued that for large counterions, the effective second virial coefficient, $\tilde{B}_2$, could be positive, although the bare coefficient B_2 is negative, yielding the regime with $\gamma = 1/2$. Physically, the negative sign of $\tilde{B}_2$ follows from the dominance of attractive volume interactions. However, in the case of large counterions with a low valency (which implies a larger counterion density inside a globule), can potentially keep the chain monomers apart and reduce the effect of attractive volume interactions between them; this results in the alteration of the sign of $\tilde{B}_2$ and the regime with $\gamma = 1/2$ can be observed. At the same time, small counterions of high valency (which implies lower density of these inside the globule) cannot effectively keep the monomers apart, so that the effective attractive volume interactions between monomers can yield a negative $\tilde{B}_2$. For these systems the regime with $\gamma = 1/2$ would be absent. In other words, if the regime with $\gamma = 1/2$ is observed for some system ($\tilde{B}_2 > 0$), the decrease of counterion size should entail the alteration of the sign of $\tilde{B}_2$ and hence, the disappearance of this regime, as for $\tilde{B}_2 < 0$. On the other hand, if the regime with $\gamma = 1/2$ is absent ($\tilde{B}_2 < 0$), the increase of the counterion size should lead to the change of the sign of $\tilde{B}_2$ and appearance of the regime with $\gamma = 1/2$, as for $\tilde{B}_2 > 0$. To confirm these predictions regarding the effect of counterion size on second virial coefficient, we perform additional simulations varying the size of counterions, σ_{c-c}: (1) for the case of monovalent counterions we decrease σ_{c-c} and test whether the regime with $\gamma = 1/2$ disappears and (2) for the case of trivalent counterions, we increase σ_{c-c} and check whether the regime with $\gamma = 1/2$ emerges. The MD data for these two simulations are shown in Fig. 3.8. As predicted, in the case of monovalent counterions,

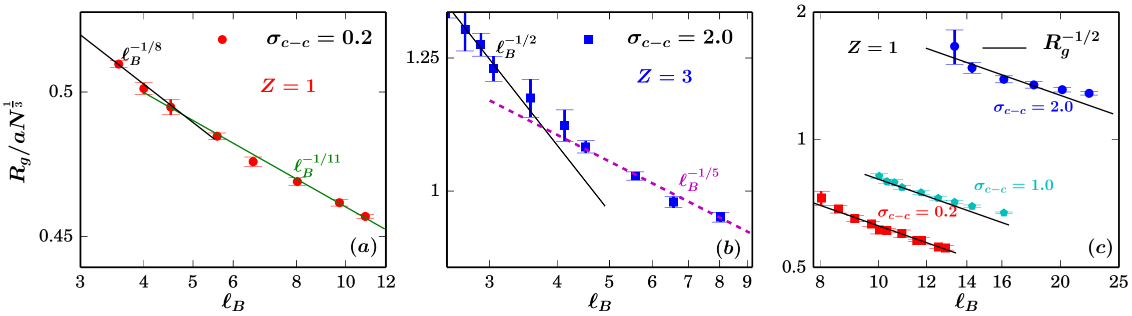

Figure 3.8: (a) Plots showing the disappearance of $R_g \sim \ell_B^{-1/2}$ and $R_g \sim \ell_B^{-1/5}$ regimes for monovalent-counterion system with $\varepsilon_{LJ} = 1$ when the radius of the counterion is reduced [compare with Fig. 3.7 (a)]. (b) The appearance of $R_g \sim \ell_B^{-1/2}$ regime for trivalent-counterion system with $\varepsilon_{LJ} = 1.0$ by increasing the counterion radius [compare with Fig. 3.7 (e)]. (c) The presence of $R_g \sim \ell_B^{-1/2}$ regime for a good solvent ($\varepsilon_{LJ} = 1$ and $r_c = 1$), the valency of counterions $Z = 1$ for different radius of counterions. The chain length is $N_m = 204$.

as the size of the counterions is reduced, we find that the regime with $\gamma = 1/2$ vanishes [see Fig. 3.8 (a)], i.e, $\tilde{B}_2$ becomes negative. On the other hand, in the case of trivalent counterions, the regime with $\gamma = 1/2$, absent for $\sigma_{c-c} = 1$ [see Fig. 3.7 (e)], appears when the counterion size increases up to $\sigma_{c-c} = 2$ [see Fig. 3.8 (b)]. These data confirm that the presence of counterions inside the condensed phase can strongly modulate the effective attractive interactions between the monomers of PE and can change the sign of the second virial coefficient $\tilde{B}_2$.

For a good solvent, with repulsive interactions between the monomers, the counterion size and valency are expected to play no role. In Fig. 3.8 (c), we present the results from MD simulations of a PE in a good solvent for three different counterion sizes (σ_{c-c}) which clearly show the presence of the sub-regime with $\gamma = 1/2$ for all the σ_{c-c}. The results in Fig. 3.8 (c) combined with those in Fig. 3.8 (a-b), show that, while the sign of $\tilde{B}_2$ is unambiguous in a good solvent, the same is not true in the case of a poor solvent and depends on several system parameters such as the strength of the solvent, the valency and the size of the counterions. This suggests that, for charged polymers with attractive monomer-monomer volume interactions and in the presence of counterions, the sign of the second virial coefficient cannot be assumed to be always negative. This is in a striking contrast with collapsed neutral polymers, which have the same attractive monomer-monomer interactions, where the sign of B_2 is always negative.

Electrostatic and LJ energy

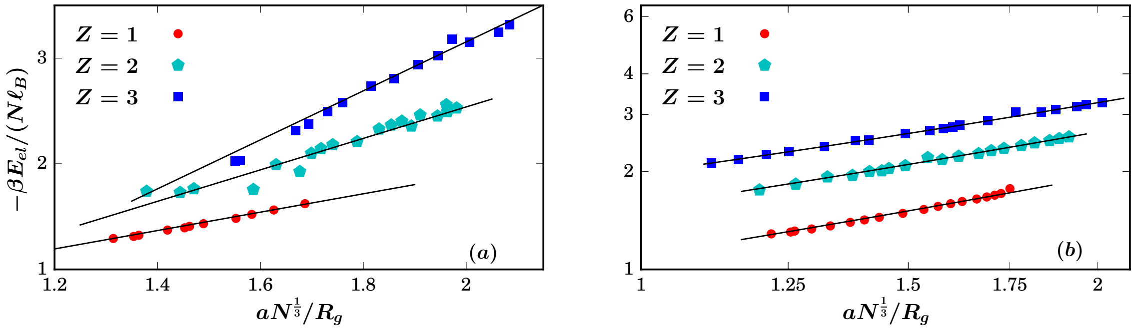

Figure 3.9: The dependence of the electrostatic energy, E_{el} on the radius of gyration R_g for different counterion valencies for (a) poor solvent and (b) good solvent. Solid line corresponds to R_g^{-1}.

The counterion fluctuation theory, as developed in Sec. 3.5.2, may be further confirmed by computing the energies E_{el} and E_{LJ} from MD simulations. As can be seen from Eqn. (3.26), the scaling of E_{el}/ℓ_B is independent of ℓ_B across a wide range of ℓ_B values and the solvent quality and scales as the inverse of R_g. The results for dependence of E_{el} on R_g from our MD simulations, shown in Fig. 3.9, capture the linear dependence of E_{el} on R_g^{-1} for all valencies, irrespective of the solvent quality.

The dependence of E_{LJ} on R_g is more complicated and exhibits a crossover from one regime to another, similar to the dependence of R_g on ℓ_B. The total LJ energy E_{LJ} has contributions from attractive monomer-monomer interactions and repulsive interactions between other pairs. This makes it difficult to analyse E_{LJ} in terms of second and third virial coefficients. Instead, we measure E_{LJ}^{mc}, the monomer-counterion component of the LJ energy as only repulsive interactions contribute to it. E_{LJ}^{mc}, shown in Fig. 3.10 (a), captures the dependence of E_{LJ} on R_g^3 and R_g^6 well, validating the free energy expression, Eqn. (3.22). For E_{LJ}, we also note that, as the valency of the counterions is increased, powers of R_g, corresponding to larger virial terms, appear. A possible physical explanation for this is that, as the electrostatic interactions in the system become stronger and the packing fraction of all the species inside the globule increases, more terms to account for the volume interactions in the collapsed state are needed.

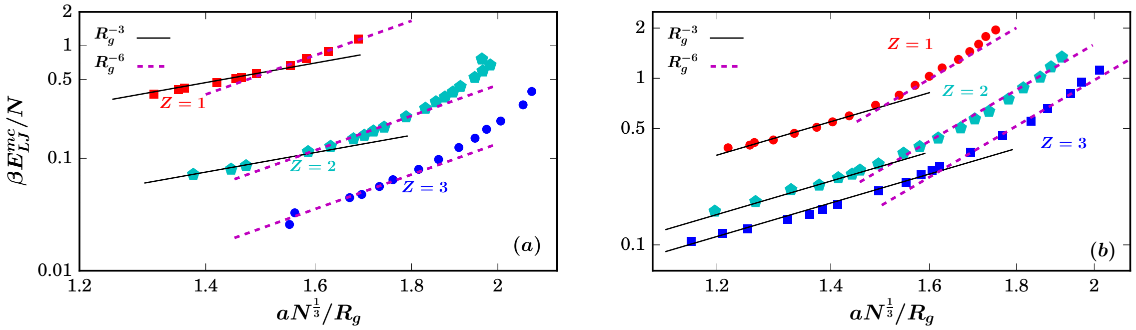

Figure 3.10: The monomer-counterion component of the LJ energy, E_{LJ}^{mc}, on the radius of gyration R_g for different counterion valencies for (a) poor solvent and (b) good solvent.

In the case of a good solvent, we retained the first two terms in the equation. If the first term on the right hand side of Eqn. (3.27) dominates, one obtains $E_{LJ} \sim R_g^{-3}$; if the second one dominates, then $E_{LJ} \sim R_g^{-6}$. In Fig. 3.10 (b), we plot the respective internal energy due to volume interactions from our MD data. The figure convincingly illustrates the dominance of the second and third virial terms in the weak and strong electrostatic regimes correspondingly, with the crossover occurring at $R_g/aN_m^{1/3} \approx 0.63$ ($Z = 3$), 0.64 ($Z = 2$) and 0.68 ($Z = 1$). These values match closely with the crossover found in Fig. 3.3.

3.5.4 Behavior of the collapse at an extremely high charge density

It has also been suggested that at very large charge densities, the PE can collapse into a crystalline-like conformation known as Wigner crystal [157–159], preceded by a glass-like behavior. It would also be interesting to probe these conformations in both good and poor solvents and understand the role of condensed counterions on such quenched structures. The primary questions of interest in such systems is to elucidate whether the counterion-counterion interaction or the counterion-monomer interactions drive these quenched structures when the electrostatic interaction in the system are very high.

Fig. 3.11 shows the snapshots for a flexible PE for very high charge density in good and

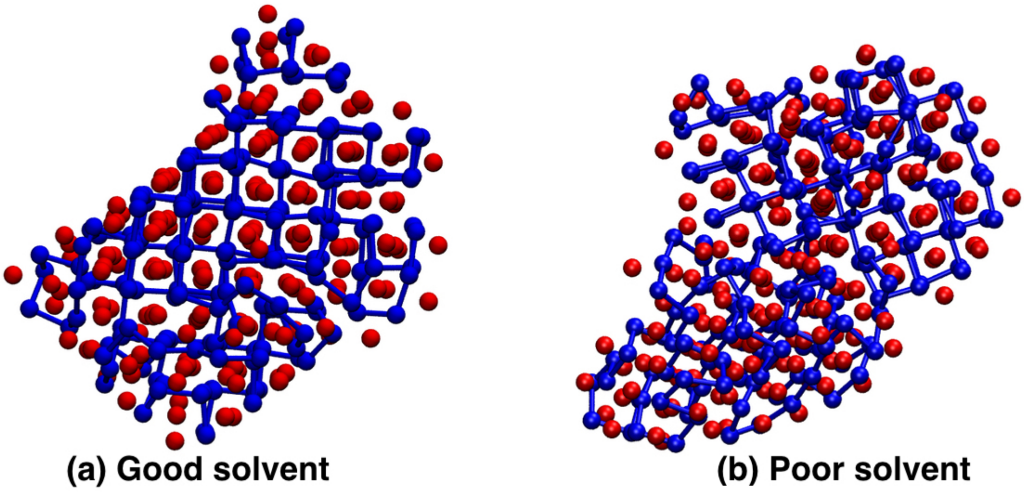

Figure 3.11: Snapshots of collapsed conformation of PE in good and poor solvent condition for the same value of charge density along the PE ($\ell_B = 37.7$).

poor solvent conditions and for monovalent counterions. The data show that though for both solvent qualities, the collapsed conformation of the PE takes on a more crystallized form with respect to both monomers and counterions for high values of charge density, the crystallization is much more significant in the case of a good solvent than a poor solvent. This can be understood in terms of the effective interactions between the monomers of the PE chain. For a good solvent, the monomers only interact via repulsive volume interactions and effective electrostatic interactions due to condensed counterions. However, there are additional volume interaction terms between monomers in the case of a poor solvent, and these attractive interactions may result in a more fluid-like behavior in the collapsed conformation of the PE in the poor solvent as compared to that in the good solvent at the same charge density. In earlier work on understanding the dynamics of collapsed conformations of strongly charged polymers [153], it was also suggested that for the not so poor solvent quality a Wigner crystal conformation is to be expected whereas for poor solvent conditions Wigner glass-like structures are expected. Though we cannot confirm the glassy behavior, we can conclude that the behavior of the system is more fluid-like.

3.6 Discussion

In this chapter, we described theoretically and by means of MD simulations the nature of a collapsed state of a polyelectrolyte (PE) for different strengths of electrostatic and volume interactions. Our main results can be summarized as follows.

The main objective of this work is to identify the correct theory describing the collapse of a PE. The detected scaling from the MD simulations ($R_g \sim N_m^{1/3} \ell_B^{-1/2}$) is not consistent with the predictions of the theories of fluctuating dipoles ($R_g \sim N_m^{1/3} \ell_B^{-2/3}$) [17, 18, 141, 142], or those from the theory of the amorphous ionic solid ($R_g \sim N_m^{1/3} \ell_B^{0}$) [16], but agrees with those from the counterion fluctuation theory [15]. At the same time, we observe other scaling regimes which are not consistent with any of the existing theories.

Using MD simulations, we studied the collapsed regime for a PE in both good and poor solvents. We identify different sub-regimes at different ℓ_B depending on the packing fraction of the particles inside the collapse. In the case of a good solvent, we observe two collapsed regimes, that we call as *weak* and *strong electrostatic regimes*. In the first regime, the radius of gyration R_g of a chain scales with Bjerrum length ℓ_B as $R_g \sim \ell_B^{-1/2}$ while in the second one $R_g \sim \ell_B^{-1/5}$. This scaling is robust and is independent of the valency of the counterions, volume interaction models between chain monomers and solvent models. Whereas, the collapsed phase of a PE chain in a poor solvent consists of several sub-regimes, characterized by different power law scaling of R_g with ℓ_B ($R_g \sim \ell_B^{-\gamma}$).

We generalize the counterion fluctuation theory [15] in such a way as to accommodate the additional observed scaling regimes. In the original theory, the volume interaction is truncated with two-body interactions and gives a scaling $R_g \propto \ell_B^{-1/2}$. From the MD simulations, we have seen the emergence of an additional scaling regime with the increase in ℓ_B due to the increase in the packing fraction of the particles inside the collapse. Then, truncating the volume interaction at the two-body interaction cannot work for systems with higher packing fractions, therefore we modify the volume interactions including more terms in the virial expansion depending on the nature of the packing fraction. In the case of a good solvent, truncating the virial expansion at the third term is enough to explain the weak and strong electrostatic regimes, whereas in the case of a poor solvent, the truncation of the virial expansion depends on several factors such as the charge density, solvent quality etc. The most dominant sub-regimes have origins in the second ($\gamma = 1/2$) and third ($\gamma = 1/5$) virial coefficients, when the packing fraction of PE monomers in the collapsed phase is small. As the packing fraction increases, additional sub-regimes with an effective power law exponent $\gamma < 1/5$ start to appear. We observe that the effective γ decreases continuously with ℓ_B, which demonstrates the contribution of additional terms in the virial expansion.

We also demonstrate that the condensation of counterions on a PE chain leads to an effective renormalization of the volume virial coefficients. The renormalized virial coefficients strongly depend on the valency of counterions and the strength of the poor solvent, which is characterized by the value of ε_{LJ} - the energy parameter of the LJ potential. Surprisingly, the MD results for a particular set of parameters for the volume interaction potential show, via the presence of a sub-regime with the exponent $\gamma = 1/2$, that the renormalized second virial coefficient $\tilde{B}_2$ is positive. This is contrary to the expectation for $\tilde{B}_2$ to be negative, as the simulations were performed for a poor solvent. We note that, while in MD simulations the solvent quality can be controlled by the interaction potential between monomers, in a theory this property is characterized by the sign of the second virial coefficient: B_2 is positive ($B_2 > 0$) for a good solvent and negative ($B_2 < 0$) for a poor one. It is not clear, however, whether this definition of solvent quality, based only on monomer-monomer interactions, remains meaningful for charged polymers in the presence of counterions. Within our generalized theory, we expect that the sign of the renormalized $\tilde{B}_2$ will be manifested in MD simulations through the presence of the sub-regime, $R_g \sim \ell_B^{-\gamma}$, with the exponent $\gamma = 1/2$ for $\tilde{B}_2 > 0$ and absence of this regime for $\tilde{B}_2 < 0$.

To understand the role of condensed counterions on the sign of renormalized $\tilde{B}_2$, we performed a theoretical analysis as well as additional simulations in which we varied the size of the counterions and demonstrated that the appearance and disappearance of the sub-regime with $\gamma = 1/2$ crucially depends on the size of the counterions. This dependence of the sign of the renormalized $\tilde{B}_2$ on the counterion size and valency occurs only for a poor solvent, as the condensed counterions can modulate the effective attractive interactions between monomers resulting in the alteration of the sign of $\tilde{B}_2$. For a good solvent, with repulsive interactions between the monomers, the counterion size and valency play no role.

The original counterion fluctuation theory [15] predicts that the electrostatic internal energy of the system, E_{el}, scales with the radius of gyration as $E_{\mathrm{el}} \sim R_g^{-1}$. At the same time, the dependence of internal energy associated with the volume (LJ) interactions is expected to be different for different sub-regimes, similar to the dependence of R_g on ℓ_B described above. The MD simulation results are in complete agreement with these predictions. We also note that the values of R_g at which the crossover from one sub-regime of $E_{LJ}(R_g)$ to another take place coincide with the values of R_g where the crossover between regimes with different exponents γ are detected.

The different regimes of electrostatic collapse observed in the MD simulations reported here may be experimentally realized as well. In organic solvents, like mixtures of water and alcohol, the dielectric permittivity may be reduced (≤ 18) leading to a large Bjerrum length ($\ell_B \sim 10$) and collapse of a biological PE like DNA has been observed experimentally [13] under such conditions. We note that if all monomers of DNA were charged, one obtains $\ell_B \simeq 29$ and the range of these experimentally realizable ℓ_B values are similar to the ones considered in this study. Another system with a comparably high linear charge density is a solution of charged worm-like micelles [160–162]. We hope that experimentalists find it interesting to check the existence of different collapse regimes for different counterion valencies and sizes.

We also observed a crystalline-like conformation at very high charge density. The nature of this conformation is different for different solvent qualities. Further studies need to be performed to classify the nature of this crystalline state and its properties.

Chapter 4

Aggregation dynamics of rigid PEs

The dynamics of aggregation of rigid PEs are studied using large scale molecular dynamics simulations. We show that the number of aggregates decrease with time as power laws with exponents that are, within numerical uncertainty, independent of the charge density of the polymers, valency of the counterions, density, and length of the PE chain. We find that the morphology of the aggregates depends on the value of the charge density of the polymers. For moderate values of charge density, the shape of the aggregates is cylindrical with height equal to the length of a single PE chain. However, for larger values of charge density, the linear extent of the aggregates increases as more and more polymers aggregate. We model the aggregation dynamics using the Smoluchowski coagulation equation with kernels determined from the molecular dynamics simulations and justify the numerically obtained value of the exponent. Our results suggest that once counterions condense, effective interactions between PE chains are short-ranged and the aggregation of PEs are diffusion-limited. The results of this chapter has been published in Ref. [163].

4.1 Introduction

Rigid PEs are an important class of PEs for which the persistence lengths of the polymer backbone are larger than their contour lengths. Many biologically relevant polymers such as DNA, actin and microtubules are examples of rigid PEs. They may aggregate into bundles in the presence of counterions [2, 78–82]. The Fig. 4.1 shows snapshots of a system of $N = 100$ rigid PEs with chain length $N_m = 30$ at different times. It is evident that the PEs aggregate and the number of clusters decrease with time. The aggregates of biological polymers play an important role in cell scaffolding and possess superior mechanical properties compared to well known synthetic flexible polymers [21, 22]. More recently, it has been possible to synthesize non-biological polymers with comparable backbone stiffness and the ability of these polymers to aggregate is an important parameter in using them as functional biomimetic materials, for instance artificial cytoskeletal or extracellular matrix [20, 164]. With recent studies on various biological phenomena such as DNA packaging, cytoskeletal organization, understanding counterion mediated aggregation of charged polymers becomes very relevant [19, 165].

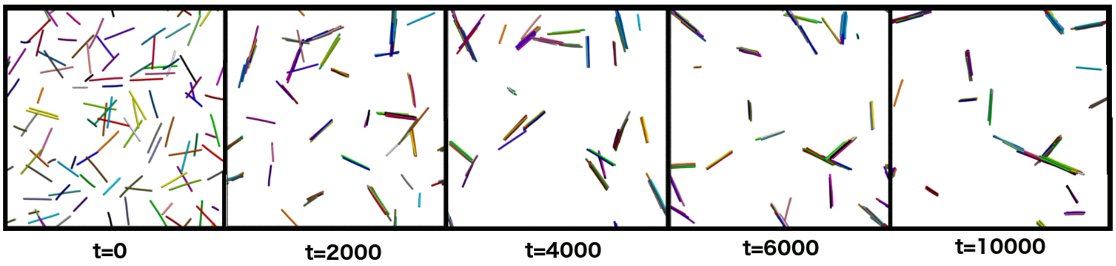

Figure 4.1: Snap shot of system at different time for $\ell_B = 3.57$ and $Z = 3$. The counterions are not shown for better clarity.

The aggregation of rigid PE chains has been studied extensively via experiments [2, 101–109], simulations in the presence and absence of salt/solvent [89–100] and using theoretical approaches [110–118]. While it has been fairly well established that multivalent counterions induce aggregation among the similarly charged PEs, the ability of monovalent counterions to induce a similar aggregation is debated [91, 94, 95, 97, 100, 102–

106, 109, 110, 114, 166–171]. There are some experimental [102–104, 166, 167] and theoretical [110, 114] results argues that the monovalent counterions cause aggregation. At the same instant, other experimental [105, 106], theoretical [169, 170, 172] and numerical [91, 94, 95, 97, 100, 171] studies report the absence of aggregation in the presence of monovalent counterions. It has been showed, using molecular dynamics simulations as well as computing potential of mean force, that for high enough charge density along PE backbone, monovalent counterions also induce aggregation [173].

While the aspect of attraction between similarly-charged PE chains, typically using coarse-grained bead-spring models, is numerically well-studied in the literature [90–99], the dynamics of aggregation of such PE chains is less studied. This is in part due to the computational cost of simulating large number of PE chains with long-ranged Coulomb interactions. Using a hybrid Monte Carlo scheme, and simulating a system with 61 PE chains, it was argued that for intermediate values of the charge density, finite-size PE bundles exist at thermodynamic equilibrium, while further increase of charge density, results in phase separation and precipitation [92, 93]. Using similar parameters, the time dependence of the number of clusters were obtained in Refs. [89, 90]. The numerical data was modeled by the Smoluchowski coagulation equation which is the basis of classical mean-field model of understanding aggregation kinetics [174], and the number of clusters decrease with time as t^{-1}. However, the coagulation kernel derived by considering the particles with equal masses and sizes. This assumption seems unreasonable as the aggregate sizes become heterogeneous with time. In addition, it is not very clear how parameters such as the valency of the counterions, the charge density of PE chains, or the overall number density of the system, affect the aggregation dynamics. In this chapter, we numerically study and model the dynamics of rigid PE in detail.

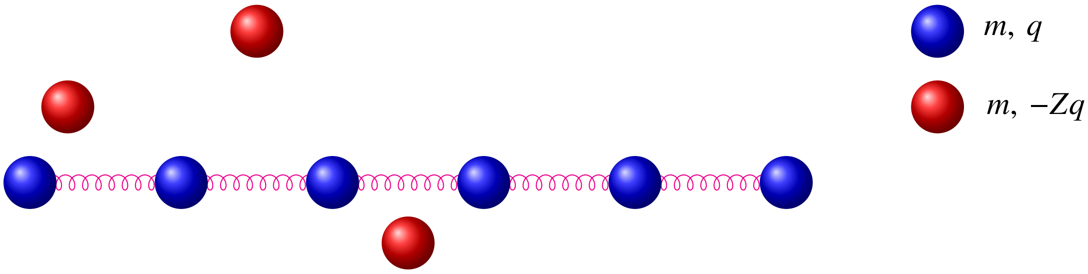

Figure 4.2: Bead-spring model of a rigid PE chain and counterions. The monomer is represented by blue spheres and the counterion by red spheres. m and q are mass and charge respectively. Z is the valency of counterions. The binding energy of the inter-monomer springs are set to a high value such that the PE remains rigid for the temperatures considered.

4.2 MD simulation details

We consider a system of N rigid PE chains. Each PE chain consists of N_m monomers, of charge $+q$, connected by bonds as shown in Fig. 4.2. The counterions have charge $-Zq$, where Z is the valency of the counterion. In this work, we consider $Z = 2, 3$ corresponding to divalent and trivalent counterions respectively. We have not considered monovalent counterions due to it's large simulation time. The number of counterions are chosen such that the system is overall charge neutral. The interactions between the particles are described below.

Excluded volume: The excluded volume interaction is modeled by the 6-12 Lennard Jones potential

$$U_{LJ}(r_{ij}) = 4\varepsilon_{ij}\left[\left(\frac{\sigma_{ij}}{r_{ij}}\right)^{12} - \left(\frac{\sigma_{ij}}{r_{ij}}\right)^{6}\right], \tag{4.1}$$

where r_{ij} is the distance between particles i and j, ϵ_{ij} is the minimum of the potential and σ_{ij} is the inter-particle distance at which the potential is zero. Both ε_{ij} and σ_{ij} are (in reduced units) set to $\varepsilon_{ij} = \varepsilon_{LJ} = 1.0$ and $\sigma_{ij} = \sigma = 1.0$ for all pairs of particles. The Lennard Jones potential is chosen to be zero beyond a cut-off distance $r_c = \sigma$, such that the excluded volume interaction between all pairs is purely repulsive.

Coulomb: The electrostatic interaction is

$$U_c(r_{ij}) = \frac{q_i q_j}{4\pi\epsilon_0 r_{ij}}, \tag{4.2}$$

where q_i and q_j are the charges of i^{th} and j^{th}particle, and ϵ_0 is the permittivity.

Bond stretching: The nearest-neighbour monomers along the PE chains are connected by harmonic springs with the potential

$$U_{bond}(r_{ij}) = \frac{1}{2}k(r_{ij} - a)^2, \tag{4.3}$$

where k is the spring constant and a is the equilibrium bond length. We set $a = 1.12\sigma$ and $k = 500.0$.

Bond bending: Bending of the bond is controlled by following potential

$$U_\theta(\theta) = k_\theta[1 + \cos\theta], \tag{4.4}$$

where θ is the angle between the bonds. The strength of this interaction is set to a large value $k_\theta = 1000.0$ for rigid PE.

All the simulations are performed for $N = 100$ PE chains at values of linear charge density, ℓ_B as defined in Eqn. (1.1), that are larger than the critical value beyond which the PEs aggregate, as determined in Ref. [173]. A variety of parameters such as ℓ_B, valency of the counterions, PE chain length and density of the system are varied and the details of the systems simulated are given in Table 4.1. The analyses are performed over 20 initial conditions for each set of parameter values in Table 4.1.

The equations of motion are integrated in time using the molecular dynamics simulation package LAMMPS [175, 176]. The simulations are carried out at constant temperature (T=1.0), maintained through a Nosé-Hoover thermostat (coupling constant = 0.1) [130, 131]. The long-ranged Coulomb interactions are evaluated using the particle-

valency (Z)	charge density (ℓ_B)	chain length (N_m)	Density (ρ)
3	2.01	30	ρ
	3.57	30	0.75ρ
	3.57	30	ρ
	3.57	30	1.5ρ
	3.57	30	2ρ
	4.52	30	ρ
	5.57	30	ρ
	6.75	30, N=50	ρ
	6.75	30, N=100	ρ
	6.75	30, N=200	ρ
	8.03	30	ρ
2	3.57	15	ρ
	3.57	30	ρ
	3.57	60	ρ
	5.58	30	ρ
	14.28	30	ρ

Table 4.1: The different values of valency of counterions (Z), charge density ℓ_B, PE chain length (N_m), and density used in the MD simulations. Density is expressed in terms of $\rho = 3.8 \times 10^{-4}$. The analyses are performed over 20 initial conditions for each set of parameter values.

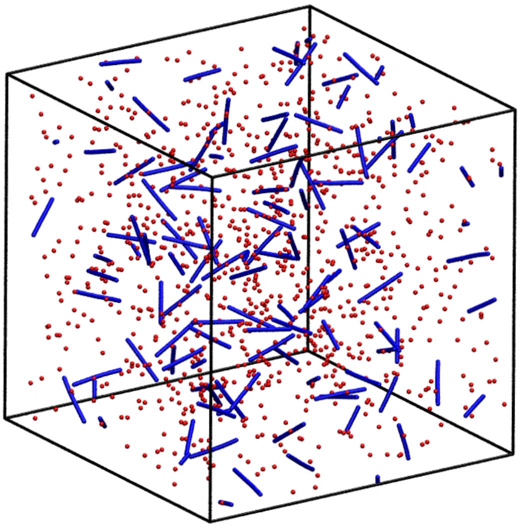

Figure 4.3: Snapshot of a typical initial set up consist of $N = 100$ rigid PEs.

particle/particle-mesh (PPPM) technique [177]. The time step for integrating equations of motion is chosen as 0.001. A homogeneous initial state is prepared as follows. N non-overlapping PE chains of length N_m are placed in a cubic box with periodic boundary conditions with randomly distributed counterions. The charge density of the PE chains is set to a very small value ($\ell_B = 0.22$) much below the critical charge density corresponds to manning condensation, which ensures that counterions do not condense onto the PE chains initially. The system is then evolved to ensure homogeneous distribution of the PE chains and the counterions. Twenty random configurations, as shown in Fig. 4.3, which are temporarily well separated, are chosen and appropriate values of ℓ_B are chosen for further simulations.

4.3 Results

4.3.1 Aggregation dynamics

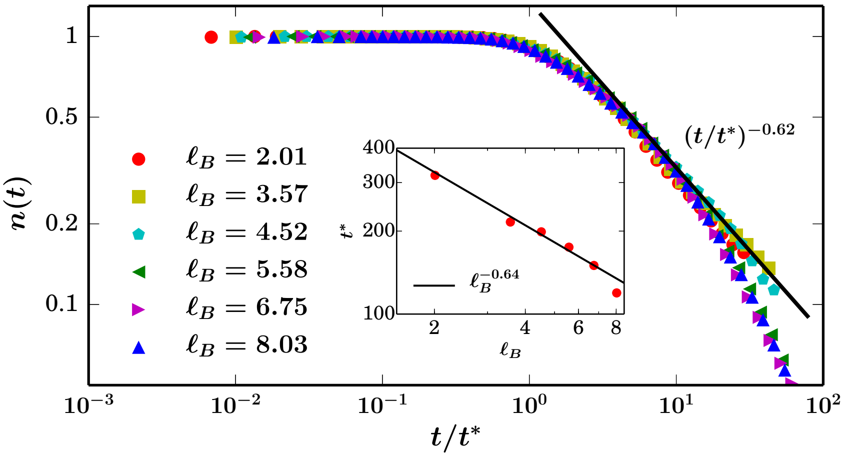

Figure 4.4: The variation of the fraction of aggregates $n(t)$ with scaled time t/t^* for different values of ℓ_B for systems with trivalent counterions. t^* is the time at which $n = 0.9$. The straight line corresponds to power law $(t/t^*)^{-0.62}$. Insets shows the dependence of t^* on ℓ_B.

Two PEs are said to form an aggregate of size two if the distance between any two monomers (not from the same PE) is less than 2σ, and the same definition is extended to an aggregate of size m. We first present results for the temporal dependence of number of aggregates. Fig. 4.4 shows the fraction of aggregates $n(t) = N(t)/N(0)$, as a function of time t/t^* for trivalent counterions. Here, $N(t)$ is the number of aggregates at time t, and t^* is the time taken for number of clusters to reach 90% of $N(0)$. For small times

$n(t) \approx 1$ and aggregation is initiated only after t^*, which is the time taken for counterion condensation to occur. Beyond t^*, $n(t)$ decreases as a power law $t^{-\theta}$. From Fig. 4.4, we find that the exponent θ is independent or utmost very weakly dependent on ℓ_B and has the value $\theta = 0.62 \pm 0.07$.

The crossover at large ℓ_B

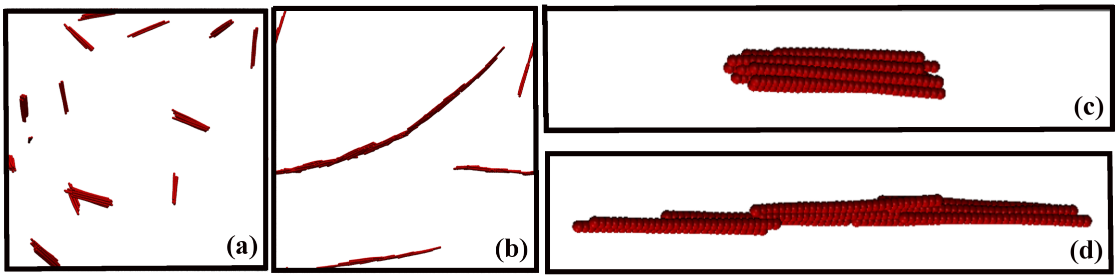

Figure 4.5: Snapshots of systems with trivalent counterions for (a) $\ell_B = 2.01$ and (b) $\ell_B = 8.03$. In (c) and (d), magnified images of clusters of size 10 in the snapshots of (a) and (b) are shown. (Counterions are not shown in the picture for the sake of clarity.)

For systems with trivalent counterions and large ℓ_B, we find that $n(t)$ deviates from the power law behavior at long times (see Fig. 4.4). To understand this crossover, we study the morphology of the aggregates. Figure 4.5 shows snapshots of the system for $\ell_B = 2.01$ and $\ell_B = 8.03$ in (a) and (b), along with enlarged snapshots of aggregates of size 10 in (c) and (d). For smaller values of ℓ_B, the aggregates are cylindrical in shape with length of the aggregate being roughly the same as the length of a PE, while for larger ℓ_B, the aggregates are linear but with larger aggregates having longer length. For very high ℓ_B, the aggregates are linear with larger aggregates having longer length, and the crossover seen in Fig. 4.4 at large times is only for these values of ℓ_B. One possible reason for the crossover is the setting in of finite size effects since it is possible that the length of the aggregates for these systems may span the simulation box at long times. To check the possibility of finite size effects, we simulated systems with trivalent counterions and $\ell_B = 6.57$ for different number of PE chains ($N = 50, 100, 200$) keeping the density fixed. The variation of the fraction of clusters with time is shown in Fig. 4.6 (a). Initially, the

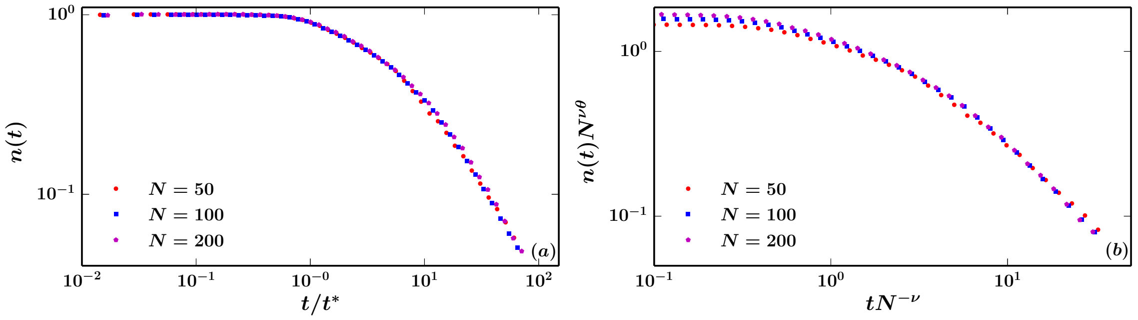

Figure 4.6: (a) The variation of $n(t)$, the fraction of aggregates with scaled time t/t^* for systems with trivalent counterions and $\ell_B = 6.57$ for different number of PE chains N. (b) The data for different N collapse onto a single curve when scaled as in Eqn. (4.5) with $\nu = 0.16$ and $\theta = 0.62$.

data for the different system sizes lie on top of each other, showing that the system size plays no role. At later times, however, they deviate slightly from each other with the data for larger system sizes deviating at later times. Let this crossover time be denoted by $t_c(N)$. We expect $t_c(N) \sim N^\nu$. Assuming finite size scaling, we write

$$n(t) \simeq N^{-\nu\theta} g(tN^{-\nu}), \tag{4.5}$$

where g is a scaling function such that $g(x) \sim x^{-\theta}$ when $x << 1$. The data for the different sizes collapses onto a single curve when scaled as in Eqn. (4.5) with $\nu = 0.16$ [see Fig. 4.6 (b)].

There are two obvious choices for the origin of the finite size effects: one is when the end to end distance of the largest cluster is of the order of the length of the simulation box, and the other when the size of the largest cluster (of mass M) is order of N. In the former case, we find that $t_c \sim M^{1/\theta} \sim N^{2/3\theta}$, where the relation between M and N is obtained from measurements of the morphology of the cluster (see Sec. 4.3.3). In the latter case, $t_c \sim M^{1/\theta} \sim N^{1/\theta}$. Given that $\theta = 0.62$, these two cases give $\nu = 1$ and $\nu = 1.5$, both very different from the numerical value of $\theta = 0.16$ obtained above. Given that the origin of ν remains unclear, and also because the system sizes being considered are small and the numerically observed finite size effects are slight, it is possible that the crossover is due to different dynamics setting in at larger times. Another explanation could be that systems which have such collinear-type aggregates follow very different dynamics, the study of which requires computationally expensive simulations of much larger system sizes. In this chapter, we restrict the discussion to times smaller than this crossover time.

Universality of the exponent, θ

Similar to Fig. 4.4, The variation of the fraction of aggregates $n(t)$ with scaled time t/t^* for different values of ℓ_B for systems with divalent counterions is shown in Fig. 4.7 (a). It is evident that the exponent θ is same for divalent counterions as is for trivalent counterion also. In an earlier paper [173], it was shown that monovalent counterions induce aggregation among similarly-charged PE chains, and preliminary data suggested $\theta \approx 0.66$. This, being consistent with the results obtained in this work for divalent and trivalent counterions, we conclude that the dynamics is independent of valency of counterions. The charge density required for aggregation with monovalent counterions is much larger than that for divalent and trivalent counterions, resulting in much longer simulations needed for obtaining good data. For efficient computational purposes, we restrict the simulations in this work to divalent and trivalent counterions. We also confirm that the exponent θ does not depend on the density ρ and N_m, the length of the PE chain, as can be seen from the collapse of the data for different ρ and N_m onto one curve [see Fig. 4.7 (b) and (c)]. We

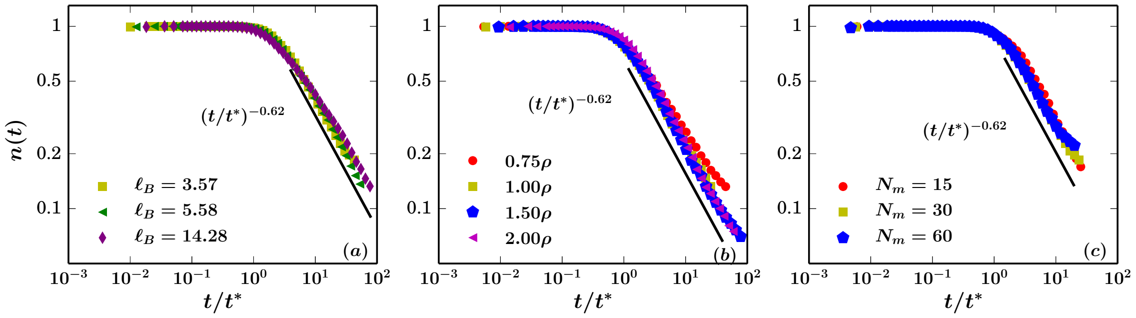

Figure 4.7: The variation of the fraction of aggregates $n(t)$ with scaled time t/t^* for (a) different values of ℓ_B for systems with divalent counterions, (b) different densities and trivalent counter ions for $\ell_B = 3.57$, and (c) different PE length N_m and divalent counter ions for $\ell_B = 3.57$.

thus conclude that the exponent θ characterizing the power law decay of number of aggregates is quite universal and does not appear to depend on parameters such as valency, density or length of the PE. It is thus plausible that aggregation is driven by diffusion and irreversible aggregation (we do not see any fragmentation event) due to short-ranged attractive forces. With this assumption, we recast the aggregation dynamics of PE in terms of the Smoluchowski equation in Sec. 4.3.3.

4.3.2 Two kinds of dynamics

For large values of ℓ_B, we observed that the aggregates are collinear with the effective length increasing with size of aggregate [see Fig. 4.10 (b)]. However, we find that such aggregates, when isolated, rearrange themselves from elongated to more compact cylindrical structures whose lengths are comparable to that of a single PE chain. To quantify this, we extract aggregates of size 3 and 10 from the simulations for $\ell_B = 8.03$ and with trivalent counterions, isolate them, and allow them to evolve for different values of ℓ_B. A typical time profile of the end to end distance, R_{ee} is shown in Fig. 4.8 (a). It decreases in steps with sudden decreases in length due to re-arrangement, separated in time. From the history averaged data (see Fig. 4.8), a relaxation time associated with the rearrangement (call as sliding time, τ) may be extracted.

Thus, there are two time scales in the problem: one is the diffusion time scale corresponding to the time taken for two aggregates to be transported nearby, and the second is the sliding time scale τ corresponding to the time taken for an aggregate to re-align itself into a compact cylindrical shape. The sliding time scale increases rapidly with ℓ_B as seen in Fig. 4.8 (b). For large ℓ_B, the sliding time scale is much larger than the diffusion time scale and the re-alignment may be ignored.

We also find that the process by which two aggregates merge are different for small and large ℓ_B. For small ℓ_B, when two PEs merge, they first orient in orthogonal directions, and

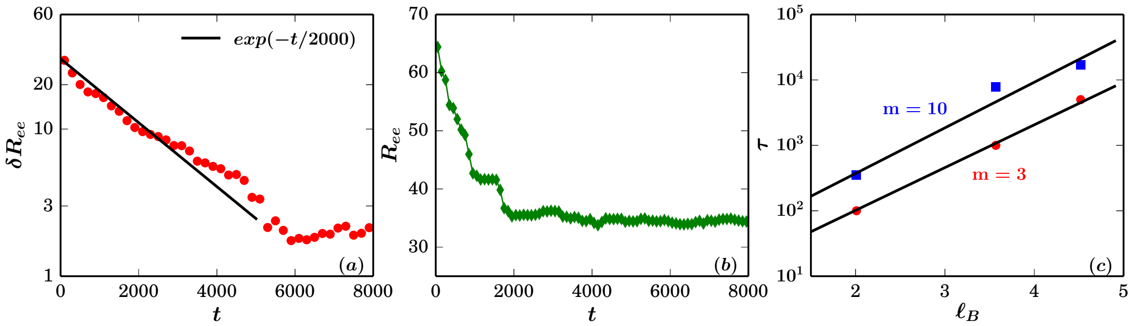

Figure 4.8: The deviation of the end to end distance of the aggregate, δR_{ee}, from its equilibrium value as a function of time t. It decreases with time as an exponential. The data is for an aggregate of size three with trivalent counterions, $\ell_B = 3.57$ and averaged over three realizations. (a) The end to end distance R_{ee} for a single realization for the same parameters as in main plot. (b) The variation of the relaxation times τ with ℓ_B for different aggregate sizes. The straight lines are $\exp(1.51\ell_B)$ ($m = 3$) and $\exp(1.61\ell_B)$ ($m = 10$).

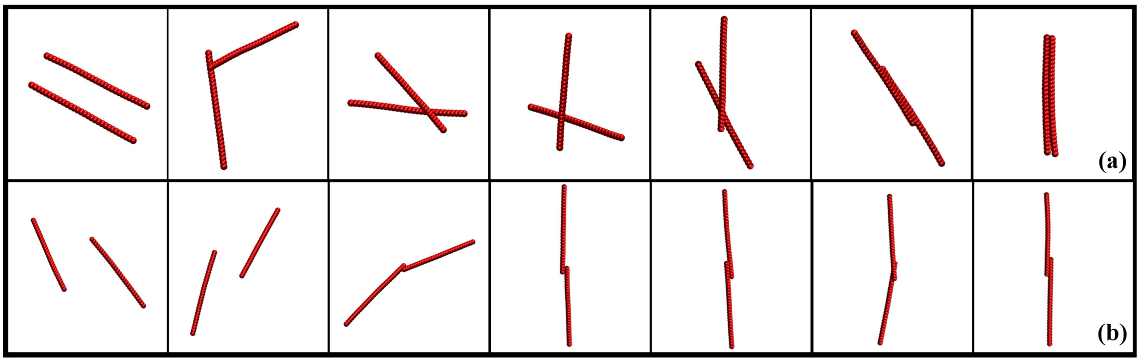

Figure 4.9: Snapshots describing the merging of two PEs for (a) $\ell_B = 2.01$ (b) $\ell_B = 8.03$ for a system with trivalent counterions.

the point of intersection moves towards the center. At later times, they align and rearrange themselves from elongated to more compact cylindrical structures [see Fig. 4.9 (a)]. For large ℓ_B, the aggregates intersect and align themselves without sliding [see Fig. 4.9 (b)].

4.3.3 Modeling using Smoluchowski equation

The Smoluchowski equation describes irreversible aggregation of particles that are transported by some mechanism such as diffusion or ballistic motion. These equations are widely applied in phenomena like polymerization, aggregation of colloidal particles, formation of stars and planets, behavior of fuel mixtures in engines etc [178]. Smoluchowski equation provides a macroscopic description for the evolution of the densities in a system whose particles are prone to binary aggregation. These equation comes in two flavors: discrete and continuous. The aggregate mass may take values in the set of positive integers in the case of discrete version, whereas the aggregate mass takes values in $\mathbb{R}^+$ in the continuous version [179].

In Sec. 4.3.1, we showed that the PE aggregation dynamics is independent of PE charge density (ℓ_B) and valency of counterions (Z). We model the aggregation as one of diffusing neutral rod-like particles that aggregate due to short-ranged attraction. The Smoluchowski equation for irreversible aggregation (for reviews, see [23, 180]) is

$$\frac{dN(m,t)}{dt} = \frac{1}{2}\sum_{m_1=1}^{m-1} K(m_1, m-m_1)N(m_1)N(m-m_1) - \sum_{m_1=1}^{\infty} K(m, m_1)N(m)N(m_1), \tag{4.6}$$

where $N(m,t)$ is the number of aggregates of size m at time t, and $K(m_1,m_2)$ is the rate at which two masses m_1 and m_2 collide. The first term in Eqn. (4.6) describes the aggregation of particles to form an aggregate of size m, while the second term describes the loss of an aggregate of size m due to collision with another aggregate.

If the kernel $K(m_1,m_2)$ is a homogeneous function of its arguments with homogeneity exponent λ, i.e., $K(hm_1,hm_2) = h^\lambda K(m_1,m_2)$, then the number of aggregates $N(t) = \sum_m N(m,t)$, decreases in time as a power law $N(t) \sim t^{-\theta}$, where

$$\theta = \frac{1}{1-\lambda}, \quad \lambda < 1. \tag{4.7}$$

To construct the kernel $K(m_1,m_2)$, we consider the aggregates to be effective spheres of radius $\sqrt{\ell^2 + r^2}$, where ℓ and r are the the height and radius of the cylindrical aggregate. This is justified because we observe that the aggregates rotate at a rate that is much larger than the rate of collision. For diffusing spheres in three dimensions, the coagulation kernel is known to be (for example, see [181])

$$K(m_1,m_2) \propto [D(m_1)+D(m_2)][R(m_1)+R(m_2)], \tag{4.8}$$

where $D(m)$ and $R(m)$ are the diffusion constant and effective radius of an aggregate of size m. In the absence of a solvent, the diffusion constant is inversely proportional to mass of an aggregate

$$D(m) \propto m^{-1}. \tag{4.9}$$

The dependence of the radius $R(m)$ on m may be determined by studying the geometry of the aggregates obtained from the MD simulations. The geometry of an aggregate may be quantified by the eigenvalues of the gyration tensor S defined in Eqn. (1.9). Let the eigenvalues be denoted by λ_1, λ_2, and λ_3, where $\lambda_1 \geq \lambda_2 \geq \lambda_3$. Modeling the shape of the aggregate as a cylinder, we obtain the length and radius of the aggregate to be $\ell = \sqrt{12\lambda_1}$ and $r = \sqrt{2(\lambda_2+\lambda_3)}$. The length and radius, thus measured, are shown in Fig. 4.10 for $\ell_B = 2.01$ and $\ell_B = 8.03$. For small values of ℓ_B, ℓ is independent of aggregate size m, i.e. $\ell \sim m^0$, while the radius r increases with m as $r \sim \sqrt{m}$ [see Fig. 4.10 (a)]. For large values of ℓ_B, we find that $\ell \sim \sqrt{m}$ and $r \sim \sqrt{m}$ [see Fig. 4.10 (b)]. Thus, aggregation is controlled by two types of kernels

$$\frac{K(m_1,m_2)}{m_1^{-1}+m_2^{-1}} \propto \begin{cases} \sqrt{N_m^2+m_1}+\sqrt{N_m^2+m_2} & \text{if } \ell_B \gtrsim \ell_{Bc} \\ \sqrt{m_1}+\sqrt{m_2} & \text{if } \ell_B \gg \ell_{Bc}, \end{cases} \tag{4.10}$$

where ℓ_{Bc} is the critical charge density beyond which aggregation sets in. The radius and length of cluster are calculated from the eigenvalues of gyration tensor, defined in Eqn. (1.9).

For $\ell_B \gg \ell_{Bc}$, the kernel is homogeneous with homogeneity exponent $\lambda = -1/2$. From Eqn. (4.7), we obtain $\theta = 2/3$. This is in excellent agreement with the numerical value of 0.62 ± 0.07 from molecular simulations, as described in previous section. When $\ell_B \gtrsim \ell_{Bc}$,

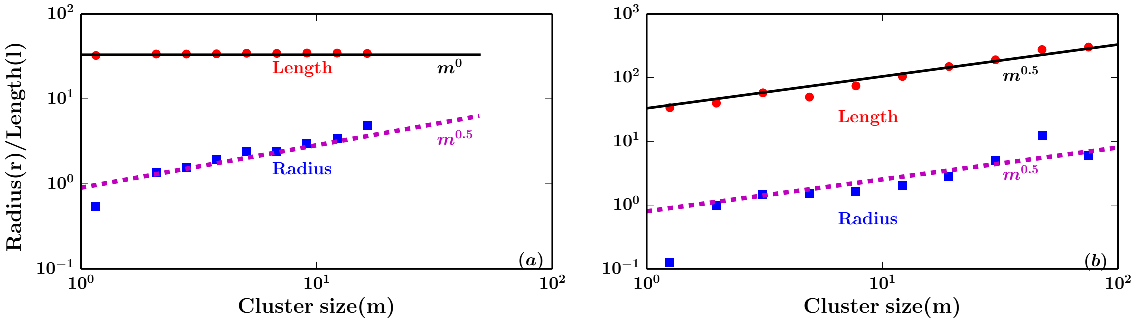

Figure 4.10: The length and radius of different cluster sizes m for (a) $\ell_B = 2.01$ and (b) $\ell_B = 8.03$.

the kernel is no longer homogeneous. For large m_1 and m_2, it is homogeneous with $\lambda = -1/2$. Equation (4.7) gives $\theta = 2/3$. On the other hand, for small m_1, m_2, we may ignore the dependence of radius on mass, and the kernel is homogeneous with $\lambda = -1$ or equivalently $\theta = 1/2$. The numerically obtained value of 0.62 ± 0.07 lies between these two bounds 0.5 and 0.67.

In our MD simulations, computational expense limits the number of PEs that can be studied to few hundreds. However, large-scale Monte Carlo simulations can be used to study the effect of the kernel for $\ell_B \gtrsim \ell_{Bc}$ on the measured θ. In these simulations, we start with $M = 10^5$ particles of mass 1. Any pair of particles of masses m_1 and m_2 undergo aggregation to form a particle of mass $m_1 + m_2$ with rate

$$K(m_1, m_2) = \Lambda(m_1^{-1} + m_2^{-1})(\sqrt{L^2 + m_1} + \sqrt{L^2 + m_2}), \tag{4.11}$$

where L is a parameter and Λ is chosen to be proportional to M^{-2}. Each parameter value was averaged over 1000 histories. The results for $n(t)$ for different parameter values are shown in Fig. 4.11. As L increases the effective power law changes from -0.67 to -0.5, and $\theta = 0.62 \pm 0.07$ from molecular dynamics falls within this range.

From the above analysis based on Smoluchowski equation, we obtain $\theta = 2/3$ very similar to the value obtained through our MD simulations ($\theta = 0.62 \pm 0.07$). More accurate determination of θ through MD simulations will require much larger systems to be simulated

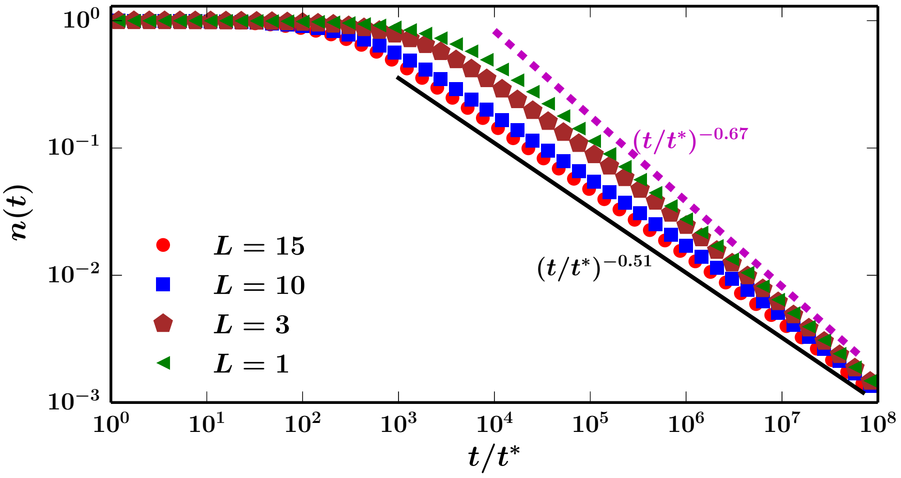

Figure 4.11: Monte Carlo simulations with kernel as in Eqn. (4.11) for different values of the parameter L.

for much longer times, currently a very expensive proposition. In earlier simulations of rigid PEs [90], it was suggested that the decay of the number of aggregates scales with time as t^{-1} different from the exponent obtained in this work ($t^{-0.62}$). This difference could be attributed to the assumption made in the analysis based on Smoluchowski equation in the earlier paper [90] that collisions occur between aggregates of approximately equal size [182]. In this work, we explicitly take into consideration collisions between aggregates of different sizes, which is much more realistic picture and hence we consider the result obtained in this work to be more accurate.

4.4 Discussion

The study on the dynamics of aggregation of similarly-charged rigid PE chains using extensive MD simulations has shown that the dynamics of aggregation is effectively determined by short-ranged interactions between the PE chains, even though the monomers and counterions interact via long-ranged Coulomb interactions. We also showed that the number of aggregates decreases with time as a power law, $t^{-\theta}$, where the exponent θ is independent of the charge density of the PE chains, whether the counterions are divalent or trivalent, number density, and length of the PE chains. The data is modeled using Smoluchowski equation with coagulation kernel determined from the MD simulations. From the molecular dynamics simulations, we estimate $\theta = 0.62 \pm 0.07$, which is consistent with the value $\theta = 2/3$ obtained from the Smoluchowski equation.

It has been argued that for intermediate values of the charge density, finite size PE bundles exist at thermodynamic equilibrium, while further increase of charge density, results in phase separation and precipitation [89, 90, 92, 93]. However, in our simulations, for all the values of charge densities that we have considered, the number of aggregates decrease continuously as a power law, and show no tendency to plateau which would be the case if finite sized bundles at thermodynamic equilibrium existed. In addition, we find that the cluster size distribution for different times obeys a simple scaling $N(m,t) \simeq t^{-2\theta} f(mt^{-\theta})$, where f is a scaling function (see Fig. 4.12), showing that the system continuously coarsens to presumably a phase separated state. This discrepancy in results could be due to the fact that the observation of finite sized bundles in Refs. [89, 90, 92, 93] was based on their short simulations and the system may not reach the equilibrium configuration.

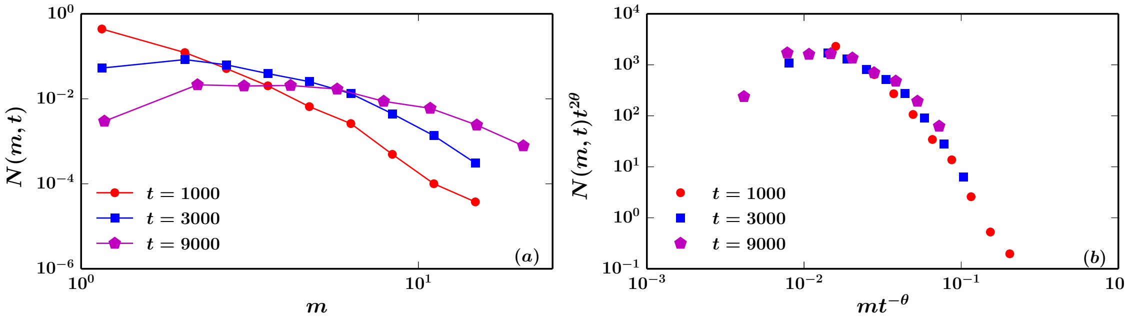

Figure 4.12: (a) Aggregate size distribution $N(m,t)$ for different times t for a system with trivalent counterions and $\ell_B = 2.01$. (b) The data for different times collapse onto a single curve when m and $N(m,t)$ are scaled as shown in the figure with $\theta = 0.62$.

It has also been suggested in literature that similarly-charged rigid PE chains tend to approach each other at right angles, align and then slide to align with the bundle while merging with each other. This mode has been referred in the literature as zipper model [89, 90, 93, 183]. Another model of approach called collinear model was also proposed for rigid PE chains, in which the centers of mass of approaching PE chains lie on a line parallel to their longer axes [183]. This model was shown to have lower kinetic barrier of approach and can explain the observation of elongated structures in experiments [184, 185] similar to that observed in our MD simulation. From our MD simulations, we see that the approach of merging depends significantly on the charge density of rigid PE chains. While zipper model seems to be the mode of aggregation for PE chains with lower charge density, the approach mechanism changes to collinear model for PE chains with high charge density.

Chapter 5

Role of flexibility in aggregation of multiple PEs

In this chapter, using large-scale coarse-grained molecular dynamics simulations, we obtain the phase diagram of the aggregated structures of flexible charged polymers in the presence of trivalent counterions. We also characterize the morphology of the aggregates as well as the aggregation dynamics. In addition to aggregation, we observe fragmentation events as well. Three different phases are observed depending on the charge density: no aggregation, a finite bundle phase where multiple small aggregates coexist with a large aggregate and a fully phase separated state. We show that the flexibility of the polymer backbone causes strong entanglement between charged polymers leading to additional time scales in the aggregation process. These results are contrary to those obtained for rigid polyelectrolytes, emphasizing the role of backbone flexibility in the conformational dynamics of PE. The results presented in this chapter has been published in Ref. [186].

5.1 Introduction

Biological polymers such as proteins are essentially flexible PEs (FPEs) and understanding the mechanism of aggregation of such FPEs is relevant as protein-protein disordered aggregates are implicated in many neurodegenerative diseases [86, 87]. The aggregation mechanism of FPE chains, whose conformational flexibility can introduce additional time scales and barriers in the aggregation dynamics might be different from that of rigid PEs described in chapter 4. The flexibility of FPE chains can possibly introduce additional kinetic barriers due to the disentanglement and subsequent entanglement required for incorporating new FPE chains into an existing aggregate, altering the aggregation dynamics as compared to rigid PE chains. It is possible that during the process to include a new FPE chain, the existing aggregate may fragment into individual PE chains, further complicating the aggregation dynamics. Another aspect of importance is to understand the underlying effective attractive interactions that play a dominant role in aggregation of like-charged FPE chains and whether these interactions are similar to those in the collapsed phase of a single flexible PE chain. In chapter 3, we have shown that the collapsed regime of a single FPE chain (in either good or poor solvent conditions) is composed of multiple sub-regimes. These sub-regimes are characterized by different scaling exponents in the relation between radius of gyration and the effective Bjerrum length (ℓ_B) of the PE chain, especially when the PE chain is strongly charged. Among existing theories to explain the counterintuitive collapse of a charged PE chain [15–18, 140–142], we identified counterion fluctuation theory [15] to be the correct theory and modified it suitably to account for the existence of several sub-regimes in the collapsed phase of a single PE chain. It would be interesting to explore whether similar sub-regimes exist for strongly charged PE chains in their aggregated regime and whether counterion fluctuation theory still holds good for aggregated structures. It can be envisaged that when the strongly charged PE chains self-assemble into an aggregated structure, the counterions are no longer bound to a specific FPE chain but move freely within the aggregate of multiple PE chains and this scenario may not be very different from a collapsed regime of a single long collapsed PE chain.

In this chapter, we study the equilibrium conformations and dynamics of aggregates of highly charged FPE chains, using molecular dynamics (MD) simulations (model and MD details in Sec. 5.2). In Sec. 5.3.1, we discuss the effects of backbone flexibility of FPE chains on the equilibrium phases in the presence of trivalent counterions and contrast them with the results for rigid PE chains with rigid backbones. We also characterize the morphology of the aggregates in detail in Sec. 5.3.2 and study the role of conformation of a single FPE chain in emergence of kinetic barriers that affect the aggregation dynamics. In Sec. 5.3.3, we characterize the dynamics of aggregation in the phase separated state by measuring the power law exponent describing the number of aggregates. Finally, in Sec. 5.4 we provide a detailed discussion of our results.

5.2 MD simulation details

We consider a system of $N = 100$ PE chains, each one consisting of $N_m = 30$ monomers of charge $+q_m$, and corresponding number of neutralizing counterions of charge $q_c = -Zq_m$, where Z is the valency of the counterion as in the case of rigid PE aggregation. In the present study, we only consider trivalent counterions ($Z = 3$) for the computational simplicity. The PE chains are modeled using a bead spring model [163, 173], as in our previous chapters, where the monomers are connected by harmonic springs with the interaction potential

$$U_{bond}(r_{ij}) = \frac{1}{2}k(r_{ij} - a)^2, \tag{5.1}$$

where k is the spring constant and a is the equilibrium bond length. The flexibility of the chain is maintained by not including a three-body bond bending interaction, hence the chains are fully flexible.

Parameters	value
σ	1
a	1.12σ
ε_{LJ}	1
r_c	σ
T	1
k	500

Table 5.1: Parameters used in the MD simulations.

The non-bonded particles interact through 6–12 Lennard Jones potential

$$U_{LJ}(r_{ij}) = 4\varepsilon_{LJ}\left[\left(\frac{\sigma}{r_{ij}}\right)^{12} - \left(\frac{\sigma}{r_{ij}}\right)^{6}\right], \tag{5.2}$$

where r_{ij} is the distance between particles i and j, ε_{LJ} is the minimum of the potential and σ is the inter-particle distance at which the potential is zero. The parameters ε_{LJ} and σ are the same for all pairs of particles. The Lennard Jones potential goes to zero smoothly beyond a cutoff distance [122] r_c ($U_{LJ}(r)) = 0$ for $r > r_c$) between any two particles and is chosen to be σ. This results in purely repulsive interactions between all the particles, implicitly mimicking good solvent conditions.

The electrostatic interaction among all pairs of particles is given by Coulomb interaction

$$U_c(r_{ij}) = \frac{q_i q_j}{4\pi\epsilon_r r_{ij}}, \tag{5.3}$$

where q_i and q_j are the charges of the i^{th} and the j^{th} particles, which can take values q_m or q_c, depending on whether it is a monomer or counterion and ϵ_r is the effective dielectric constant of the medium. The strength of electrostatic interactions in the system can be scaled via dimensionless Bjerrum length ℓ_B, which can be changed either by changing monomer charge q_m keeping effective dielectric constant ϵ_r fixed or by changing ϵ_r and keeping q_m fixed. In our simulations, we systematically scale the monomer charges q_m to vary ℓ_B. Larger the value of ℓ_B, stronger the electrostatic interactions. The PE chains and the corresponding counterions are placed in a box of linear size L with periodic boundary conditions. The equations of motion are integrated in time using the molecular dynamics (MD) simulation package LAMMPS [175, 176] using a time step of 0.001 at temperature $T = 1$ maintained through a Nosé-Hoover thermostat [130, 131]. Details of the interaction parameters are given in Table 5.1. The long-ranged electrostatic interactions are calculated using Particle-Particle/Particle-Mesh (PPPM) technique [177].

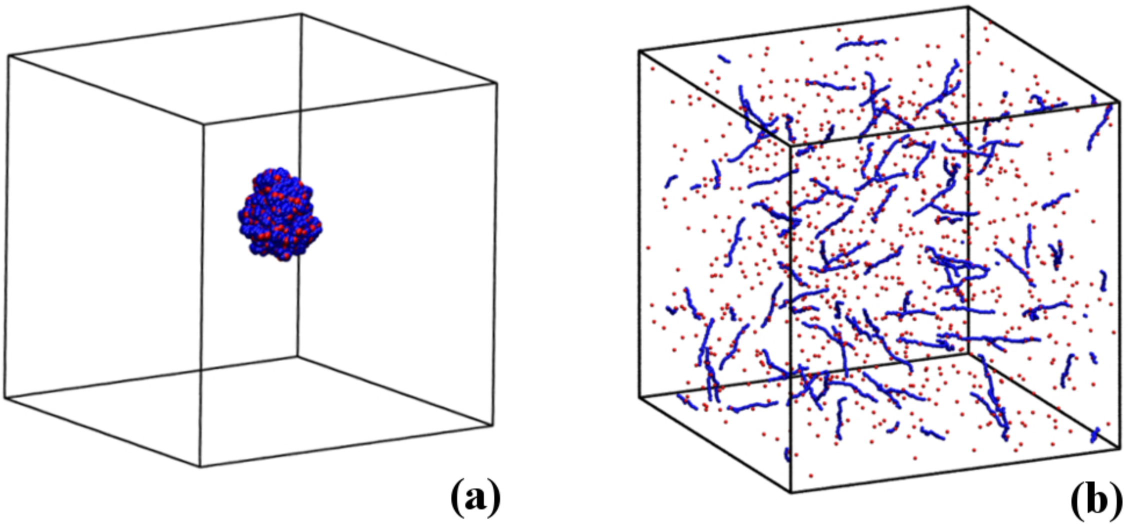

Figure 5.1: Snapshots of the system at the initial configuration for (a) reverse simulations and (b) forward simulations.

We perform two kinds of simulations which differ from each other in their initial conditions. The first set of NVT simulations are used to obtain the different phases that the aggregates may exist and obtain ρ -ℓ_B phase diagram, where $\rho = NN_m/L^3$ is the monomer number density. The initial conditions for these sets of simulations were obtained by performing a NPT ($P = 1$, $T = 1$) simulation of a system of randomly dispersed PE chains and counterions with $\ell_B = 3.57$ (much larger than that of a critical charge density above which counterions condense onto the PE chains and above critical charge density for aggregation) until all the 100 PE chains aggregate into a single aggregate. The corresponding initial configuration is shown in Fig. 5.1 (a). This single aggregate is then evolved in time for different values of ℓ_B and number density ρ (we change the volume of the system keeping the number of monomers fixed) for 10^7 steps to ascertain the stability and morphology of the resultant aggregates. These simulations will be referred to as "reverse simulations" in the chapter. In the second set of NVT simulations, the initial condition is one where all the PE chains and the counterions are dispersed uniformly throughout the simulation box. To ensure that the initial conformations of the PE chains are well dispersed throughout the simulation box, we set the charge density of the PE chains to a very small value ($\ell_B = 0.22$), much less than that of a critical charge density above which counterions condense onto the PE chains ($\ell_{Bc} \approx 1$) and equilibrate the system. Twenty random configurations, which are temporally well separated (time step between two configuration is chosen to be 5000) are chosen for further simulations in which the value of charge density of the FPE chains, ℓ_B, is varied. Here we keep the number density fixed ($L = 129$ and $\rho = 1.43 \times 10^{-3}$ in units of σ) and vary ℓ_B. For each value of ℓ_B considered, 20 independent simulations are performed, each for 10^7 steps. These simulations will be referred to as "forward simulations". An initial configuration for the forward simulation is shown in Fig. 5.1 (b).

5.3 Results

5.3.1 Equilibrium phases and phase diagram

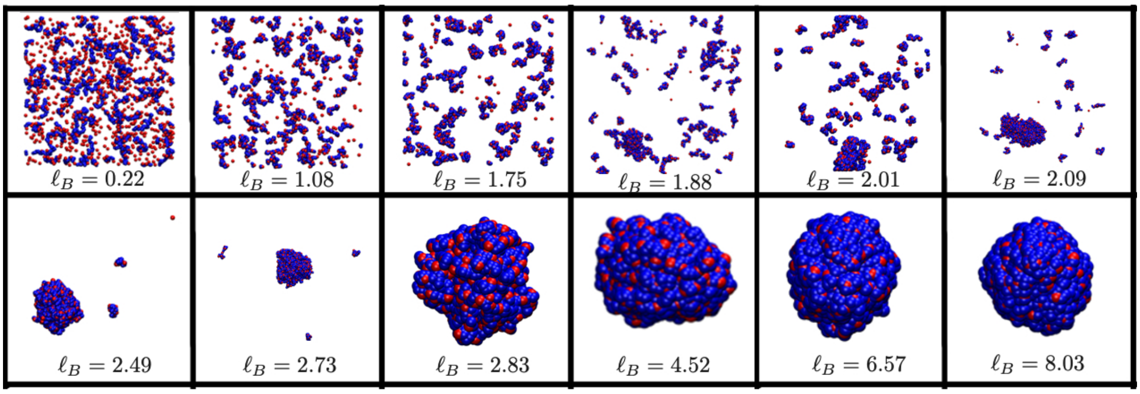

Figure 5.2: Reverse simulations: snapshots of the system at the end of 10^7 MD steps for different values of charge density ℓ_B and at fixed monomer number density $\rho = 1.43 \times 10^{-3}$. The monomers and counterions are colored in blue and red respectively. The snapshots are not to scale.

We first identify the equilibrium phases and phase diagram of a system of flexible PE chains, as a function of PE chain charge density ℓ_B and monomer number density ρ. This can be done in two ways, either using a forward simulation in wherein well dispersed PE chains and counterions as the initial state or by reverse simulation in wherein a large aggregate of size $m = 100$ as the initial state and observe the equilibrium state. The equilibration time for the PEs system in the forward simulation is unknown and is large, it would be difficult to conclusively distinguish between finite bundle formation and fully phase separated states. Setting an arbitrarily fixed equilibration time [92, 93] can potentially lead to erroneous conclusions regarding the phase diagram. The reverse simulations help to avoid this problem. We study the stability of a fully phase separated aggregate structure by performing reverse simulations at various values of ℓ_B and ρ.

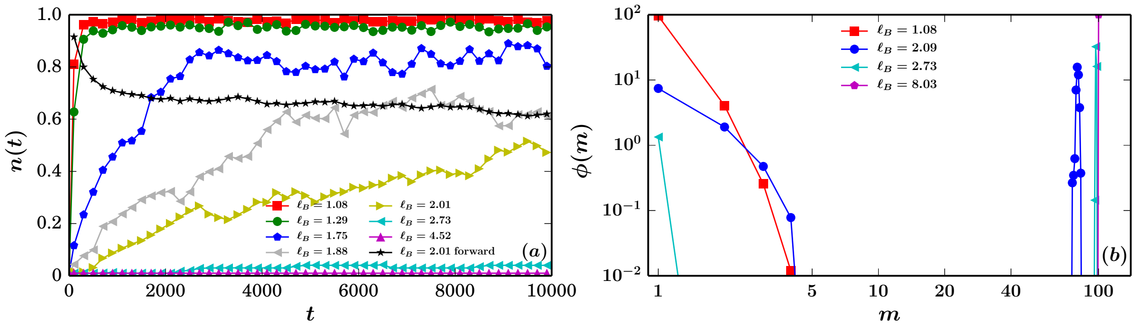

Figure 5.3: (a) The variation of the fraction of aggregates, $n(t)$ with time for different values of the charge density ℓ_B and fixed monomer number density $\rho = 1.43 \times 10^{-3}$ in reverse simulations. The initial condition is one where all PE chains are in one aggregate corresponding to $n(0) = N^{-1} = 0.01$, where N is the total number of PE chains. For intermediate values of ℓ_B, $n(t)$ attains a time-independent constant value between 0.01 and 1, corresponding to the existence of finite-sized bundles. To show equilibration, $n(t)$ for $\ell_B = 2.01$ in forward simulations, averaged over twenty initial conditions, is also shown. (b) $\phi(m)$, the mean fraction of PE chains contained in an aggregate of size m, as a function of m for different values of ℓ_B. The data is for monomer number density $\rho = 1.43 \times 10^{-3}$.

The snapshots of the system at the end of 10^7 steps are shown in Fig. 5.2 for different values of ℓ_B and fixed monomer number density $\rho = 1.43 \times 10^{-3}$. For a given value of ρ, we find that the system may exist in three different phases. These phases correspond to the aggregate being (a) completely fragmented (no aggregation), (b) partially fragmented (finite bundles characterized by the presence of a single large aggregate and multiple small aggregates), or (c) intact (phase separation).

To show the stability of the three phases, the equilibration of the system as well as independence of the final state on the initial conditions have to be checked. To do this, we define a quantity $n(t)$ which quantifies the number of aggregates in the system, irrespective of their size, as in the case of rigid PE described in chapter 4. $n(t)$ takes a value of 1, when there are no aggregates of size more than 1 (completely fragmented state) and $0.01(= 1/N)$ when there is a single aggregate comprising of all PEs (completely phase separated state). For reverse simulations $n(0) = 0.01$ whereas for forward simulations $n(0) = 1$. The variation of $n(t)$ with time in shown in Fig. 5.3 (a). From the figure, three different regions are observed, consistent with Fig. 5.2. For $\ell_B < 1.28$, the initial single aggregate of size 100 fragments completely and $n(t)$ increases from 0.01 to nearly 1. For $1.29 < \ell_B < 2.73$, within the first half of the simulation time, $n(t)$ reaches a steady state value between 0 and 1. From these results, we identify two critical values of charge density denoted by $\ell_{B1} \approx 1.29$ and $\ell_{B2} \approx 2.73$ above which finite bundles and phase separated states appear respectively. We check that in this range of ℓ_B [for example $\ell_B = 2.01$ is shown in Fig. 5.3 (a)] values, the steady state values of $n(t)$ are independent of the initial conditions by doing a forward simulation in which all the PE chains are uniformly distributed within the simulation box. The steady state values from these runs (averaged over 20 initial conditions) as well as from the reverse simulations tend to the same value at large times, showing that the system is equilibrated. For values of ℓ_B larger than 2.73, the initial single aggregate remains intact throughout the simulation time scale suggesting that for these values of ℓ_B complete phase separation is the equilibrium phase.

Characterizing the finite bundle phase only in terms of $n(t)$ is incomplete, as it does not distinguish between many small-size aggregates coexisting with a large aggregate, or a system consisting of only aggregates of small size. To understand more about the coexistence of aggregates, we study the aggregate size distribution. Let $N(m,t)$ be the number of aggregates of size m at time t. The number of aggregates $n(t)$, defined earlier, is then given

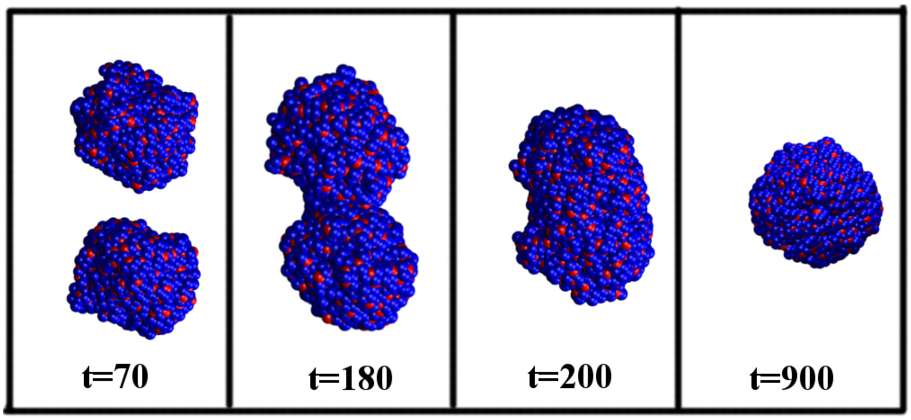

Figure 5.4: Snapshot of merging of two aggregate of size $m = 50$ to form an aggregate of size $m = 100$.

by $n(t) = N^{-1}\sum_m N(m,t)$. Also, it is clear that $\sum_m mN(m,t) = N$ because the total number of PEs is conserved during aggregation. We consider the quantity $\phi(m,t) = mN(m,t)/N$ (where $\sum_m \phi(m,t) = 1$) which measures the fraction of total number of PEs that appears in the form of aggregates of size m, in a given configuration. Once the system reaches equilibrium, the average value of $\phi(m,t)$ reaches a time independent value. We then define $\phi(m) = \langle\phi(m,t)\rangle$, where the average is done over all equilibrium configurations, that is obtained by discarding the initial equilibration run in the backward simulations. Defined this way, $\phi(1) = 1.0$ in fully fragmented phase and $\phi(100) = 1.0$ in a completely phase separated state, with all other $\phi(m) = 0$. The variation of $\phi(m)$ with m for different values of ℓ_B is shown in Fig. 5.3 (b). For $\ell_B = 1.08$, which is in the fully fragmented phase, it can be seen that the peak of the distribution is at $m = 1$ with $\phi(1) \approx 1.0$, showing that the system is made of aggregates of size one. For two values of $\ell_B = 2.09, 2.73$ in the finite bundle phase, the distribution is inhomogeneous and consists of two parts: a peak at large values of m and a decaying distribution for small values of m. This shows that the finite bundle phase consists of the co-existence of a single large aggregate and multiple small-size aggregates. On the other hand, for the fully phase separated state ($\ell_B = 8.03$), the peak of the distribution is at 100, as expected for a stable aggregate of size 100. The aggregate size distribution, along with the data for the total number of aggregates $n(t)$ shown in Fig. 5.3, clearly demonstrates the existence as well as the nature of the finite

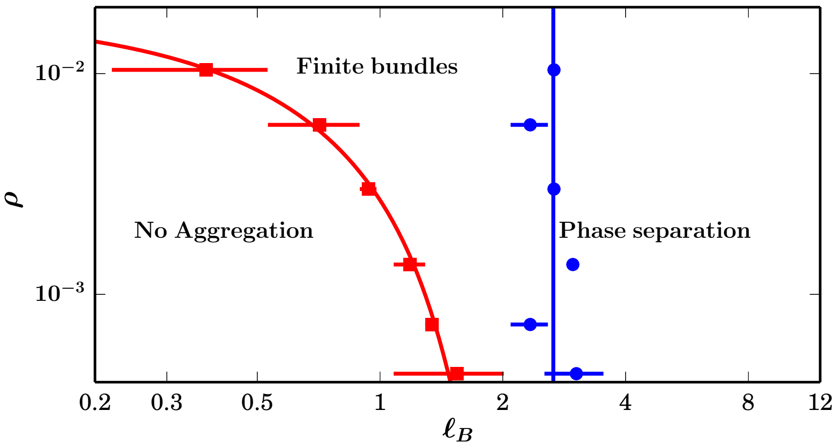

Figure 5.5: Phase diagram in the ρ-ℓ_B plane. There are three phases: one with no aggregation, another one with finite-sized bundles and a completely phase separated state.

bundle phase, albeit for a range of ℓ_B values.

The stability of the phase separated state is checked by doing an additional simulations starting with a system consist of two aggregates, each of having size $m = 50$ and $\ell_B = 8.03$. the snapshot of such a system at different time in Fig. 5.4 is clearly showing that each aggregates merge at large times to form a single aggregate of size 100. Which is a clear indication of stable phase separated state.

The critical values ℓ_{B1} and ℓ_{B2}, which characterize the beginning and end of the finite bundle phase, are expected to depend on the monomer number density ρ since the volume available for a monomer decreases as the density increases and hence the entropy also decreases. To construct the phase diagram in the ρ -ℓ_B plane, we performed extensive simulations for many values of ρ and the results are shown in Fig. 5.5. The approximate transition points are identified by measuring $n(t)$ and we label the region $0.95 < n(t) < 0.02$ as the finite bundle phase. From Fig. 5.5, within numerical error, the transition from the finite bundle phase to the fully phase separated state appears to be independent of the monomer number density for the range of densities considered in our simulations. Which indicate the electrostatic interactions overcomes the entropic contributions, and hence is presumably driven only by electrostatic interactions.

5.3.2 Morphology of aggregates

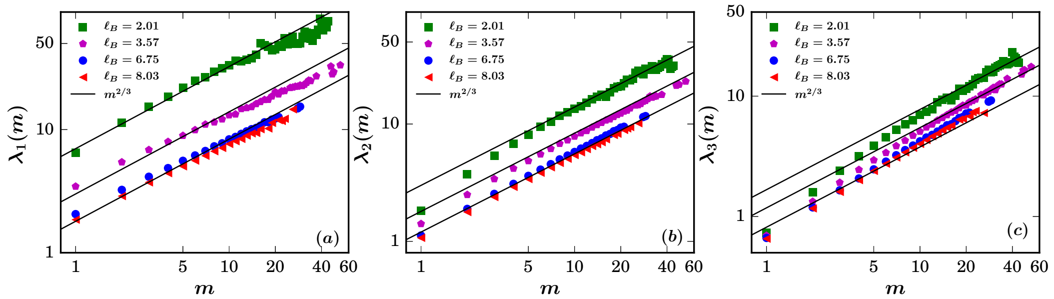

Figure 5.6: The variation of the eigenvalues (a) λ_1, (b) λ_2 and (c) λ_3 of the gyration tensor with aggregate size m for different charge densities ℓ_B.

In our previous work on rigid PE chains described in chapter 4, it was observed that the morphology of the aggregates depended on the charge density ℓ_B of the individual rigid PE chains. For lower values of ℓ_B, the aggregates were cylindrical with length same as that of a single rigid PE chain. In this section, we examine the effect of backbone flexibility on the morphology of the aggregates of FPE chains. The aggregates of FPE chains are compact as may be seen in Fig. 5.2 and we characterize the morphology of the aggregates, of size m, through eigenvalues of the gyration tensor as defined in Eqn. (1.9). $S_{\alpha\beta}(m)$ is the gyration tensor for an aggregate of size m. The three eigenvalues of this tensor, $\lambda_i(m)$, $i = 1, 2, 3$ with $\lambda_1(m) > \lambda_2(m) > \lambda_3(m)$ measure the square of the aggregate dimensions along the three principal axes, and can be used to define parameters that reflect the morphology of the aggregate. The eigenvalues are measured over the trajectory of simulation, accumulating data about aggregates of different sizes and then averaging over the length of the trajectory for each aggregate of size m. In the case of a compact spherical morphology, the radius is proportional to $m^{1/3}$, where m is the size of the aggregate and hence the eigenvalues are expected to scale as $m^{2/3}$. The variation of the eigenvalues $\lambda_i(m)$ with the size of the aggregate, m, for different values of ℓ_B is shown in Fig. 5.6 (a-c) and for all values of ℓ_B shown, $\lambda_i(m)$ is proportional to $m^{2/3}$, as expected for a compact spherical aggregate.

Another measure of morphology of aggregates is prolateness, which characterizes the spheroidness of an object [187], and this can also be defined in terms of the eigenvalues as

$$S(m) = \frac{\prod_{i=1}^{3} \lambda_i(m) - \bar{\lambda}_m}{\bar{\lambda}_m^3}, \tag{5.4}$$

where $\bar{\lambda}_m$ is the average value of eigenvalues $\lambda_1(m), \lambda_2(m)$ and $\lambda_3(m)$ measured for an aggregate of size m. Negative values of $S(m)$ correspond to oblate ellipsoids and positive values to prolate ellipsoids [187]. For a perfect sphere, $S(m) = 0$. We measure the prolateness $S(m)$ by averaging over the length of the trajectory for all aggregates of size m. The dependence of prolateness S on ℓ_B and size of the aggregate m are shown in Fig. 5.7.

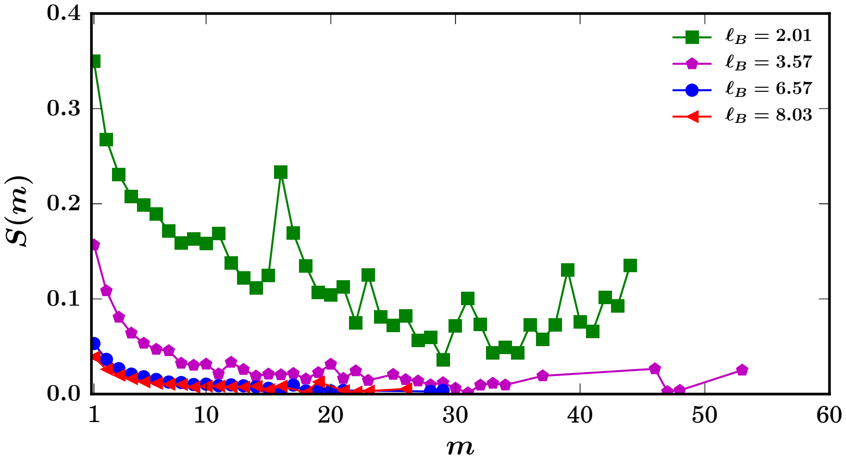

Figure 5.7: The variation of the prolateness S with m for different values of ℓ_B.

It can be seen that for all values of ℓ_B, S is positive and decreases to zero as the size of the aggregate increases. Thus, the shape of the aggregates is prolate for small aggregate sizes and becomes more spherical with increasing aggregate size.

Conformations of individual chains

Next, we probe the conformations of individual FPE chains inside an aggregate in order to understand their role to act as limiting factors in the path to achieve complete phase separation at high values of ℓ_B. Towards this goal, we calculate $R_g^1(m)$, the average radius of gyration of a single PE chain in an aggregate of size m relative to its gyration radius when it is not part of any aggregate, $R_g^1(1)$, as a function of m as well as ℓ_B and the data

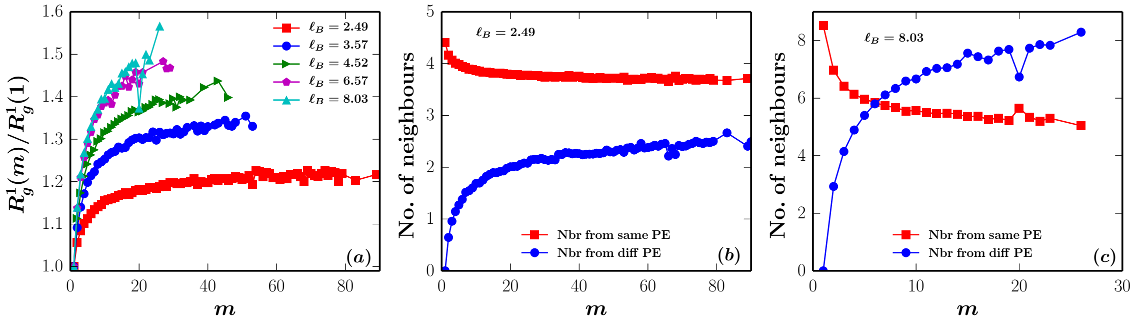

Figure 5.8: (a)Scaled radius of gyration of a single FPE chain belonging to an aggregate of size m, as a function of m for different ℓ_B for the forward simulation. The average number of non-bonded nearest neighbors of a monomer, that belong to same/different FPE chains for (b) $\ell_B = 2.49$ and (c) $\ell_B = 8.03$.

are shown in Fig. 5.8 (a). The gyration radius of a FPE chain increases for all values of ℓ_B, implying that a single FPE chain is in a more extended state in an aggregate. The relative change is larger for higher values of ℓ_B. The implications of such extended states of single FPE chains in aggregates can be the emergence of strong entanglement of individual chains in the aggregate, which can potentially slow down the aggregation dynamics at higher values of ℓ_B as will be discussed in next section. To quantify the entanglement of individual FPE chains in aggregates, we compute the average number of non-bonded nearest neighbors (within a radius of 2σ) for any monomer of a FPE chain and ask whether they belong to the same FPE chain or a different one. In the case of high entanglement (and more extended conformations), we expect that any given monomer will see more neighbors belonging to other chains than its own chain. From data shown in Fig. 5.8 (b) and (c), it is clear that at low values of ℓ_B, an individual FPE chain is more likely to be in a more compact conformation, with any monomer seeing more neighbors belonging to its own chain and even as the size of the aggregate increases, the nature of the nearest neighbors remains the same. However, at high values of ℓ_B, there is a crossover regime, as a function of aggregate size, where any given monomer of an individual FPE chain begins to see more neighbors from other chains than from its own polymer chain. This, when correlated with the data in Fig. 5.8 (a), shows that at high values of ℓ_B, the individual chains are not only in more extended conformation, but are also entangled with other chains.

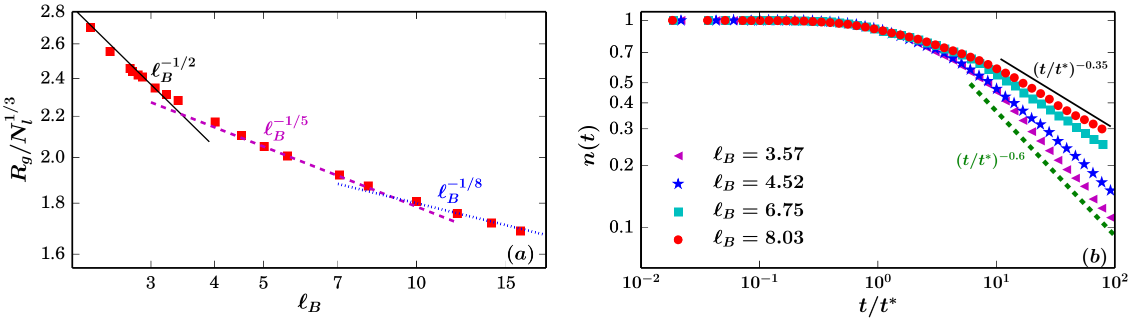

Figure 5.9: (a) The scaling of the gyration radius R_g of largest aggregate with charge density ℓ_B. Each point in the plot is averaged over 2000 frames. N_l is the size of largest aggregate. (b) The variation of fraction of aggregates $n(t)$ with scaled time t/t^* for different values of ℓ_B, where t^* is the time at which $n(t) = 0.9$ for forward simulations. The straight lines are power laws and guides to the eye.

The entanglement of FPE chains in an aggregate suggests that an aggregate of m FPE chains of length N_m can potentially behave like a single FPE chain of size $m \times N_m$. In earlier work described in chapter 3, we showed that the collapsed state of a single FPE chain consists of multiple sub-regimes. These power law sub-regimes are characterized by different scaling relations between R_g and ℓ_B, depending on the most dominant volume interaction virial term in the free energy expression for a collapsed FPE chain with electrostatics described by counterion fluctuation theory. For aggregates of FPE chain with high values of ℓ_B it can be envisaged that the counterions inside the aggregate may not have a preference to a particular FPE chain and may behave collectively as counterions inside a collapsed phase of a single long FPE chain. If this is true, we should be able to observe sub-regimes, similar to that for a single PE chain, as the value of ℓ_B is increased. To check this, we measured $R_g/N^{1/3}$ for the largest aggregate at a particular value of ℓ_B, from our reverse simulations and are shown in Fig. 5.9. For small values of ℓ_B, R_g decreases as $R_g \sim \ell_B^{-1/2}$, while for large values of ℓ_B, R_g decreases as $R_g \sim \ell_B^{-1/5}$, and for even larger values of ℓ_B, the scaling is consistent with $R_g \sim \ell_B^{-1/8}$. These sub-regimes are identical to those obtained in simulations of a single PE chain and as predicted by the counterion fluctuation theory for the effective attractive interactions between monomers of the PE chain. This clearly shows that once, two PE chains aggregate, the aggregate may be treated as a single PE chain of twice the original length.

5.3.3 Dynamics

We now study the pathway to full phase separation (for high values of ℓ_B) starting from an initial condition of completely dispersed PE chains, using forward simulations, as described in Sec. 5.2. Here, we focus on three aspects of the pathway, which have been also studied for rigid PE chains [89–93, 163, 173, 188, 189]. First, the aggregation dynamics are characterized by monitoring the evolution of fraction of aggregates $n(t)$ with time. For rigid PE chains, $n(t)$ decreases as a power law $t^{-\theta}$, showing the absence of a characteristic size of aggregates. Using extensive MD simulations described in chapter 4, we showed that θ is independent of system parameters such as charge density ℓ_B of the rigid PE chains, valency of counterions etc., and has a value $\theta \approx 0.62$, in contrast to $\theta = 1$ obtained in other studies [89,90]. Second aspect is whether the aggregation dynamics can be understood by modeling the system using classical Smoluchowski coagulation equation, which describes irreversible aggregation of particles that are transported by some process, such as diffusion or ballistic motion, and aggregate on contact [23,180]. By modeling the rigid PE chains as neutral, rotating cylinders that diffuse and aggregate on contact, we obtained $\theta = 2/3$, in close agreement with the results from MD simulations ($\theta \approx 0.62$), strongly suggesting that even though the dominant Coulomb interactions in this system of charged PE chains are inherently long-ranged in nature, the effective interactions that drive the aggregation process are short-ranged in nature. The third aspect of the aggregation pathway that is of interest is understanding the mode of merging of two aggregates. Simulations suggest that, at lower values of ℓ_B, two merging rigid PE chains approach each other perpendicularly, followed by a sliding motion of one of the rigid PE chains onto the other in a manner that has been referred to as zipper model [89,90,92,93,163,173,183]. At higher values of ℓ_B, the mode of aggregation of two aggregates changes from a zipper model to

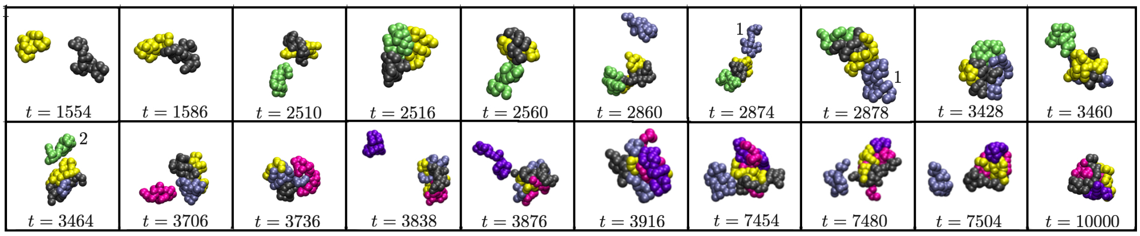

Figure 5.10: Snapshots of aggregation and fragmentation events over a time period for an aggregate of size $m = 4$ for $\ell_B = 3.57$.

a collinear model where the approaching rigid PE chains are parallel to each other and join end to end with larger sliding times, resulting in elongated structures spanning the simulation box. However, irrespective of the mode of aggregation, it was observed that the aggregate size increases monotonically and no fragmentation occurs in the pathway towards a bigger aggregate structure from constituent smaller aggregates. In this section, we examine how the flexibility of the FPE chains affect the three aspects of aggregation dynamics described above.

In case of FPE chains, unlike the case of rigid PE chains, we observe fragmentation events along the pathway of aggregation formation for intermediate values of ℓ_B. Snapshots of a typical aggregation pathway of formation of an aggregate with 4 FPE chains are shown in Fig. 5.10 for $\ell_B = 3.57$. It clearly shows intermittent fragmentation events at $t = 3464$, and 7480, where we identify a fragmentation event as one in which a PE chain that was a long-existing component of an aggregate gets separated. A fragmentation event is usually preceded by the addition of a new FPE chain into the aggregate. For example, in the fragmentation event around $t = 3464$, it can be noticed that the inclusion of a new FPE chain, labeled 1, results in the subsequent expulsion of an already existing FPE chain of the aggregate, labeled 2. We, however, note that the fragmentation events are less frequent as the charge density of the FPE chains increases, possibly due to high attractive electrostatic interactions among the constituent FPE chains in an aggregate, and the higher entanglement between FPE chains as discussed in Sec. 5.3.2.

The aggregation dynamics is characterized by monitoring the temporal evolution of frac-

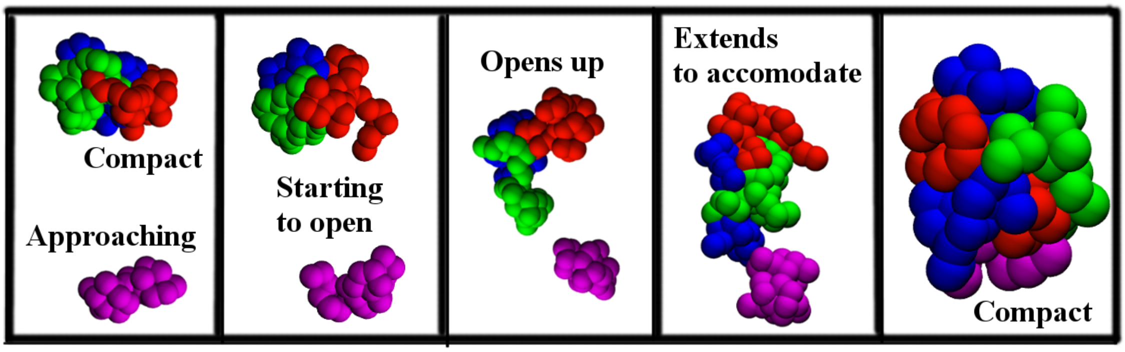

Figure 5.11: Snapshots of aggregation showing the opening up of an existing aggregate to incorporate another PE chain.

tion of aggregates, $n(t)$, which decreases on aggregation and increases with fragmentation and attains a value of $N^{-1} = 0.01$, in the fully phase segregated phase or remains close to 1 in the non-aggregated phase. The variation of $n(t)$ with scaled time t/t^* is shown in Fig. 5.9 (b), where t^* is set to be the time when $n(t) = 0.9$. It can be seen that $n(t)$ decreases with t/t^* as a power law, albeit with varying values of the exponent θ which decrease with the charge density of the FPE chain, in stark contrast to the single exponent ($\theta \approx 0.62$) that we obtained in the aggregation dynamics of rigid PE chains. The exponent θ varies from 0.6 to 0.35 for the range of ℓ_B values considered here.

Smoluchowski theory

We now ask whether the aggregation dynamics of the FPE chains can be modeled by the Smoluchowski equation, which was successfully applied to the case of aggregation of rigid PE chains as explained in chapter 4. It can be seen from Fig. 5.2 and Fig. 5.6, the shape of aggregates, in the case of FPE chains, is spherical and hence $R(m) \propto m^{1/3}$, giving the homogeneity exponent $\lambda = -2/3$ (see Sec. 4.3.3 for more details). Substituting this value of λ for spherical aggregates in Eqn. (4.7), we obtain $\theta = 3/5$. This is in contrast to the value of $\lambda = -1/2$ and $\theta = 2/3$ that we obtained in the case of rigid PE chains in chapter 4, using the kernel for rotating cylindrical aggregates with $R(m) \propto m^{1/2}$.

The result obtained from Smoluchowski theory ($\theta = 3/5$) is close to the numerical value obtained for smaller values of ℓ_B [see lower guide line in Fig. 5.9 (b)]. However, the exponent for larger values of ℓ_B is dependent on ℓ_B and is significantly smaller $\theta = 3/5$ [see upper guide line in Fig. 5.9 (b)] showing a lower aggregation rate with larger ℓ_B. This discrepancy could possibly be due to the existence of kinetic barriers, due to the entanglement of the extended FPE chains in aggregates, that have to be crossed when two aggregates merge. In the case of rigid PE chains, the typical aggregate conformation is linear and a new rigid PE chain gets attached to the existing aggregate without modifying the structure of the previous aggregate. This is not the case for FPE chains, as may be seen from the snapshots of a typical aggregation event shown in Fig. 5.11. In the case of FPE chains, owing to their inherent highly flexible backbones, the aggregates have a more entangled structure and incorporation of a new FPE chain into such an aggregate requires significant global conformational changes, as can be seen in Fig. 5.11. This process can introduce additional time scales into the aggregation dynamics, altering the power law exponent from the result obtained via Smoluchowski theory suggesting that the flexibility of the PE chain backbone can significantly alter the aggregation dynamics as compared to rigid PE chains. It can also be envisaged that these additional time scales become increasingly more significant at higher values of ℓ_B, where the strong electrostatic interactions are the dominant forces holding the aggregate together leading to larger deviations from the classical Smoluchowski theory.

5.4 Discussion

In this chapter we determined, using extensive MD simulations, the effects of backbone flexibility of FPE chains on their aggregation dynamics as well as the equilibrium phases in the presence of trivalent counterions, and contrasted them with the known results for rigid PE chains with rigid backbones. We showed the existence of three possible phases. At low charge densities, the FPE chains do not aggregate and remain uniformly distributed throughout the available volume. At intermediate charge densities, the system exists in a finite bundle phase, where a fraction of the FPE chains form an aggregate while the remaining FPE chains are in the form of multiple small aggregates. At large charge densities, the equilibrium configuration is one of phase separation where all the FPE chains come together as a single aggregate. Surprisingly the critical charge density for the transition from finite bundles to fully phase separated state would appear to be independent, within numerical error, of the monomer number density of the system. We characterized the morphology of the aggregates in detail. Due to the flexibility of the PE chain, the aggregates are compact and their shapes become more spherical with increasing charge density as well as aggregate size. An individual FPE chain within an aggregate becomes more extended with increasing aggregate size, and we show that its non-bonded nearest neighbors are increasingly from other FPE chains, implying that the FPE chains within an aggregate are strongly entangled. Finally, we characterized the dynamics of aggregation in the phase separated state by measuring the power law exponent describing the decreasing in the number of aggregates. Surprisingly, we find this exponent to vary with charge density.

The equilibrium phases of aggregates of PE chains has been a long standing issue, with most of the studies focusing on rigid PE chains [89–93]. Conflicting results from both experimental and theoretical studies suggest that the final equilibrium configuration of an aggregate phase, in the presence of multivalent counterions, could be either a fully phase separated state or coexisting finite aggregates [89–93]. Theoretical studies have also shown that the size of the multivalent counterion, frustration of the interactions between the rods due to growth of the aggregate, as well as kinetic barriers play a role in determining whether finite-sized bundles or complete phase separation are the equilibrium states [188,189]. However, by performing large-scale simulations on systems of 100 rigid PE chains, unlike earlier simulations with fewer PE chains as well as shorter simulation time scales [89,90,92,93], we showed that the equilibrium state is either a fully separated state or one of no aggregation, and could find no evidence of a finite bundle phase [163]. In contrast, for FPE chains, we find that for a large regime of charge density for each value of monomer number density, there exists a finite bundle phase where large aggregates coexist with multiple small aggregates, emphasizing the crucial role played by the flexibility of the polymers. In the fully separated phase, there is always a finite probability of FPE chains fragmenting and forming smaller aggregates. However, we expect that this fraction would be thermodynamically negligible. To show this more rigorously, we would need to systematically simulate larger systems, which is computationally expensive and is beyond the scope of the present study.

The aggregation dynamics of the FPE chains is qualitatively and quantitatively different from that of rigid PE chains. Qualitatively, we find that in the aggregation of FPE chains, we observe fragmentation events where an existing aggregate breaks up into smaller ones. This occurs particularly for charge densities corresponding to finite bundles phase. Such fragmentation events were not observed in the aggregation of rigid PE chains. The aggregation dynamics were quantified through the temporal variation of the fraction of aggregate $n(t)$ in forward simulations: $n(t) \sim t^{-\theta}$. We find that for FPE chains, θ decreases with increasing charge density and varies from from 0.6 and 0.35 for the range of charge densities considered. This is in complete contrast to the charge independent value of $\theta \approx 0.62$ obtained for rigid PE chains through MD simulations. We rationalize the additional time scales that emerge by carefully monitoring a single aggregation event in which a new FPE chain merges with the existing aggregate. To incorporate a new FPE chain into an aggregate, a global reorganization of the existing aggregate is required in the form of adopting an open configuration as the new FPE chain approaches. Once the FPE chain is assimilated into the existing aggregate, another global conformational rearrangement occurs before the new aggregate adopts an almost spherical shape and closed conformation. This opening and closing of the structures can have two possible consequences. If the effective attractive interactions holding the FPE chains in the aggregate are not strong enough, fragmentation events can occur slowing down the aggregation dynamics process. Additionally, at higher charge densities, the opening of the aggregate structures may be difficult due to high attractive energetic barriers introducing additional time scales, issues that do not impact the aggregation of the rigid PE chains. The slowing down of aggregation dynamics at higher values of ℓ_B, for FPE chains, can also be understood in terms of individual conformations of FPE chains in aggregates. We showed that as the value of ℓ_B increases, the individual FPE chains in aggregates are more extended, compared to the case of a single FPE chain, and are also more entangled with other chains resulting in appearance of kinetic barriers in the pathway of forming bigger aggregates. The stronger entanglement at larger values of ℓ_B also explains why fragmentation events occur only at lower values of ℓ_B.

Understanding the effective interactions driving both the collapse of a single PE chain and aggregation of similarly charged PE chains is a long-standing problem of fundamental interest. In particular, the emergence of short-ranged attractive interactions in a system of similarly charged entities with inherently long-ranged Coulomb interactions is an aspect that is not well-understood. Several theories [15–17, 140] have been proposed to explain the nature of the effective interactions based on minimization of free energy of a PE chain. In our earlier work [132, 133], using both extensive MD simulations and analytical calculations, we showed conclusively that the counterion fluctuation theory and its modifications best explains the observed emergence of multiple regimes in the collapse phase of a single PE chain. The data Fig. 5.9 shows the emergence of similar regimes, characterized by different scaling exponents in the relation between radius of gyration and the effective Bjerrum length of the PE chain ($R_g \sim \ell_B^{-\alpha}$) as predicted by counterion fluctuation theory for a single PE chain collapse. This is further evidence for the counterion fluctuation theory being the correct description for the effective attractive interactions in charged PE systems. The results also suggest that at high values of ℓ_B, the multiple FPE chains in an aggregate are strongly entangled and behave effectively like a single long PE chain.

Considering our observation that the aggregates in case of FPE chains are nearly spherical, we model the aggregation of FPE chains using Smoluchowski equation, which for neutral spheres that diffuse and coagulate on contact, gives $\theta = 3/5$ for aggregation dynamics. In the case of FPE chains we obtained a charge dependent value of θ which varied from 0.6 and 0.35. To obtain such a charge dependent θ, it would be necessary to modify the collision kernel to include effects beyond geometry, such as the time scale associated with opening up an aggregate consisting of entangled FPE chains. Quantifying these time scales in a systematic manner is a promising area for future study. We note that modeling the aggregation dynamics of rigid PE chains using Smoluchowski coagulation equation gives $\theta = 2/3$ very close to the numerical obtained value of 0.62, and indicates the lack of rearrangement required to incorporate a new rigid PE chain into an existing aggregate. It may still be possible to understand the different phases in terms of competition between aggregation and fragmentation of neutral aggregates. In simple lattice models of aggregation and fragmentation, an interesting phase transition occurs when fragmentation is limited to a finite number of units fragmenting from an existing aggregate to a neighbor [190–195]. As fragmentation rate is decreased, the system undergoes a non-equilibrium phase transition from a phase characterized by an exponential distribution of aggregate sizes (akin to no aggregation) to a phase characterized by the presence of a condensate containing a finite fraction of the polymers, and the remaining polymers being in smaller aggregates distributed as a power law. In the limit of zero fragmentation, phase separation happens in the form of a single condensate. The phases seen in this work have a one to one mapping with the phases seen in such an aggregation-fragmentation model. However, the mapping is at a qualitative level and understanding the role of charge density in determining the fragmentation rate in systems like charged polymers is an interesting open problem.

Chapter 6

Conclusions

Polyelectrolytes (PEs) are charged polymers. In this thesis, various aspects of highly charged PE systems, both single and multiple chains, are studied using extensive MD simulations. The main results of these simulations are summarized below.

In the first problem, we test the predictions of the different theories describing the collapse transition of a flexible PE using large scale MD simulations. Main results can be summarized as follows:

- We observe two collapsed regime with well defined exponent $\gamma = 1/2$ and $1/5$ (characterizing the dependence of R_g on ℓ_B) in the MD simulation results of good solvent, that we refer to as weak and strong electrostatic regimes. This scaling is robust and independent of the valency of the counterions, volume interaction models between chain monomers and on the solvent models.

- The scaling in the weak electrostatic regime ($\gamma = 1/2$) is not consistent with the predictions of either the fluctuating dipole theory ($\gamma = 2/3$) [17, 18], or of the amorphous ionic solid ($\gamma = 0$) [16], but agrees with the counterion fluctuation theory [15] proposed earlier. However, the scaling in the strong electrostatic regime ($\gamma = 1/5$) is not consistent with any of the existing theories.

- We find the existence of several sub-regimes in the dependence of the gyration radius of the chain R_g on ℓ_B for poor solvents, the exponent γ for a poor solvent crucially depends on the size and valency of the counterions.

- We develop a generalized theory for a collapsed regime of a PE in good and poor solvents based on counterion fluctuation theory [15], by explicitly considering the monomer-monomer, monomer-counterion and counterion-counterion interactions.

- We also show that the presence of condensed counterions modifies the effective attraction among the chain monomers and modulates the sign of the second virial coefficient under poor solvent conditions.

In the second problem, we study the aggregation dynamics of rigid PEs using large scale molecular dynamics simulations. The main results are summarized below

- We show that the number of aggregates decrease with time as power laws with exponents that are, within numerical uncertainty, independent of the charge density of the polymers, valency of the counterions, density, and length of the PE chain.

- We find that the morphology of the aggregates depends on the value of the charge density of the polymers. For moderate values of charge density, the shape of the aggregates is cylindrical with height equal to the length of a single PE chain. However, for larger values of charge density, the linear extent of the aggregates increases as more and more PEs aggregate.

- We model the aggregation dynamics using the Smoluchowski coagulation equation with kernels determined from the molecular dynamics simulations and justify the numerically obtained value of the exponent.

- Our results suggest that once counterions condense, effective interactions between PE chains are short-ranged and the aggregation of PEs are diffusion-limited.

In the last problem, we study the behavior of aggregation in the case of completely flexible PEs (FPEs). The main results are summarized below.

- In the case of FPEs, aggregation as well as fragmentation events are present.
- Unlike rigid PEs, the phase diagram of the FPEs with valency $Z = 3$, consist of three different phases depending on the charge density: one with no aggregation, another with finite bundles and a fully phase separated phase.
- An individual FPE chain within an aggregate becomes more extended with increasing aggregate size, and we show that its non-bonded nearest neighbors are increasingly from other FPE chains, implying that the FPE chains within an aggregate are strongly entangled.
- In contrast to rigid PEs aggregation, the dynamics of aggregation in the phase-separated regime depends on charge density. The reason for the dependence of the exponent on charge may be due to the additional time scale involved in the system due to the rearrangements inside an aggregate such as opening up and closing up of an existing aggregate consisting of entangled FPE chains, during the addition of a new one. Such a rearrangement is absent in the case of rigid PE aggregation.
- In the case of FPE aggregate, we observe multiple regimes characterized by different scaling exponents in the relation between the radius of gyration and the effective Bjerrum length of the PE chain ($R_g \sim \ell_B^{-\gamma}$) as predicted by generalized counterion fluctuation theory for a single PE chain collapse. This provides further evidence for the counterion fluctuation theory being the correct description for the effective attractive interactions in PE systems.

Bibliography

[1] Paul van der Schoot and Robijn Bruinsma. Electrostatics and the assembly of an rna virus. *Physical Review E*, 71(6):061928, 2005.

[2] Victor A Bloomfield. Condensation of dna by multivalent cations: considerations on mechanism. *Biopolymers: Original Research on Biomolecules*, 31(13):1471, 1991.

[3] Victor A Bloomfield. Dna condensation. *Current opinion in structural biology*, 6(3):334, 1996.

[4] David A Mortimer. Synthetic polyelectrolytes - a review. *Polymer International*, 25(1):29, 1991.

[5] Margreet A Wolfert, Etienne H Schacht, Veska Toncheva, Karel Ulbrich, Ola Nazarova, and Leonard W Seymour. Characterization of vectors for gene therapy formed by self-assembly of dna with synthetic block co-polymers. *Human gene therapy*, 7(17):2123, 1996.

[6] Y Kawashima, T Handa, A Kasai, H Takenaka, SY Lin, and Y Ando. Novel method for the preparation of controlled-release theophylline granules coated with a polyelectrolyte complex of sodium polyphosphate–chitosan. *Journal of pharmaceutical sciences*, 74(3):264–268, 1985.

[7] Brian Bolto and John Gregory. Organic polyelectrolytes in water treatment. *Water research*, 41(11):2301, 2007.

[8] Seong Uk Hong, Matthew D Miller, and Merlin L Bruening. Removal of dyes, sugars, and amino acids from nacl solutions using multilayer polyelectrolyte nanofiltration membranes. *Industrial & engineering chemistry research*, 45(18):6284, 2006.

[9] Gerald S Manning. Polyelectrolytes. *Annual review of physical chemistry*, 23(1):117, 1972.

[10] Mark J Stevens and Kurt Kremer. The nature of flexible linear polyelectrolytes in salt free solution: A molecular dynamics study. *The Journal of chemical physics*, 103(4):1669, 1995.

[11] Mark J Stevens and Kurt Kremer. Structure of salt-free linear polyelectrolytes. *Physical Review Letters*, 71(14):2228, 1993.

[12] Roland G Winkler, Michael Gold, and Peter Reineker. Collapse of polyelectrolyte macromolecules by counterion condensation and ion pair formation: a molecular dynamics simulation study. *Physical Review Letters*, 80(17):3731, 1998.

[13] Sergey M Mel'nikov, Malek O Khan, Björn Lindman, and Bo Jönsson. Phase behavior of single dna in mixed solvents. *Journal of the American Chemical Society*, 121(6):1130–1136, 1999.

[14] Anoop Varghese, Satyavani Vemparala, and R Rajesh. Phase transitions of a single polyelectrolyte in a poor solvent with explicit counterions. *The Journal of chemical physics*, 135(15):154902, 2011.

[15] NV Brilliantov, DV Kuznetsov, and R Klein. Chain collapse and counterion condensation in dilute polyelectrolyte solutions. *Physical Review Letters*, 81(7):1433, 1998.

[16] Francisco J Solis and Monica Olvera De La Cruz. Collapse of flexible polyelectrolytes in multivalent salt solutions. *The Journal of Chemical Physics*, 112(4):2030, 2000.

[17] H Schiessel and P Pincus. Counterion-condensation-induced collapse of highly charged polyelectrolytes. *Macromolecules*, 31(22):7953, 1998.

[18] M Muthukumar. Theory of counter-ion condensation on flexible polyelectrolytes: adsorption mechanism. *The Journal of chemical physics*, 120(19):9343, 2004.

[19] Gerard CL Wong and Lois Pollack. Electrostatics of strongly charged biological polymers: ion-mediated interactions and self-organization in nucleic acids and proteins. *Annual review of physical chemistry*, 61:171, 2010.

[20] Olivier JN Bertrand, Deborah Kuchnir Fygenson, and Omar A Saleh. Active, motor-driven mechanics in a dna gel. *Proceedings of the National Academy of Sciences*, 2012.

[21] Daniel A Fletcher and R Dyche Mullins. Cell mechanics and the cytoskeleton. *Nature*, 463(7280):485, 2010.

[22] Jonathan Stricker, Tobias Falzone, and Margaret L Gardel. Mechanics of the f-actin cytoskeleton. *Journal of biomechanics*, 43(1):9, 2010.

[23] François Leyvraz. Scaling theory and exactly solved models in the kinetics of irreversible aggregation. *Physics Reports*, 383(2):95, 2003.

[24] Pascal Carrivain, Axel Cournac, Christophe Lavelle, Annick Lesne, Julien Mozziconacci, Fabien Paillusson, Laurence Signon, Jean-Marc Victor, and Maria Barbi. Electrostatics of dna compaction in viruses, bacteria and eukaryotes: functional insights and evolutionary perspective. *Soft Matter*, 8(36):9285, 2012.

[25] Bruce Alberts, Dennis Bray, Karen Hopkin, Alexander D Johnson, Julian Lewis, Martin Raff, Keith Roberts, and Peter Walter. *Essential cell biology*. Garland Science, 2015.

[26] Helmut Schiessel. The physics of chromatin. *Journal of Physics: Condensed Matter*, 15(19):R699, 2003.

[27] John Goers, Amy B Manning-Bog, Alison L McCormack, Ian S Millett, Sebastian Doniach, Donato A Di Monte, Vladimir N Uversky, and Anthony L Fink. Nuclear localization of α-synuclein and its interaction with histones. *Biochemistry*, 42(28):8465, 2003.

[28] Giorgio Favrin, Anders Irbäck, and Sandipan Mohanty. Oligomerization of amyloid $A\beta_{16-22}$ peptides using hydrogen bonds and hydrophobicity forces. *Biophysical journal*, 87(6):3657, 2004.

[29] Yun-Jie Yang, Xia Tao, Qian Hou, Yi Ma, Xuan-Li Chen, and Jian-Feng Chen. Mesoporous silica nanotubes coated with multilayered polyelectrolytes for ph-controlled drug release. *Acta Biomaterialia*, 6(8):3092, 2010.

[30] Daniel J Schmidt, Joshua S Moskowitz, and Paula T Hammond. Electrically triggered release of a small molecule drug from a polyelectrolyte multilayer coating. *Chemistry of Materials*, 22(23):6416, 2010.

[31] Michael C Berg, Lei Zhai, Robert E Cohen, and Michael F Rubner. Controlled drug release from porous polyelectrolyte multilayers. *Biomacromolecules*, 7(1):357, 2006.

[32] Whitney C Blocher and Sarah L Perry. Complex coacervate-based materials for biomedicine. *Wiley Interdisciplinary Reviews: Nanomedicine and Nanobiotechnology*, 9(4):e1442, 2016.

[33] Shutao Guo, Yuanyu Huang, Qiao Jiang, Yun Sun, Liandong Deng, Zicai Liang, Quan Du, Jinfeng Xing, Yuliang Zhao, Paul C Wang, et al. Enhanced gene delivery and sirna silencing by gold nanoparticles coated with charge-reversal polyelectrolyte. *ACS nano*, 4(9):5505, 2010.

[34] Sania Mansouri, Yan Cuie, Francoise Winnik, Qin Shi, Patrick Lavigne, Mohamed Benderdour, Eric Beaumont, and Julio C Fernandes. Characterization of folate-chitosan-dna nanoparticles for gene therapy. *Biomaterials*, 27(9):2060, 2006.

[35] Mark A Shannon, Paul W Bohn, Menachem Elimelech, John G Georgiadis, Benito J Marinas, and Anne M Mayes. Science and technology for water purification in the coming decades. In *Nanoscience And Technology: A Collection of Reviews from Nature Journals*, page 337. World Scientific, 2010.

[36] Susumu Kawamura. Effectiveness of natural polyelectrolytes in water treatment. *Journal-American Water Works Association*, 83(10):88, 1991.

[37] Bijay P Tripathi, Nidhi C Dubey, and M Stamm. Functional polyelectrolyte multilayer membranes for water purification applications. *Journal of hazardous materials*, 252:401, 2013.

[38] UK Aravind, B George, MS Baburaj, S Thomas, AP Thomas, and CT Aravindakumar. Treatment of industrial effluents using polyelectrolyte membranes. *Desalination*, 252(1):27, 2010.

[39] Manian Ramesh, Chandrashekar S Shetty, and Martha R Finck. Hydrophobic polyelectrolytes used in color removal, March 8 1994. US Patent 5,292,793.

[40] GR Nabi Bidhendi, A Torabian, H Ehsani, and N Razmkhah. Evaluation of industrial dyeing wastewater treatment with coagulants and polyelectrolyte as a coagulant aid. *Iran. J. Environ. Health. Sci. Eng*, 4(1):29, 2007.

[41] Lars Wågberg, Sven Forsberg, A Johansson, and P Juntti. Engineering of fibre surface properties by application of the polyelectrolyte multilayer concept. part i: Modification of paper strength. *Journal of Pulp and Paper Science (JPPS)*, 28(7):222, 2002.

[42] James Richard Gross. Absorbent articles made from latexes of carboxylic synthetic polyelectrolyte containing n-substituted acrylamide crosslinking agent, March 14 1978. US Patent 4,079,029.

[43] Mauricio Odio and Sheila Fallon Friedlander. Diaper dermatitis and advances in diaper technology. *Current opinion in pediatrics*, 12(4):342, 2000.

[44] James A Ward. Polyelectrolyte hydrogels and methods of their preparation, March 11 1980. US Patent 4,192,727.

[45] Ronald S Harland and Robert K Prud'homme. *Polyelectrolyte gels: Properties, preparation, and applications*. ACS Publications, 1992.

[46] Gerald S Manning. Limiting laws and counterion condensation in polyelectrolyte solutions i. colligative properties. *The journal of chemical Physics*, 51(3):924, 1969.

[47] Jovan Kamcev, Michele Galizia, Francesco M Benedetti, Eui-Soung Jang, Donald R Paul, Benny D Freeman, and Gerald S Manning. Partitioning of mobile ions between ion exchange polymers and aqueous salt solutions: importance of counter-ion condensation. *Physical Chemistry Chemical Physics*, 18(8):6021, 2016.

[48] IM Lifshitz, A Yu Grosberg, and AR Khokhlov. Some problems of the statistical physics of polymer chains with volume interaction. *Reviews of Modern Physics*, 50(3):683, 1978.

[49] Gerald S Manning. Limiting laws and counterion condensation in polyelectrolyte solutions. iii. an analysis based on the mayer ionic solution theory. *The Journal of Chemical Physics*, 51(8):3249, 1969.

[50] Gerald S Manning. Counterion condensation theory constructed from different models. *Physica A: Statistical Mechanics and its Applications*, 231(1):236, 1996.

[51] Fumio Oosawa. Polyelectrolytes. In *Polyelectrolytes*. Marcel Dekker, 1971.

[52] Camilo Guáqueta. Phase transitions in polyelectrolyte solutions. 2005.

[53] Murugappan Muthukumar. *Polymer translocation*. CRC Press, 2016.

[54] A. Yu. Grosberg and A. R. Khokhlov. *Statistical Physics of Macromolecules*. AIP Press, Woodbury, NY, 1994.

[55] Paul J Flory. *Principles of polymer chemistry*. Cornell University Press, 1953.

[56] W Kuhn, O Künzle, and A Katchalsky. Verhalten polyvalenter fadenmolekelionen in lösung. *Helvetica Chimica Acta*, 31(7):1994, 1948.

[57] Andrey V Dobrynin and Michael Rubinstein. Theory of polyelectrolytes in solutions and at surfaces. *Progress in Polymer Science*, 30(11):1049, 2005.

[58] Max Born and Robert Oppenheimer. Zur quantentheorie der molekeln. *Annalen der Physik*, 389(20):457, 1927.

[59] Victor Rühle, Christoph Junghans, Alexander Lukyanov, Kurt Kremer, and Denis Andrienko. Versatile object-oriented toolkit for coarse-graining applications. *Journal of Chemical Theory and Computation*, 5(12):3211, 2009.

[60] Hsiao-Ping Hsu. Lattice monte carlo simulations of polymer melts. *The Journal of chemical physics*, 141(23):234901, 2014.

[61] Peter H Verdier and David E Kranbuehl. Simulation of polymer chain dynamics by lattice models with excluded volume: Lattice dependence. *Macromolecules*, 20(6):1362, 1987.

[62] J Baschnagel, K Binder, W Paul, M Laso, UW Suter, I Batoulis, W Jilge, and T Bürger. On the construction of coarse-grained models for linear flexible polymer chains: Distribution functions for groups of consecutive monomers. *The Journal of chemical physics*, 95(8):6014, 1991.

[63] Wolfgang Paul, Kurt Binder, Kurt Kremer, and Dieter W Heermann. Structure-property correlation of polymers, a monte carlo approach. *Macromolecules*, 24(23):6332, 1991.

[64] I Carmesin and Kurt Kremer. The bond fluctuation method: a new effective algorithm for the dynamics of polymers in all spatial dimensions. *Macromolecules*, 21(9):2819, 1988.

[65] Markus Deserno and Christian Holm. Theory and simulations of rigid polyelectrolytes. *Molecular Physics*, 100(18):2941, 2002.

[66] AA Gavrilov, AV Chertovich, and E Yu Kramarenko. Conformational behavior of a single polyelectrolyte chain with bulky counterions. *Macromolecules*, 49(3):1103, 2016.

[67] AA Gavrilov, AV Chertovich, and E Yu Kramarenko. Dissipative particle dynamics for systems with high density of charges: Implementation of electrostatic interactions. *The Journal of chemical physics*, 145(17):174101, 2016.

[68] Anette Schneemann. The structural and functional role of rna in icosahedral virus assembly. *Annual Review of Microbiology*, 60:51, 2006.

[69] Antonio Šiber, Anže Lošdorfer Božič, and Rudolf Podgornik. Energies and pressures in viruses: contribution of nonspecific electrostatic interactions. *Physical chemistry chemical physics*, 14(11):3746, 2012.

[70] Robijn F Bruinsma, Mauricio Comas-Garcia, Rees F Garmann, and Alexander Y Grosberg. Equilibrium self-assembly of small rna viruses. *Physical Review E*, 93(3):032405, 2016.

[71] Leonard C Gosule and John A Schellman. Compact form of dna induced by spermidine. *Nature*, 259(5541):333, 1976.

[72] Izumi Nishio, Shao-Tang Sun, Gerald Swislow, and Toyoichi Tanaka. First observation of the coil–globule transition in a single polymer chain. *Nature*, 281(5728):208, 1979.

[73] Arindam Kundagrami and M Muthukumar. Effective charge and coil- globule transition of a polyelectrolyte chain. *Macromolecules*, 43(5):2574, 2010.

[74] Jiayi Guo, Haojun Liang, and Zhen-Gang Wang. Coil-to-globule transition by dissipative particle dynamics simulation. *The Journal of chemical physics*, 134(24):244904, 2011.

[75] Pierre-Gilles De Gennes and Pierre-Gilles Gennes. *Scaling concepts in polymer physics*. Cornell university press, 1979.

[76] Cameron F Abrams, N-K Lee, and SP Obukhov. Collapse dynamics of a polymer chain: Theory and simulation. *Europhysics Letters*, 59(3):391, 2002.

[77] A Halperin and Paul M Goldbart. Early stages of homopolymer collapse. *Physical Review E*, 61(1):565, 2000.

[78] Daniel J Needleman, Miguel A Ojeda-Lopez, Uri Raviv, Herbert P Miller, Leslie Wilson, and Cyrus R Safinya. Higher-order assembly of microtubules by counte-

rions: from hexagonal bundles to living necklaces. *Proceedings of the National Academy of Sciences*, 101(46):16099, 2004.

[79] Mireille Maria Anna Elisabeth Claessens, C Semmrich, L Ramos, and AR Bausch. Helical twist controls the thickness of f-actin bundles. *Proceedings of the National Academy of Sciences*, 105(26):8819, 2008.

[80] Florian Huber, Dan Strehle, and Josef Käs. Counterion-induced formation of regular actin bundle networks. *Soft Matter*, 8(4):931, 2012.

[81] Sarah Mohammadinejad, Ramin Golestanian, and Hossein Fazli. Chiral structure of f-actin bundle formed by multivalent counterions. *Soft Matter*, 8(13):3649, 2012.

[82] Thomas E Angelini, Hongjun Liang, Willy Wriggers, and Gerard CL Wong. Like-charge attraction between polyelectrolytes induced by counterion charge density waves. *Proceedings of the National Academy of Sciences*, 100(15):8634, 2003.

[83] Xiangyun Qiu, Lisa W Kwok, Hye Yoon Park, Jessica S Lamb, Kurt Andresen, and Lois Pollack. Measuring inter-dna potentials in solution. *Physical Review Letters*, 96(13):138101, 2006.

[84] Kurt Andresen, Xiangyun Qiu, Suzette A Pabit, Jessica S Lamb, Hye Yoon Park, Lisa W Kwok, and Lois Pollack. Mono-and trivalent ions around dna: a small-angle scattering study of competition and interactions. *Biophysical journal*, 95(1):287, 2008.

[85] Thomas E Angelini, Ramin Golestanian, Robert H Coridan, John C Butler, Alexandre Beraud, Michael Krisch, Harald Sinn, Kenneth S Schweizer, and Gerard CL Wong. Counterions between charged polymers exhibit liquid-like organization and dynamics. *Proceedings of the National Academy of Sciences*, 103(21):7962, 2006.

[86] Anthony L Fink. Protein aggregation: folding aggregates, inclusion bodies and amyloid. *Folding and design*, 3(1):R9, 1998.

[87] Alfonso De Simone, Craig Kitchen, Ann H Kwan, Margaret Sunde, Christopher M Dobson, and Daan Frenkel. Intrinsic disorder modulates protein self-assembly and aggregation. *Proceedings of the National Academy of Sciences*, 109(18):6951, 2012.

[88] Gerard CL Wong. Electrostatics of rigid polyelectrolytes. *Current opinion in colloid & interface science*, 11(6):310, 2006.

[89] Hossein Fazli, Sarah Mohammadinejad, and Ramin Golestanian. Salt-induced aggregation of stiff polyelectrolytes. *Journal of Physics: Condensed Matter*, 21(42):424111, 2009.

[90] Hossein Fazli and Ramin Golestanian. Aggregation kinetics of stiff polyelectrolytes in the presence of multivalent salt. *Physical Review E*, 76(4):041801, 2007.

[91] Alexey Savelyev and Garegin A Papoian. Inter-dna electrostatics from explicit solvent molecular dynamics simulations. *Journal of the American Chemical Society*, 129(19):6060, 2007.

[92] Mehmet Sayar and Christian Holm. Finite-size polyelectrolyte bundles at thermodynamic equilibrium. *Europhysics Letters*, 77(1):16001, 2006.

[93] Mehmet Sayar and Christian Holm. Equilibrium polyelectrolyte bundles with different multivalent counterion concentrations. *Physical Review E*, 82(3):031901, 2010.

[94] MJ Stevens. Mj stevens, physical review letters 82, 101 (1999). *Physical Review Letters*, 82:101, 1999.

[95] Kun-Chun Lee, Itamar Borukhov, William M Gelbart, Andrea J Liu, and Mark J Stevens. Effect of mono-and multivalent salts on angle-dependent attractions between charged rods. *Physical Review Letters*, 93(12):128101, 2004.

[96] Simone Pietronave, Luca Arcesi, Cristina D?Arrigo, and Angelo Perico. Attraction between like-charged polyelectrolytes in the extended condensation theory. *The Journal of Physical Chemistry B*, 112(50):15991, 2008.

[97] Niels Grønbech-Jensen, Robert J Mashl, Robijn F Bruinsma, and William M Gelbart. Counterion-induced attraction between rigid polyelectrolytes. *Physical Review Letters*, 78(12):2477, 1997.

[98] Binquan Luan and Aleksei Aksimentiev. Dna attraction in monovalent and divalent electrolytes. *Journal of the American Chemical Society*, 130(47):15754, 2008.

[99] R Bruinsma. Liquid crystals of polyelectrolyte networks. *Physical Review E*, 63(6):061705, 2001.

[100] Alexandre Diehl, Humberto A Carmona, and Yan Levin. Counterion correlations and attraction between like-charged macromolecules. *Physical Review E*, 64(1):011804, 2001.

[101] Jay X Tang, Shuen Wong, Phong T Tran, and Paul A Janmey. Counterion induced bundle formation of rodlike polyelectrolytes. *Berichte der Bunsengesellschaft für physikalische Chemie*, 100(6):796, 1996.

[102] Marián Sedlák and Eric J Amis. Dynamics of moderately concentrated salt-free polyelectrolyte solutions: Molecular weight dependence. *The Journal of chemical physics*, 96(1):817, 1992.

[103] JJ Tanahatoe and ME Kuil. Polyelectrolyte aggregates in solutions of sodium poly (styrenesulfonate). *The Journal of Physical Chemistry B*, 101(31):5905, 1997.

[104] Redouane Borsali, Huy Nguyen, and R Pecora. Small-angle neutron scattering and dynamic light scattering from a polyelectrolyte solution: Dna. *Macromolecules*, 31(5):1548, 1998.

[105] Olena V Zribi, Hee Kyung, Ramin Golestanian, Tanniemola B Liverpool, and Gerard CL Wong. Condensation of dna-actin polyelectrolyte mixtures driven by ions of different valences. *Physical Review E*, 73(3):031911, 2006.

[106] John C Butler, Thomas Angelini, Jay X Tang, and Gerard CL Wong. Ion multivalence and like-charge polyelectrolyte attraction. *Physical Review Letters*, 91(2):028301, 2003.

[107] F Bordi, C Cametti, M Diociaiuti, and S Sennato. Large equilibrium clusters in low-density aqueous suspensions of polyelectrolyte-liposome complexes: a phenomenological model. *Physical Review E*, 71(5):050401, 2005.

[108] Andras Muhlrad, Elena E Grintsevich, and Emil Reisler. Polycation induced actin bundles. *Biophysical chemistry*, 155(1):45, 2011.

[109] Ningdong Huang, Jiaojiao Tao, Jun Liu, Shenghui Wei, Liangbin Li, and Ziyu Wu. Specific ion effects induced by mono-valent salts in like charged aggregates in water. *Soft matter*, 10(24):4236, 2014.

[110] Jolly Ray and Gerald S Manning. Formation of loose clusters in polyelectrolyte solutions. *Macromolecules*, 33(8):2901, 2000.

[111] Shiqi Zhou. Density functional analysis of like-charged attraction between two similarly charged cylinder polyelectrolytes. *Langmuir*, 29(40):12490, 2013.

[112] AV Ermoshkin and M Olvera De La Cruz. Polyelectrolytes in the presence of multivalent ions: gelation versus segregation. *Physical Review Letters*, 90(12):125504, 2003.

[113] CP Broedersz and FC MacKintosh. Erratum: Modeling semiflexible polymer networks. *Reviews of Modern Physics*, 88(3):039903, 2016.

[114] Angelo Perico and Arnaldo Rapallo. Clusters in strong polyelectrolyte solutions in the condensation theory approach. *The Journal of chemical physics*, 134(5):02B609, 2011.

[115] GS Manning. Counterion condensation theory of attraction between like charges in the absence of multivalent counterions. *The European Physical Journal E*, 34(12):132, 2011.

[116] Arun Yethiraj. Conformational properties and static structure factor of polyelectrolyte solutions. *Physical Review Letters*, 78(19):3789, 1997.

[117] Arun Yethiraj. Liquid state theory of polyelectrolyte solutions. *The Journal of Physical Chemistry B*, 113(6):1539, 2009.

[118] Gerald S Manning. Excess counterion condensation on polyelectrolyte kinks and branch points and the interaction of skewed charged lines. *Soft matter*, 10(21):3738, 2014.

[119] Dezső Boda and Douglas Henderson. The effects of deviations from lorentz–berthelot rules on the properties of a simple mixture. *Molecular Physics*, 106(20):2367, 2008.

[120] Loup Verlet. Computer "experiments" on classical fluids. i. thermodynamical properties of lennard-jones molecules. *Physical review*, 159(1):98, 1967.

[121] William C Swope, Hans C Andersen, Peter H Berens, and Kent R Wilson. A computer simulation method for the calculation of equilibrium constants for the formation of physical clusters of molecules: Application to small water clusters. *The Journal of Chemical Physics*, 76(1):637, 1982.

[122] Michael P Allen and Dominic J Tildesley. *Computer simulation of liquids*. Oxford university press, 2017.

[123] Paul P Ewald. The calculation of optical and electrostatic grid potentials. *Annalen der physik*, 369(3):253, 1921.

[124] Daan Frenkel and Berend Smit. *Understanding molecular simulation: from algorithms to applications*, volume 1. Elsevier, 2001.

[125] Thierry Dauxois, Stefano Ruffo, Ennio Arimondo, and Martin Wilkens. Dynamics and thermodynamics of systems with long-range interactions: An introduction. In *Dynamics and Thermodynamics of Systems with Long-Range Interactions*, page 1. Springer, 2002.

[126] Freddy Bouchet, Shamik Gupta, and David Mukamel. Thermodynamics and dynamics of systems with long-range interactions. *Physica A: Statistical Mechanics and its Applications*, 389(20):4389, 2010.

[127] Alessandro Campa, Thierry Dauxois, and Stefano Ruffo. Statistical mechanics and dynamics of solvable models with long-range interactions. *Physics Reports*, 480(3):57, 2009.

[128] Hans C Andersen. Molecular dynamics simulations at constant pressure and/or temperature. *The Journal of chemical physics*, 72(4):2384, 1980.

[129] Herman JC Berendsen, JPM van Postma, Wilfred F van Gunsteren, ARHJ DiNola, and JR Haak. Molecular dynamics with coupling to an external bath. *The Journal of chemical physics*, 81(8):3684, 1984.

[130] Shuichi Nosé. A unified formulation of the constant temperature molecular dynamics methods. *The Journal of chemical physics*, 81(1):511, 1984.

[131] William G Hoover. Canonical dynamics: equilibrium phase-space distributions. *Physical review A*, 31(3):1695, 1985.

[132] Anvy Moly Tom, Satyavani Vemparala, R Rajesh, and Nikolai V Brilliantov. Mechanism of chain collapse of strongly charged polyelectrolytes. *Physical Review Letters*, 117(14):147801, 2016.

[133] Anvy Moly Tom, Satyavani Vemparala, R Rajesh, and Nikolai V Brilliantov. Regimes of electrostatic collapse of a highly charged polyelectrolyte in a poor solvent. *Soft matter*, 13(9):1862, 2017.

[134] Allan Rupprecht, Jure Piškur, Johan Schultz, Lars Nordenskiöld, Zhiyan Song, and Gojmir Lahajnar. Mechanochemical study of conformational transitions and melting of li-, na-, k-, and csdna fibers in ethanol–water solutions. *Biopolymers: Original Research on Biomolecules*, 34(7):897, 1994.

[135] EI Tiktopulo, VE Bychkova, J Ricka, and OB Ptitsyn. Cooperativity of the coil-globule transition in a homopolymer: Microcalorimetric study of poly (n-isopropylacrylamide). *Macromolecules*, 27(10):2879, 1994.

[136] Thomas E Creighton. *Protein folding*. WH Freeman and Company, 1992.

[137] Hue Sun Chan and Ken A Dill. The protein folding problem. *Physics today*, 46(2):24, 1993.

[138] Eilon Sherman and Gilad Haran. Coil–globule transition in the denatured state of a small protein. *Proceedings of the National Academy of Sciences*, 103(31):11539, 2006.

[139] AR Khokhlov. On the collapse of weakly charged polyelectrolytes. *Journal of Physics A: Mathematical and General*, 13(3):979, 1980.

[140] Ramin Golestanian, Mehran Kardar, and Tanniemola B Liverpool. Collapse of stiff polyelectrolytes due to counterion fluctuations. *Physical Review Letters*, 82(22):4456, 1999.

[141] AG Cherstvy. Collapse of highly charged polyelectrolytes triggered by attractive dipole- dipole and correlation-induced electrostatic interactions. *The Journal of Physical Chemistry B*, 114(16):5241, 2010.

[142] Prasanta Kundu and Arti Dua. Weak polyelectrolytes in the presence of counterion condensation with ions of variable size and polarizability. *Journal of Statistical Mechanics: Theory and Experiment*, 2014(7):P07023, 2014.

[143] Steve Plimpton. Fast parallel algorithms for short-range molecular dynamics. *Journal of computational physics*, 117(1):1, 1995.

[144] Helena Kovacs and Aatto Laaksonen. Molecular dynamics simulation and nmr study of water-acetonitrile mixtures. *Journal of the American Chemical Society*, 113(15):5596, 1991.

[145] A Yu Grosberg and DV Kuznetsov. Quantitative theory of the globule-to-coil transition. 1. link density distribution in a globule and its radius of gyration. *Macromolecules*, 25(7):1970, 1992.

[146] Vladimir A Baulin and Emmanuel Trizac. Self-assembly of spherical interpolyelectrolyte complexes from oppositely charged polymers. *Soft Matter*, 8(25):6755–6766, 2012.

[147] Vassilis I Harismiadis, Athanassios Z Panagiotopoulos, and Dimitrios P Tassios. Phase equilibria of binary lennard-jones mixtures with cubic equations of state. *Fluid Phase Equilibria*, 94:1, 1994.

[148] CA Croxton and David Chandler. Liquid state physics—a statistical mechanical introduction. *Physics Today*, 28:52, 1975.

[149] Jean-Pierre Hansen and Ian Ranald McDonald. *Theory of simple liquids: with applications to soft matter*. Academic Press, 2013.

[150] Rakwoo Chang and Arun Yethiraj. Strongly charged flexible polyelectrolytes in poor solvents: molecular dynamics simulations with explicit solvent. *The Journal of chemical physics*, 118(14):6634, 2003.

[151] Uwe Micka, Christian Holm, and Kurt Kremer. Strongly charged, flexible polyelectrolytes in poor solvents: molecular dynamics simulations. *Langmuir*, 15(12):4033, 1999.

[152] Uwe Micka and Kurt Kremer. Strongly charged flexible polyelectrolytes in poor solvents?from stable spheres to necklace chains. *Europhysics Letters*, 49(2):189, 2000.

[153] Namkyung Lee and D Thirumalai. Dynamics of collapse of flexible polyelectrolytes in poor solvents. *Macromolecules*, 34(10):3446, 2001.

[154] Rakwoo Chang and Arun Yethiraj. Dilute solutions of strongly charged flexible polyelectrolytes in poor solvents: Molecular dynamics simulations with explicit solvent. *Macromolecules*, 39(2):821, 2006.

[155] Hans Jörg Limbach and Christian Holm. Single-chain properties of polyelectrolytes in poor solvent. *The Journal of Physical Chemistry B*, 107(32):8041, 2003.

[156] Peter Loh, G Roshan Deen, Doris Vollmer, Karl Fischer, Manfred Schmidt, Arindam Kundagrami, and Murugappan Muthukumar. Collapse of linear polyelectrolyte chains in a poor solvent: when does a collapsing polyelectrolyte collect its counterions? *Macromolecules*, 41(23):9352, 2008.

[157] Eugene Wigner. On the interaction of electrons in metals. *Physical Review*, 46(11):1002, 1934.

[158] Boris I Shklovskii. Wigner crystal model of counterion induced bundle formation of rodlike polyelectrolytes. *Physical Review Letters*, 82(16):3268, 1999.

[159] Ioulia Rouzina and Victor A Bloomfield. Macroion attraction due to electrostatic correlation between screening counterions. 1. mobile surface-adsorbed ions and diffuse ion cloud. *The Journal of Physical Chemistry*, 100(23):9977, 1996.

[160] Götz Jerke, Jan Skov Pedersen, Stefan Ulrich Egelhaaf, and Peter Schurtenberger. Flexibility of charged and uncharged polymer-like micelles. *Langmuir*, 14(21):6013, 1998.

[161] C Sommer, L Cannavacciuolo, SU Egelhaaf, JS Pedersen, and P Schurtenberger. Micelles as model systems for equilibrium polyelectrolytes: a light and neutron scattering study. In *Trends in Colloid and Interface Science XIV*, page 347. Springer, 2000.

[162] Luigi Cannavacciuolo, Jan Skov Pedersen, and Peter Schurtenberger. Monte carlo simulation study of concentration effects and scattering functions for polyelectrolyte wormlike micelles. *Langmuir*, 18(7):2922, 2002.

[163] Anvy Moly Tom, R Rajesh, and Satyavani Vemparala. Aggregation dynamics of rigid polyelectrolytes. *The Journal of Chemical Physics*, 144(3):034904, 2016.

[164] Paul HJ Kouwer, Matthieu Koepf, Vincent AA Le Sage, Maarten Jaspers, Arend M van Buul, Zaskia H Eksteen-Akeroyd, Tim Woltinge, Erik Schwartz, Heather J Kitto, Richard Hoogenboom, et al. Responsive biomimetic networks from polyisocyanopeptide hydrogels. *Nature*, 493(7434):651, 2013.

[165] Paul A Janmey, David R Slochower, Yu-Hsiu Wang, Qi Wen, and Andrejs Cēbers. Polyelectrolyte properties of filamentous biopolymers and their consequences in biological fluids. *Soft Matter*, 10(10):1439, 2014.

[166] Brett D Ermi and Eric J Amis. Domain structures in low ionic strength polyelectrolyte solutions. *Macromolecules*, 31(21):7378, 1998.

[167] Yubao Zhang, Jack F Douglas, Brett D Ermi, and Eric J Amis. Influence of counterion valency on the scattering properties of highly charged polyelectrolyte solutions. *The Journal of Chemical Physics*, 114(7):3299, 2001.

[168] Jeferson J Arenzon, Jurgen F Stilck, and Yan Levin. Simple model for attraction between like-charged polyions. *The European Physical Journal B-Condensed Matter and Complex Systems*, 12(1):79, 1999.

[169] Jeferson J Arenzon, Yan Levin, and Jürgen F Stilck. The mean-field theory for attraction between like-charged macromolecules. *Physica A: Statistical Mechanics and its Applications*, 283(1):1, 2000.

[170] Francisco J Solis and Monica Olvera De La Cruz. Attractive interactions between rodlike polyelectrolytes: polarization, crystallization, and packing. *Physical Review E*, 60(4):4496, 1999.

[171] E Allahyarov, G Gompper, and H Löwen. Attraction between dna molecules mediated by multivalent ions. *Physical Review E*, 69(4):041904, 2004.

[172] Yan Levin, Jeferson J Arenzon, and Jürgen F Stilck. The nature of attraction between like-charged rods. *Physical Review Letters*, 83(13):2680, 1999.

[173] Anoop Varghese, R Rajesh, and Satyavani Vemparala. Aggregation of rod-like polyelectrolyte chains in the presence of monovalent counterions. *The Journal of chemical physics*, 137(23):234901, 2012.

[174] M V Smoluchowski. Attempt of a mathematical theory of the coagulation kinetics of colloidal l solutions. *Journal of Physical Chemistry*, 92(1):129–168, 1918.

[175] See http://lammps.sandia.gov for details about the package.

[176] Steve Plimpton. Fast parallel algorithms for short-range molecular dynamics. *Journal of computational physics*, 117(1):1, 1995.

[177] Roger W Hockney and James W Eastwood. *Computer simulation using particles*. CRC Press, 1988.

[178] Madalina Deaconu and Etienne Tanré. Smoluchowski's coagulation equation: probabilistic interpretation of solutions for constant, additive and multiplicative kernels. *Annali della Scuola Normale Superiore di Pisa, Classe di Scienze*, 29(3):549, 2000.

[179] Mohammad Reza Yaghouti, Fraydoun Rezakhanlou, and Alan Hammond. Coagulation, diffusion and the continuous smoluchowski equation. *Stochastic Processes and their Applications*, 119(9):3042–3080, 2009.

[180] C. Connaughton, R. Rajesh, and O. Zaboronski. Kinetics of cluster-cluster aggregation. In K. D. Sattler, editor, *Handbook of Nanophysics: Clusters and Fullerenes*. Taylor and Francis, 2010.

[181] Pavel L Krapivsky, Sidney Redner, and Eli Ben-Naim. *A kinetic view of statistical physics*. Cambridge University Press, 2010.

[182] William Bailey Russel, WB Russel, Dudley A Saville, and William Raymond Schowalter. *Colloidal dispersions*. Cambridge university press, 1991.

[183] TT Nguyen and BI Shklovskii. Kinetics of macroion coagulation induced by multivalent counterions. *Physical Review E*, 65(3):031409, 2002.

[184] F Bordi, C Cametti, S Sennato, and M Diociaiuti. Direct evidence of multicompartment aggregates in polyelectrolyte-charged liposome complexes. *Biophysical journal*, 91(4):1513, 2006.

[185] Markus Susoff, Dominik Winter, Claus D Eisenbach, and Wilhelm Oppermann. Aggregation behavior of rodlike ionogenic polymers in chloroform. *The Journal of Physical Chemistry B*, 112(15):4519, 2008.

[186] Anvy Moly Tom, Ravindran Rajesh, and Satyavani Vemparala. Aggregation of flexible polyelectrolytes: Phase diagram and dynamics. *The Journal of chemical physics*, 147(14):144903, 2017.

[187] Ruxandra I Dima and D Thirumalai. Asymmetry in the shapes of folded and denatured states of proteins. *The Journal of Physical Chemistry B*, 108(21):6564, 2004.

[188] Mark L Henle and Philip A Pincus. Equilibrium bundle size of rodlike polyelectrolytes with counterion-induced attractive interactions. *Physical Review E*, 71(6):060801, 2005.

[189] B-Y Ha and AJ Liu. Kinetics of bundle growth in dna condensation. *Europhysics Letters*, 46(5):624, 1999.

[190] Satya N. Majumdar, Supriya Krishnamurthy, and Mustansir Barma. Nonequilibrium phase transitions in models of aggregation, adsorption, and dissociation. *Physical Review Letters*, 81:3691, Oct 1998.

[191] Satya N Majumdar, Supriya Krishnamurthy, and Mustansir Barma. Nonequilibrium phase transition in a model of diffusion, aggregation, and fragmentation. *Journal of Statistical Physics*, 99(1):1, 2000.

[192] PL Krapivsky and S Redner. Transitional aggregation kinetics in dry and damp environments. *Physical Review E*, 54(4):3553, 1996.

[193] R Rajesh and Satya N Majumdar. Exact phase diagram of a model with aggregation and chipping. *Physical Review E*, 63(3):036114, 2001.

[194] R Rajesh and Supriya Krishnamurthy. Effect of spatial bias on the nonequilibrium phase transition in a system of coagulating and fragmenting particles. *Physical Review E*, 66(4):046132, 2002.

[195] R Rajesh, Dibyendu Das, Bulbul Chakraborty, and Mustansir Barma. Aggregate formation in a system of coagulating and fragmenting particles with mass-dependent diffusion rates. *Physical Review E*, 66(5):056104, 2002.